

DEVELOPMENT OF A TWO-PHASE FLOW SIMULATOR USING PORE NETWORK MODELLING

César Gustavo Timaná Beteta

Dissertação de Mestrado apresentada ao
Programa de Pós-graduação em Engenharia
Química, COPPE, da Universidade Federal
do Rio de Janeiro, como parte dos requisitos
necessários à obtenção do título de Mestre em
Engenharia Química.

Orientadores: Paulo Laranjeira da Cunha

Lage

Paulo Couto

Rio de Janeiro

Março de 2025

DEVELOPMENT OF A TWO-PHASE FLOW SIMULATOR USING PORE
NETWORK MODELLING

César Gustavo Timaná Beteta

DISSERTAÇÃO SUBMETIDA AO CORPO DOCENTE DO INSTITUTO
ALBERTO LUIZ COIMBRA DE PÓS-GRADUAÇÃO E PESQUISA DE
ENGENHARIA DA UNIVERSIDADE FEDERAL DO RIO DE JANEIRO COMO
PARTE DOS REQUISITOS NECESSÁRIOS PARA A OBTENÇÃO DO GRAU
DE MESTRE EM CIÊNCIAS EM ENGENHARIA QUÍMICA.

Orientadores: Paulo Laranjeira da Cunha Lage

Paulo Couto

Aprovada por: Prof. Paulo Laranjeira da Cunha Lage

Prof. Paulo Couto

Prof. Gabriel Gonçalves da Silva Ferreira

D.Sc. Elizabeth May Braga Dulley Pontedeiro

RIO DE JANEIRO, RJ – BRASIL

MARÇO DE 2025

Timaná Beteta, César Gustavo

Development of a two-phase flow simulator using pore network modelling/César Gustavo Timaná Beteta. – Rio de Janeiro: UFRJ/COPPE, 2025.

XXIX, 167 p.: il.; 29, 7cm.

Orientadores: Paulo Laranjeira da Cunha Lage

Paulo Couto

Dissertação (mestrado) – UFRJ/COPPE/Programa de Engenharia Química, 2025.

Referências Bibliográficas: p. 125 – 133.

1. Pore media. 2. Two-phase flow. 3. Pore network modeling. 4. OpenPNM. I. Laranjeira da Cunha Lage, Paulo *et al.* II. Universidade Federal do Rio de Janeiro, COPPE, Programa de Engenharia Química. III. Título.

*O uso de programas
computacionais para simular
processos tem um objetivo
simples: reduzir o tempo que eu
levaria para fazer o mesmo com
papel e lápis.*

Agradecimentos

Agradeço a Deus pelo amparo incondicional ao longo desta jornada. A meus pais, Gustavo e Marleny, e ao meu irmão Johan, por todo o apoio e incentivo desde que me lancei neste desafio longe de casa, sempre mantendo contato e me acompanhando à distância. Aos meus amigos do LTFD – Alex, Lauren, Manuela e Matheus –, sou grato por me ajudarem na adaptação ao trabalho no laboratório, pelos conselhos e por tornarem esse período mais amigável. Aos meus orientadores, Paulo Lage e Paulo Couto, agradeço pela orientação neste projeto e pela paciência, especialmente considerando que o idioma foi, em muitos momentos, um desafio adicional para o entendimento. Finalmente e igual de importante, a todos os amigos que fiz desde que cheguei ao Rio, meu profundo agradecimento. Cada um, à sua maneira, contribuiu positivamente para minha trajetória como estudante de mestrado, e sua presença em minha vida foi essencial para que eu chegasse até aqui.

Resumo da Dissertação apresentada à COPPE/UFRJ como parte dos requisitos necessários para a obtenção do grau de Mestre em Ciências (M.Sc.)

DESENVOLVIMENTO DE UM SIMULADOR DE ESCOAMENTO BIFÁSICO UTILIZANDO MODELAGEM DE REDE DE POROS

César Gustavo Timaná Beteta

Março/2025

Orientadores: Paulo Laranjeira da Cunha Lage

Paulo Couto

Programa: Engenharia Química

Este estudo apresenta o desenvolvimento de um simulador de escoamento bifásico em redes de poros, considerando a presença simultânea das fases em poros e gargantas. O simulador, que representa poros e gargantas como prismas de seção transversal triangular, utiliza bibliotecas do software *OpenPNM* V 3.2.0, e pode processar redes geradas via *PoreSpy* V 2.2.2. Para o modelamento dos processos de drenagem primária e imbibição, foi considerado o cálculo de estados quasi-estáticos. Com isso, foi possível modelar a adesão da fase molhante às paredes, permitindo deslocamentos tipo “snapoff” ou mantendo a conectividade dos clusters por meio de camadas. O simulador foi utilizado em análises de sensibilidade para avaliar o impacto da variabilidade estatística na geração das redes, do tamanho das gargantas e dos ângulos de contato de avanço e recuo nos resultados de permeabilidade relativa e pressão capilar durante os processos de drenagem primária e embebição. Além disso, redes com diferentes distribuições de conexão poro-garganta, tamanhos de poros e gargantas, mas com a mesma porosidade e permeabilidade absoluta, foram comparadas em termos de permeabilidade relativa e pressão capilar nos mesmos processos. Os resultados obtidos seguiram as tendências esperadas com base na teoria.

Abstract of Dissertation presented to COPPE/UFRJ as a partial fulfillment of the requirements for the degree of Master of Science (M.Sc.)

DEVELOPMENT OF A TWO-PHASE FLOW SIMULATOR USING PORE NETWORK MODELLING

César Gustavo Timaná Beteta

March/2025

Advisors: Paulo Laranjeira da Cunha Lage

Paulo Couto

Department: Chemical Engineering

This study presents the development of a two-phase flow simulator using pore networks, considering the simultaneous presence of both phases in pores and throats. The simulator, which represents pores and throats as prisms with triangular cross sections, utilizes libraries from the *OpenPNM* V 3.2.0 software and can process networks generated through *PoreSpy* V 2.2.2. For modeling the primary drainage and imbibition processes, quasi-static states were considered in the calculations. These considerations enabled the modeling of wetting-phase adhesion to walls, which allowed for snapoff displacements and the maintenance of cluster connectivity through layers. The simulator was used in sensitivity analyses to evaluate the impact of statistical variability in the generation of the networks, throat sizes, and advancing and receding contact angles on the results of relative permeability and capillary pressure during primary drainage and imbibition processes. In addition, networks with different pore-throat connection distributions, pore sizes, and throat sizes, but with the same porosity and absolute permeability, were compared in terms of relative permeability and capillary pressure during the same processes. The results obtained followed the trends expected based on the theory.

Contents

List of Figures	xii
List of Tables	xxii
List of Symbols	xxiv
1 Introduction	1
1.1 Objectives	3
1.2 Document Structure	3
2 Literature review	4
2.1 Generation of pore-network models	4
2.2 Fluid behavior in porous materials	6
2.2.1 Experimental studies	6
2.2.2 Quasi-static flow simulation using PNM	7
2.2.3 Direct numerical simulations	9
2.3 Recent PNM uses	10
2.4 Open-source PNM software	11
3 Methodology	13
3.1 PNM softwares	14
3.1.1 PoreSpy	14
3.1.2 OpenPNM	15
3.2 Geometrical properties of pores and throats	18
3.2.1 Spherical pores and cylindrical throats	19

3.2.2	Triangular prismatic elements	21
3.3	Network construction	27
3.4	Phase properties	29
3.4.1	Contact angle and wettability	29
3.4.2	Interfacial tension	29
3.5	Quasi-static model for network invasion	30
3.5.1	Displacement events and phase distribution	31
3.5.2	Primary drainage	32
3.5.3	Imbibition	36
3.5.4	Phase locations	45
3.5.5	Clusters	45
3.5.6	Invasion simulation	49
3.6	Relative permeability calculation	54
3.6.1	Pore and throat conductance for single-phase flow	54
3.6.2	Pore and throat conductance for multiphase flow	59
3.6.3	Conduit conductance	62
3.6.4	Transport properties of the pore network	63
3.6.5	Algorithm to calculate relative permeability	64
3.7	Berea pore network calibration	65
4	Numerical Procedure	67
4.1	Determination of parameters of correlations	67
4.2	Network calibration using the absolute permeability	68
4.3	Tuning network porosity and permeability	69
5	Results and Discussions	74
5.1	Improvement of the throat cross-sectional data	75
5.2	Correction factor for conductance in triangular ducts	77
5.3	Absolute permeability of the Berea sandstone network	78

5.3.1	Impact of the categories of pore diameter on the absolute permeability	78
5.3.2	Impact of the calculation of the minimum length on the absolute permeability	79
5.3.3	Impact on the absolute permeability by using triangles as cross-sectional shapes for throats and pores	79
5.4	Relative permeability of the Berea network	81
5.5	Evaluation of the simulator using statistically built networks	84
5.5.1	Preliminary Test	89
5.5.2	Proposed case studies	92
5.5.3	Statistical analysis of PNM properties	95
5.5.4	Influence of throat-to-pore area ratio	113
5.5.5	Results for different networks with the same permeability and porosity	116
5.5.6	Influence of receding contact angle	120
5.5.7	Influence of advancing contact angle	121
6	Conclusions	123
6.1	Future work suggestions	124
	References	125
A	Modeling throats as isosceles triangular prisms	134
A.1	Algorithm to build pixelized isosceles triangles	134
A.2	Calculation of the minimum shape factor	138
A.3	Calculation of the half-corner angles for an isosceles triangle	141
B	Calculating geometric properties for the equilateral triangular prismatic pores	146
C	Defining properties to create networks	149
C.1	Defining pore diameters using a truncated lognormal distribution . . .	149

C.2	Avoiding pore overlapping in imposing pore diameter distribution . . .	151
D	Calculation of entry capillary pressures	153
D.1	Analysis of the PLD in a throat	153
D.1.1	Primary drainage	153
D.1.2	Spontaneous imbibition process	156
D.1.3	Forced imbibition process	158
D.2	Analysis for snap-off in spontaneous imbibition	160
D.3	Analysis for layer collapse	163
E	Calculation of conductance expressions	166

List of Figures

2.1	a) Triangular, and b) square cross sections occupied by two phases. c) a circular cross section can only be occupied by one phase	10
3.1	Pore length L_j considering a spherical pore: (a) non-overlapping and (b) overlapping pores.	20
3.2	Flowchart for calculation of geometry properties of throats.	24
3.3	Examples of wettability. Phase 1 is taken as a reference to measure the contact angle. Values in radians. Adapted from BLUNT (2017) .	29
3.4	Two phases, white and light blue, in an element. a) 3D representa- tion of a prism with a triangular cross section b) parallel lateral cut, showing the main terminal meniscus c) cross section, showing the arc menisci.	32
3.5	Geometrical information for a piston-like displacement event showing (a) the displacement dx , (b) the effective area and the length of the interfaces in the element cross section, and (c) the geometrical details of a corner with an AM. Before invasion, only the $nw - s$ interface exist, occupying all the perimeter of the cross-section area of the element. The variable α_i is used in Appendix D.1.1.	33
3.6	Geometry of a corner of the cross-section of an element if forced im- bibition is carried out. For spontaneous imbibition, the geometry of Figure 3.5c can be used. α_i is used for demonstration in Section D.1.3.	36

3.7	Iteration to calculate p_c^e for a throat invaded considering a PLD. $iter$ is the number of iterations. tol is the tolerance. The lower the value of i , the lower β_i value.	40
3.8	Different pore-body filling events with (a) $N = 1$ and (b) $N = 2$. Extracted from BLUNT (2017).	42
3.9	A snap-off event. Extracted from BLUNT (2017).	42
3.10	AM displacements and collision. The AMs in red are moving towards the center. We show (a) just one AM moving, and (b) all AM are moving.	43
3.11	Planar fluid-fluid interface	44
3.12	Different fluid configurations.	45
3.13	Possible displacements according to the invading phase (indicated in boxes) and the fluid configuration inside the element. The displacements considered are: piston-like displacement (PLD), pore-body Filling (PB), snap-off (SO), and layer collapse (LC).	46
3.14	Procedure to identify clusters. “p.loc.” is the abbreviation for “phase location”	48
3.15	Procedure for invasion in primary drainage. $p_{c,s}^e$ is the minimum p_c^e obtained at the current invasion state.	51
3.16	Procedure for invasion in imbibition. $p_{c,s}^e$ is the maximum p_c^e obtained at the current invasion state.	53
3.17	Tube with an arbitrary cross section. Extracted from AKBARI <i>et al.</i> (2011)	55
3.18	Part of an sphere with radius R , and a cross section of radius $R^c(x)$.	56
3.19	Value of $32/(fRe_{Dh})$ for different isosceles triangles. β_{dif} is the different β on the triangle.	58
3.20	Geometrical analysis of a corner layer.	61

3.21	Algorithm to calculate flow rate for one phase during a specific quasi-static state. $q_{p,int}$ and $q_{p,out}$ are the phase flow rate on an inlet or outlet pore, respectively. p.loc. means “phase locations”.	66
4.1	Procedure for tuning network permeability k_{abs} by binary search. All pore and throat properties are calculated according to the algorithm in Section 3.3.	70
4.2	Procedure for tuning network porosity Φ by binary search. All pore and throat properties are calculated according to the algorithm in Section 3.3.	71
4.3	Procedure for tuning networks	73
5.1	Relation between the shape factor calculated with PoreSpy and the real shape factor for different isosceles triangles that can be represented with (a) 20 voxels, (b) 30 voxels, (c) 100 voxels, and (d) 1000 voxels. The trend lines using Equation 3.12 with their 95% confidence error and R-squared are shown.	76
5.2	ζ data, errorbar, and trend line for each triangle group.	76
5.3	Cumulative distribution of the internal throat shape factors of the Berea network, after and before correction	77
5.4	Correction factor F_g for different trend lines. The cubic function is $F_g(x) = c_0 + c_1x + c_2x^2 + c_3x^3$. The sinusoidal function is $F_g(x) = c_0 + c_1 \sin(c_2x + c_3)$. The optimization method used to calculate the coefficients is least squares.	77

5.5	Absolute permeability (mD) of the Berea sandstone network if we set $G = G^*$ for the throats with $G < G^*$. The abscissa are (a) the different values of G^* and (b) the percentual values of the cumulative distribution at G^* . <i>OpenPNM</i> V 3.2.0 was used, considering equivalent diameter of pores and throats, and $L_{min} = L_v$. We represent pores as spheres, and throats as prisms with isosceles triangles as cross sections.	80
5.6	Distribution plots of the ratio of the throat equivalent diameter to the minimum connected pore equivalent diameter; compared to (a) the throat conductance ($\mu = 0.001$ Pa.s), and (b) the throat cross-sectional area; for the Berea network. All throats are represented as prisms with an isosceles triangle as the cross-sectional shape.	82
5.7	Sensitivity analysis of the contact angle on the primary drainage simulation, for a Berea network represented by prismatic pores and throats. We show the results of (a) oil relative permeability, (b) water relative permeability and (c) capillary pressure according to the water saturation	85
5.8	Sensitivity analysis of the throat volume on the primary drainage simulation, for a Berea network represented by prismatic pores and throats. We show the results of (a) oil and water relative permeability, and (b) capillary pressure according to the water saturation	86
5.9	Sensitivity analysis of the throat shape factor on the primary drainage simulation, for a Berea network represented by prismatic pores and throats. We show the results of (a) oil and water relative permeability, and (b) capillary pressure according to the water saturation	87
5.10	Histogram of the pore equivalent diameter data from the Berea sample and a lognormal distribution curve with the same mean and standard deviation as the Berea data	88

5.11	Flow simulation results for the C10F36 (a, c, e) and CZ10T (b, d, f) networks, considering $\theta_r = \theta_a = 0^\circ$. (a,b) relative permeability, (c,d) capillary pressure, and (e,f) cumulative number of displacements are shown. The quasi-static states are sampled at different intervals: for drainage is at every 10 states, for imbibition is at every 20 states. . . .	90
5.12	Flow simulation results for the C10F36 (a, c, e) and CZ10T (b, d, f) networks, considering $\theta_r = 60^\circ$, $\theta_a = 110^\circ$. (a,b) relative permeability, (c,d) capillary pressure, and (e,f) cumulative number of displacements are shown. The quasi-static states are sampled at different intervals: for drainage is at every 10 states, for imbibition, they are sampled first at every 4 states (filled markers) and at every 20 states afterward (unfilled markers).	91
5.13	Statistical analysis of properties for C10F36 networks. a) porosity, with $\bar{\Phi} = 0.188$ and $\sigma_{\Phi} = 0.008$. b) absolute permeability, with $\bar{k}_{abs} = 1.57$ D and $\sigma_k = 0.28$ D.	95
5.14	Statistical analysis of properties for for C20F36 networks. a) porosity, with $\bar{\Phi} = 0.190$ and $\sigma_{\Phi} = 0.003$. b) absolute permeability, with $\bar{k}_{abs} = 1.53$ D and $\sigma_k = 0.10$ D.	95
5.15	Statistical analysis of the drainage simulation results for C10F36 networks, considering $\theta_r = \theta_a = 0^\circ$. a) water relative permeability, b) oil relative permeability, and c) capillary pressure are sampled at every 10 states. d) maximum capillary pressure, with $\bar{p}_c = 127.3$ kPa and $\sigma_p = 23.3$ kPa.	96
5.16	Statistical analysis of the imbibition simulation results for C10F36 networks, considering $\theta_r = \theta_a = 0^\circ$. a) water relative permeability, b) oil relative permeability, and c) capillary pressure are sampled at every 20 states. d) final water saturation, with $\bar{X}_w = 0.392$ and $\sigma_{X_w} = 0.025$ kPa. e) final water relative permeability, with $\bar{k}_w = 0.148$ and $\sigma_{kw} = 0.014$	97

5.17	Statistical analysis of the drainage simulation results for the C20F36 networks, considering $\theta_r = \theta_a = 0^\circ$. a) water relative permeability, b) oil relative permeability, and c) capillary pressure are sampled at every 50 states. d) maximum capillary pressure, with $\bar{p}_c = 232.2$ kPa and $\sigma_p = 30.6$ kPa.	98
5.18	Statistical analysis of the imbibition simulation results for the C20F36 networks, considering $\theta_r = \theta_a = 0^\circ$. a) water relative permeability, b) oil relative permeability, and c) capillary pressure are sampled at every 100 states. d) final water saturation, with $\bar{X}_w = 0.365$ and $\sigma_{X_w} = 0.007$ kPa. e) final water relative permeability, with $\bar{k}_{wv} = 0.145$ and $\sigma_{k_{wv}} = 0.008$	99
5.19	Statistical analysis of the drainage simulation results for the C10F36 networks, considering $\theta_r = 60^\circ$, $\theta_a = 110^\circ$. a) water relative permeability, b) oil relative permeability, and c) capillary pressure are sampled at every 10 states. d) maximum capillary pressure, with $\bar{p}_c = 62.5$ kPa and $\sigma_p = 19.1$ kPa.	100
5.20	Statistical analysis of the imbibition simulation results for the C10F36 networks, considering $\theta_r = 60^\circ$, $\theta_a = 110^\circ$. a) water relative permeability, b) oil relative permeability, and c) capillary pressure are sampled first at every 4 states until state 60 (filled markers) and then every 20 states (unfilled markers). d) capillary pressure required to perform the last displacement, with $\bar{p}_c = -42.7$ kPa and $\sigma_p = 13.1$ kPa.	101
5.21	Statistical analysis of the drainage simulation for the C20F36 networks, considering $\theta_r = 60^\circ$, $\theta_a = 110^\circ$. a) water relative permeability, b) oil relative permeability, and c) capillary pressure are sampled at every 50 states. d) maximum capillary pressure, with $\bar{p}_c = 117.8$ kPa and $\sigma_p = 15.4$ kPa.	102

5.22	Statistical analysis of the imbibition simulation results of the C20F36 networks, considering $\theta_r = 60^\circ$, $\theta_a = 110^\circ$. a) water relative permeability, b) oil relative permeability, and c) capillary pressure are sampled first at every 20 states until state 500 (filled markers) and then every 100 states (unfilled markers). d) capillary pressure required to perform the last displacement, with $\bar{p}_c = -80.5$ kPa and $\sigma_p = 10.5$ kPa.	103
5.23	Statistical analysis of properties for CZ10F36 networks. a) porosity, with $\bar{\Phi} = 0.135$ and $\sigma_\Phi = 0.009$. b) absolute permeability, with $\bar{k}_{abs} = 2.38$ D and $\sigma_k = 0.44$ D.	104
5.24	Statistical analysis of properties for CZ20F36 networks. a) porosity, with $\bar{\Phi} = 0.138$ and $\sigma_\Phi = 0.003$. b) absolute permeability, with $\bar{k}_{abs} = 1.96$ D and $\sigma_k = 0.19$ D.	104
5.25	Statistical analysis of the drainage simulation results for the CZ10F36 networks, considering $\theta_r = \theta_a = 0^\circ$. a) water relative permeability, b) oil relative permeability, and c) capillary pressure are sampled at every 10 states. d) maximum capillary pressure, with $\bar{p}_c = 122.2$ kPa and $\sigma_p = 38.0$ kPa.	105
5.26	Statistical analysis of the imbibition simulation for the CZ10F36, considering $\theta_r = \theta_a = 0^\circ$. a) water relative permeability, b) oil relative permeability, and c) capillary pressure are sampled at every 20 states. d) final water saturation, with $\bar{X}_w = 0.434$ and $\sigma_{X_w} = 0.028$. e) final water relative permeability, with $\bar{k}_w = 0.171$ and $\sigma_{k_w} = 0.025$	106
5.27	Statistical analysis of the drainage simulation results for the CZ20F36 networks, considering $\theta_r = \theta_a = 0^\circ$. a) water relative permeability, b) oil relative permeability, and c) capillary pressure are sampled at every 50 states. d) maximum capillary pressure, with $\bar{p}_c = 212.0$ kPa and $\sigma_p = 69.0$ kPa.	107

5.28	Statistical analysis of the imbibition simulation results for the CZ20F36 networks, considering $\theta_r = \theta_a = 0^\circ$. a) water relative permeability, b) oil relative permeability, and c) capillary pressure are sampled at every 100 states. d) final water saturation, with $\bar{X}_w = 0.385$ and $\sigma_{X_w} = 0.005$ kPa. e) final water relative permeability, with $\bar{k}_w = 0.158$ and $\sigma_{k_w} = 0.007$	108
5.29	Statistical analysis of the drainage simulation results for the CZ10F36 networks, considering $\theta_r = 60^\circ$, $\theta_a = 110^\circ$. a) water relative permeability, b) oil relative permeability, and c) capillary pressure are sampled at every 10 states. d) maximum capillary pressure, with $\bar{p}_c = 62.5$ kPa and $\sigma_p = 19.1$ kPa.	109
5.30	Statistical analysis of the imbibition simulation results for the CZ10F36 networks, considering $\theta_r = 60^\circ$, $\theta_a = 110^\circ$. a) water relative permeability, b) oil relative permeability, and c) capillary pressure are sampled first at every 4 states until state 60 (filled markers) and then every 20 states (unfilled markers). d) capillary pressure required to perform the last displacement, with $\bar{p}_c = -42.7$ kPa and $\sigma_p = 13.1$ kPa.	110
5.31	Statistical analysis of the drainage simulation results for the CZ20F36 networks, considering $\theta_r = 60^\circ$, $\theta_a = 110^\circ$. a) water relative permeability, b) oil relative permeability, and c) capillary pressure are sampled at every 50 states. d) maximum capillary pressure, with $\bar{p}_c = 111.5$ kPa and $\sigma_p = 29.1$ kPa.	111
5.32	Statistical analysis of the imbibition simulation results for the CZ20F36 networks, considering $\theta_r = 60^\circ$, $\theta_a = 110^\circ$. a) water relative permeability, b) oil relative permeability, and c) capillary pressure are sampled first at every 20 states until state 500 (filled markers) and then every 100 states (unfilled markers). d) capillary pressure required to perform the last displacement, with $\bar{p}_c = -76.2$ kPa and $\sigma_p = 19.9$ kPa.	112

5.33	Primary drainage results using networks with different F_{At} , considering $\theta_r = \theta_a = 0^\circ$. a) relative permeability of oil (dash-dot) and water (dashed). b) capillary pressure.	114
5.34	Imbibition results using networks with different F_{At} , considering $\theta_r = \theta_a = 0^\circ$. a) relative permeability of oil (dash-dot) and water (dashed). b) capillary pressure.	114
5.35	Primary drainage results using networks with different F_{At} , considering $\theta_r = 60^\circ$ and $\theta_a = 110^\circ$. a) relative permeability of oil (dash-dot) and water (dashed). b) capillary pressure.	115
5.36	Imbibition results using networks with different F_{At} , considering $\theta_r = 60^\circ$ and $\theta_a = 110^\circ$. a) relative permeability of oil (dash-dot) and water (dashed). b) capillary pressure.	115
5.37	Primary drainage results using two different networks with the same Φ and k_{abs} , considering $\theta_r = \theta_a = 0^\circ$. a) relative permeability of oil (dash-dot) and water (dashed). b) capillary pressure.	117
5.38	Imbibition results using two different networks with the same Φ and k_{abs} , considering $\theta_r = \theta_a = 0^\circ$. a) relative permeability of oil (dash-dot) and water (dashed). b) capillary pressure.	117
5.39	Primary drainage results using two different networks with the same Φ and k_{abs} , considering $\theta_r = 60^\circ$ and $\theta_a = 110^\circ$. a) relative permeability of oil (dash-dot) and water (dashed). b) capillary pressure.	118
5.40	Imbibition results using two different networks with the same Φ and k_{abs} , considering $\theta_r = 60^\circ$ and $\theta_a = 110^\circ$. a) relative permeability of oil (dash-dot) and water (dashed). b) capillary pressure.	118
5.41	Impact of θ_r during primary drainage on the C20F36 network, considering $\theta_a = 60^\circ$. a) relative permeability of oil (dash-dot) and water (dashed). b) capillary pressure.	120

5.42	Impact of θ_a during imbibition on the C20F36 network, considering $\theta_r = 0^\circ$. a) relative permeability of oil (dash-dot) and water (dashed). b) capillary pressure.	121
5.43	Impact of θ_a during imbibition on the C20F36 network, considering $\theta_r = 60^\circ$. a) relative permeability of oil (dash-dot) and water (dashed). b) capillary pressure.	122
A.1	Conversion into pixels of an isosceles triangle with $A = 35u^2$ and $h = 7u$. Voxel size = $1u$	135
A.2	Results of building isosceles triangles with voxels before correct number of voxels used. (a) The probability to obtain more voxels than expected and (b) the average ratio $\Delta n_v/n_l$ are shown.	137
A.3	G_{min} analysis for $v = 30$, where only one voxel (in gray) of the triangle is “protected” by “perimeter” voxels (in red).	139
A.4	Geometry of a triangle with an inscribed circle of radius R	142
B.1	Aspect ratio for triangular prisms with volume V and superficial area S . The roots are related to the possible values of the edge side a , calculated with Equation B.3	148
D.1	Reproduction of Figure 3.5c	153
D.2	Reproduction of Figure 3.6	159
D.3	Geometrical analysis of a triangular cross section after the invasion of the non-wetting phase. $0 < \beta_1 \leq \beta_2 \leq \beta_3 < \pi/2$	160
D.4	Reproduction of Figure 3.20	163
E.1	Planar fluid-fluid interface, when $r \rightarrow \infty$	167

List of Tables

3.1	Pore properties using <i>PoreSpy</i> V 2.2.2. n_p is the number of pores. . .	16
3.2	Throat properties using <i>PoreSpy</i> V 2.2.2. n_t is the number of throats.	17
3.3	Criteria for connectivity in adjacent elements. Extracted from PIRI (2003).	47
3.4	fRe for different isosceles triangles. Extracted from WHITE (2002) .	57
4.1	Iteration history for the tuning of network CZ20T (network details on Table 5.10). The reference values are: $k_{abs}^{ref} = 1.662D$, $\phi^{ref} = 19.47 \times 10^{-2}$. The main iterations are those where we complete the cycle of tuning both parameters k_{abs} and Φ . TBSI is the total binary search iterations.	72
5.1	Properties of the Berea image.	75
5.2	Parameters value to improve G for throats	75
5.3	Results for the polynomial function $F_g(x) = c_0 + c_1x + c_2x^2 + c_3x^3$ with the error at 95 % confidence interval	78
5.4	Absolute permeability (mD) of a Berea image using <i>OpenPNM</i> V 3.2.0 considering spherical pores and cylindrical throats using their equivalent diameters and $F_L = 0.05$ in Eq. 3.8.	79
5.5	Absolute permeability (mD) of a Berea network represented with spherical pores and cylindrical throats using <i>OpenPNM</i> V 3.2.0, considering equivalent diameter of pores and throats, and $L_{min} = L_v$. . .	79
5.6	Phase properties used to simulate two-phase invasion	82

5.7	Properties of $10 \times 10 \times 10$ networks with similar Φ , k_{abs} . For those networks: $\lambda = 146 \mu\text{m}$, $N_p = 1000$, $N_t = 2700$, the $D_{eq,p}$ distribution corresponds to a lognormal distribution with an interval of $[24.59\mu\text{m}, 266.69\mu\text{m}]$ and $\sigma_D = 38.00 \mu\text{m}$	89
5.8	Simulation details for $10 \times 10 \times 10$ networks	89
5.9	Base properties of the network groups used for statistical analysis . .	93
5.10	Properties of $20 \times 20 \times 20$ networks with $\lambda = 146\mu\text{m}$, $N_p = 8000$, $N_t = 22800$, and lognormal distribution with interval $[24.59\mu\text{m}; 266.69\mu\text{m}]$ and standard deviation $\sigma_D = 38.00\mu\text{m}$	93
5.11	Simulation details to test θ_a . The same network C20F36 is used in all cases.	94
5.12	Simulation details to test θ_a . The same network C20F36 is used in all cases.	94
5.13	Information of displacements at the last state of the imbibition process on networks with the same Φ , k_{abs} , for a water-oil system with $\theta_r = \theta_a = 0^\circ$	117

List of Symbols

A	Cross-sectional area
a	Triangle edge length
B	Estimated parameters of an ODR problem
b	Interface corner position
C	Constant value after integration
D	Diameter
e	Error
F	Correction factor
f	Friction factor
G	Shape factor
g	Conductance
h	Height
I_p	Polar momentum of inertia
k	Permeability
L	Length

n	Total number of elements
P	Perimeter
p	Pressure
q	Flow rate
R	Radius
r	Radius of curvature
S	Superficial area
s	Stage of invasion
V	Volume
v	Fluid velocity
Z	Connectivity

Dimensionless numbers

Ca	Capillary number
Re	Reynolds number

Functions

erfc	Complementary error function
\mathbb{F}	Cumulated frequency function
\mathbb{P}	Frequency function

Greek Letters

β	Half corner angle
δ	Error in the independent variable

ϵ	Error in the dependent variable
η	Random number between 0 and 1
κ	Conductance parameters for a specific phase location
λ	Pore spacing
μ	Dynamic viscosity
Φ	Porosity
ϕ	Angular coordinate for cylindrical coordinate system
Ψ	PLD parameter
ψ	PB parameter
ρ	Density
Ω	Body force per unit mass
σ	Interfacial tension
θ	Contact angle
ζ	Shape factor correlation parameters

Mathematical Operations

$-$	Average
Δ	Differential
\sim	Dimensionless

Subscripts

95	95% confidence
a	Advancing

<i>abs</i>	Absolute
<i>c</i>	Capillary
<i>ce</i>	Center
<i>con</i>	Connected
<i>co</i>	Corner
<i>ctc</i>	Conduit
<i>d</i>	Drainage
<i>Dh</i>	Hydraulic diameter
<i>dif</i>	different
<i>g</i>	Conductance
<i>h</i>	Hinging
<i>imb</i>	Imbibition
<i>in</i>	Inner
<i>int</i>	Inlet
<i>l</i>	Layer
<i>min</i>	Maximum
<i>min</i>	Minimum
<i>mph</i>	Multiphase
<i>nw</i>	Non-wetting phase
<i>nw – s</i>	Interaction between the solid and the non-wetting phase
<i>o</i>	Outer

<i>out</i>	Outlet
<i>p</i>	Pore
<i>ph</i>	Phase
<i>pn</i>	Pore network
<i>ps</i>	PoreSpy
<i>R</i>	Radius
<i>r</i>	Receding
<i>rel</i>	Relative
<i>sph</i>	Single phase
<i>t</i>	Throat
<i>v</i>	Voxel
<i>w</i>	Wetting phase
<i>w – s</i>	Interaction between the solid and the wetting phase

Superscript

*	Specific
<i>c</i>	Related to a cross section
<i>cal</i>	Calculated
<i>e</i>	Entry
<i>ref</i>	Reference
S	Snap-off
<i>T</i>	Truncated

Abbreviations

AM	Arc meniscus
DNS	Direct numerical simulation
LC	Layer collapse
LF	Layer formation
LBM	Lattice-Boltzmann method
MB	Maximum ball technique
MTM	Main terminal meniscus
ODR	Orthogonal distance regression
PB	Pore body filling
PBM	Process-based method
PLD	Piston like displacement
PNM	Pore network modelling
R^2	Coefficient of determination
SO	Snap-off

Chapter 1

Introduction

The study of multiphase flow in porous media is a topic of utmost importance in many fields. In the oil & gas industry, it helps to determine the conditions to optimize hydrocarbon recovery (SIMONOV *et al.*, 2023) and to apply carbon capture and storage technologies (WANG *et al.*, 2023). In hydrogeology, it is crucial to understand the migration patterns of liquid pollutants in soils and aquifers, in order to minimize their effects (LI *et al.*, 2024). In addition, porous materials have also been required to construct batteries and combustion cells that do not require fossil fuels, aiming to transition to a clean, zero-carbon energy economy (BLUNT *et al.*, 2024).

However, research on porous media presents various important challenges that have been faced for years. The pore space where liquid or gaseous phases flow through has a high degree of irregularity. Additionally, its scale is usually measured in microns (LI *et al.*, 2017), which means that the accuracy of the method used to extract the topological properties of a porous media is greatly influenced by the ability to get micrometric details and to work at that scale. To further complicate the analysis, chemical reactions and non-isotropic properties can occur (SHOKRI *et al.*, 2024; WANG *et al.*, 2023).

Different flow simulation techniques depending on the scale of the system were developed. Density functional theory, molecular simulation, pore network modeling, direct numerical simulation, and reservoir simulation are some examples of

these techniques (CUI *et al.*, 2022). At the pore scale, where individual pores are resolved, direct numerical simulation (DNS) and pore network modeling (PNM) are recommended. The former technique requires dividing the porous medium into discrete cells to apply a specific flow simulation model, such as Lattice-Boltzmann. Since the pore space is highly irregular, applying DNS to the domain obtained from a high-resolution tomographic image has a high computational cost. On the other hand, PNM simplifies the porous medium geometry, considering that it can be represented by two types of elements: pores and throats. This technique absurdly reduces the computational cost when compared to DNS (SHENG and THOMPSON, 2016) at the expense of accuracy.

Nowadays, different software programs apply the PNM method. Proprietary software examples are *Avizo* and *PoreXpert*. Open-source software, such as *PoreSpy* and *OpenPNM*, also exist. These free-access programs have been developed by a research group at the University of Cambridge, led by Dr. Jeff Gostick. Both codes are written in Python and are complementary: *PoreSpy* obtains a pore network by processing a tomographic image, and *OpenPNM* uses pore networks to simulate processes like invasion or fluid flow (GOSTICK *et al.*, 2019, 2016).

PoreSpy and *OpenPNM* have improved significantly compared to their initial versions. However, current algorithms do not allow the simulation of multiphase flow when considering more complex and realistic events, such as the presence of a phase attached to the solid after the invasion of another phase. It is proven that considering that scenario enhances results by improving connectivity and allowing simulation of more invasion events, such as snap-off. Algorithms for the described scenario have already been developed by various authors (PATZEK and SILIN, 2001; PIRI, 2003; VALVATNE and BLUNT, 2004). We consider that those methods can be implemented in *OpenPNM*.

1.1 Objectives

This project aims to build codes in *OpenPNM* to simulate two-phase flow processes in a porous medium using a pore network modeling approach, allowing us to determine the relative permeability and the sequence of invasion of network pores and throats. For each porous element, the work must consider the simultaneous occupation of both immiscible and non-reacting phases. The software used are *OpenPNM* V 3.2.0 for the flow simulation and *PoreSpy* V 2.2.2 to extract the network from a tomographic image. We divide our main objective into three specific objectives:

1. convert CT images into pore networks using elements with triangular cross-sections and geometric properties as accurately as possible,
2. create quasi-steady flow simulators that predict the invasion order of elements, considering the presence and movement of two phases in each element and different invasion scenarios, such as drainage and imbibition, and
3. redefine or develop functions to calculate the properties of the porous medium based on the results of the two-phase simulators.

1.2 Document Structure

Chapter 2 provides a background of fluid flow experiments and simulations, focusing on two simulation methods: pore network modeling and direct numerical simulations. Chapter 3 details the methodology of the quasi-static analysis of the network invasion and flow through the network, specifying the equations, input parameters, and the boundary conditions required for different network scenarios. Models used for calibration or parameter optimization are in Chapter 4. Results and conclusions are given in Chapters 5 and 6, respectively.

Chapter 2

Literature review

2.1 Generation of pore-network models

Over the years, researchers have elaborated diverse methods to generate a pore network representing a porous medium, allowing the study of the pore space and its interaction with fluids. Nowadays, pore networks are built from the X-ray tomographic (micro-CT) image of rock samples. A good example is the SNOW algorithm proposed by [GOSTICK \(2017\)](#). When rock's analysis technology was not as developed as now, other methods were created and tested to obtain pore-network models.

One of the first methods used to assign properties to the elements of a network was presented by [MCDOUGALL and SORBIE \(1995\)](#), who aimed to simulate wettability tests for fractionally-wet porous mediums. The method called “the 3R’s approach”, assigns three different radii for each pore. The number of pores and connections was previously defined. These radii were used to calculate pore properties like volume and entry capillary pressure. Then, waterflooding simulations were run on a pore space initially filled with oil. Each simulation used a different distribution of water-wet and oil-wet pores. They found that the results for fractionally-wet systems may be different compared to the experimental data from Amott-Harvey’s and free-imbibition tests, suggesting that the test results are imprecise. Also, the best oil recoveries were obtained for systems with between 30% and 50% of water-wet pores.

Another group of models for building pore networks tries to reproduce the natural formation process of the stone: sedimentation, compaction, and diagenesis. These are called process-based models (PBM). [BAKKE and ØREN \(1997\)](#) created an algorithm using this idea. This algorithm works in two stages: the first recreates the formation process, obtaining a 3D voxelized image, and the second generates pores and throats (both with triangular cross sections) from that image. To test the method, a network using information from a Bentheimer sandstone was created, and primary drainage was simulated using the technique proposed in an earlier work ([ØREN *et al.*, 1996](#)), obtaining consistent results of capillary pressure and relative permeability compared to the laboratory measurements.

Micro-CT images of a rock sample can be transformed into a pore network by techniques like maximum ball ([SILIN and PATZEK, 2006](#)) or watershed segmentation ([GOSTICK *et al.*, 2019](#)). In the maximum ball (MB) algorithm, the minimum Euclidean distance to the solid of each voxel is calculated. Then, spheres were created using those distance values as radii. A hierarchical system based on the sphere sizes is used to construct the skeleton of the pore network, from which the pores and throats are identified. [DONG \(2007\)](#) proposed a maximum ball algorithm which is an improved version of [SILIN and PATZEK \(2006\)](#) method. He tested it by calculating the relative error on permeability results, taking as accepted values those obtained by the Lattice-Boltzmann method ([CHEN and DOOLEN, 1998](#); [MANWART *et al.*, 2002](#)). The voxelized images were generated by a PBM to represent Fontainebleau and Berea sandstones ([BAKKE and ØREN, 1997](#); [ØREN and BAKKE, 2002](#); [ØREN and BAKKE, 2003](#)). [DONG \(2007\)](#) concluded that the absolute permeability errors generated by the MB method were lower than those from the PBM, and the MB's relative permeability values were highly accurate.

SNOW is a more up-to-date method proposed by [GOSTICK \(2017\)](#). This method uses marker-based watershed segmentation to define 3D pores and 2D throats. Then, the topological properties are obtained. He validated his model by simulating mercury intrusion on the created networks, getting a good agreement

with the results that came from simulating this process using the domain obtained from the micro-CT images.

2.2 Fluid behavior in porous materials

2.2.1 Experimental studies

Performing multiphase flow experiments in a porous media has several objectives like testing the accuracy of a method or model that simulates the flow at the pore scale, or finding correlations between the porous medium properties. An example of the former is the work done by MORROW (1976), where the relation between capillary pressure and the intrinsic contact angle (measured for the wetting phase) was studied. In the experiments, artificial cores of polytetrafluoroethylene were used. He obtained correlations between those parameters for uniformly wetted systems. Also, he concluded that contact angle values up to 73° did not cause significant impact on the radius of curvature obtained at a specific saturation during a primary drainage process. In addition, for contact angles of 30° and above, he observed that the radius of curvature depended on the intrinsic contact angle during a subsequent imbibition process.

In the next years, OAK (1990) studied Berea sandstone two-phase and three-phase relative permeabilities for a gas-oil-water system, been water the most wetting phase and gas the least wetting. He observed that, regardless of whether two-phase or three-phase flow occurs, the water's relative permeability depended on the water saturation and the gas' relative permeability depended on the gas saturation history. However, oil's relative permeability depended on the saturation values of all the phases present, becoming harder to predict by existing methods, like those developed by STONE (1970, 1973).

2.2.2 Quasi-static flow simulation using PNM

Early research about the quasi-static simulation of multiphase flow were focused on either determining the phase displacement throughout an invasion or calculating the fluid flow for a specific quasi-static state. Nowadays, it is common to study both topics together, using a single pore network model.

An example of improving a complete quasi-static simulation is the two-phase flow methodology developed by M. Blunt ([BLUNT, 1997a,b, 1998](#); [VALVATNE and BLUNT, 2004](#)). His first methodology contemplates the simultaneous occupation of both phases on elements represented by tubes with a square cross section, simulating primary drainage, imbibition, and secondary drainage. Then, the method was improved by including elements with triangular and circular cross sections (see [Figure 2.1](#)), depending on the topological properties of the pore space. Blunt's latest research ([VALVATNE and BLUNT, 2004](#)) concluded that the relative permeability results of this model corresponded closely to the experimental data if the network is previously tuned using data from mercury injection experiments.

[PIRI \(2003\)](#) proposed a complete three-phase network model, in which every element has a circular, square, or triangular cross-section. A total of 11 configurations for fluid accommodation on a corner were considered. The model allows wettability alteration and displacement of trapped clusters, improving relative permeability results for two-phase and three-phase flow simulations. The simulations used a representation of a Berea sandstone using the model proposed by [BAKKE and ØREN \(1997\)](#) and were compared to the experimental results from [OAK \(1990\)](#) for a gas-oil-water system, obtaining good agreement in all results except for the oil relative permeability at low oil saturations. In addition, results for different invasion sequences that, at that time, had not experimental data, were obtained.

The previously mentioned methods apply to networks in which a completely solid rock is assumed to surround the porous space. However, it is possible to consider the effect caused by micropores present in such rocks. [BAUER *et al.* \(2011\)](#) studied electrical conductance (an analogue to hydraulic conductance, which represents the

ease with which a fluid can flow from one point to another) by considering a dual PNM, or double porosity model: one porosity corresponding to the pores and throats representing the porous space, and a second porosity corresponding to the micropores, representing the sections of the rock identified as porous rock. The network construction uses 8-bit gray-level micro-CT images, which pass through a filtering process to obtain images with voxels in three different shades: black, representing a voxel corresponding to the porous space (porosity $\Phi = 0$); gray, corresponding to the porous rock ($0 < \Phi < 1$); and white, corresponding to the solid rock ($\Phi = 1$). For each pore-throat-pore conduit, if the porous rock surrounds the throat, the model adds an extra throat to represent the conductance of the micropores. Based on the volume of porous rock, the porosity of that rock, and the number of throats surrounded by micropores, [BAUER *et al.* \(2011\)](#) calculated the cross-sectional area and the length of the cuboid that represents the microporous throat, parameters required to determine the total conductance of the conduit. The proposed model reproduced the Archie's and non-Archie behaviors observed experimentally in rock samples whose tomographic images were used in the simulations.

Years later, [RABBANI *et al.* \(2020\)](#) proposed a triple pore network model, in which the third porosity corresponds to fractures within the porous medium. They construct the main network, which includes the pore space formed by fractures, by using the watershed segmentation algorithm. The conductance of the conduits in this network was calculated using the image-based throat permeability model developed earlier by [RABBANI and BABAEI \(2019\)](#), which relates the absolute permeability of a conduit to the distance map obtained from the voxelized image of the throat. Similar to the approach by [BAUER *et al.* \(2011\)](#), this model assumes the presence of micropores in partially solid voxels ($0 < \Phi < 1$). However, the absolute permeability of these voxels is estimated using a correlation that depends on the local porosity value, the radius of the micro-throats, and the percentage of micropores connected to the mesopore network (assumed to be 95%). Flow simulation was performed on micro-CT images of three types of carbonate rocks: Estailades, Savonnières, and

Massangis, with fractures manually added to the images. Compared with a model that does not account for microporosity, the proposed model showed an increase in absolute permeability ranging from 20

2.2.3 Direct numerical simulations

Direct numerical simulations (DNS) methods determine flow behavior by solving a flow model consisting of the equations derived from the fundamental conservation laws for mass, momentum, and energy (HÄRTEL, 1996; SEIDL *et al.*, 1997). Due to the microscopic scale of the pore space and the assumption of laminar flow, the method can provide highly accurate results as MALENICA *et al.* (2024) reported. They used a lattice-Boltzmann method (LBM) for a single-phase flow simulation and compared the results with those obtained by finite-difference techniques, finding similar responses in terms of accuracy and computational cost.

Recent works for single-phase flow simulations analyzed error minimization. One example is the work done by MACHADO *et al.* (2024), who analyzed the effects on absolute permeability determination by DNS when smoothing the solid-fluid interface of a voxelized mesh. 2D and 3D pore-space meshes were created using OpenFOAM[®] v2212 (OPENCDF, 2024) and *PoreSpy* (GOSTICK *et al.*, 2019). They concluded that the accuracy of the permeability results improved if smoothed meshes were used only if the mesh resolution was good enough to represent the solid-fluid interface.

On the other hand, multiphase flow simulations were studied in the last decade (MALENICA *et al.*, 2024). Some techniques used were lattice-Boltzmann methods (LIU *et al.*, 2021), smoothed particle hydrodynamics (TARTAKOVSKY *et al.*, 2016), level set methods (FRISS *et al.*, 2019), and the volume of fluid method (SHAMS *et al.*, 2018).

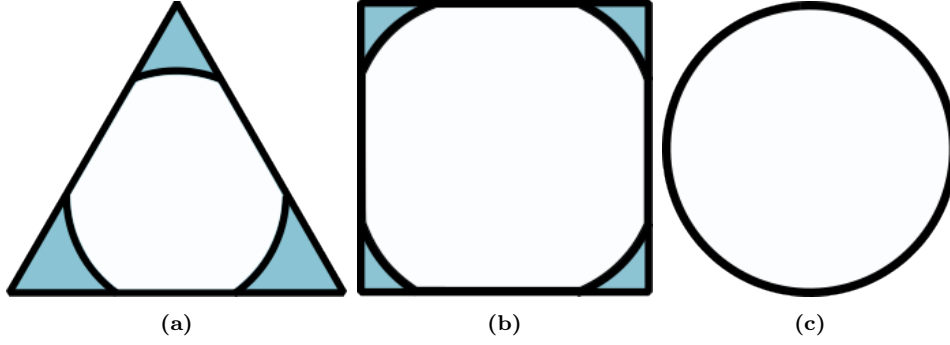


Figure 2.1: a) Triangular, and b) square cross sections occupied by two phases. c) a circular cross section can only be occupied by one phase

2.3 Recent PNM uses

PNM has been a helpful method in recent years because of its low computational cost. For example, [CLAASSEN *et al.* \(2025\)](#) compared the results of purely mechanical dispersion in packed beds obtained using two methods: Particle Resolved CFD (reference results) and PNM. Three different column-to-particle diameter ratios and three different particle Reynolds numbers were evaluated, resulting in a total of nine distinct simulations for each method. To define the pores and throats, the software *pnextract* ([LONDON, 2021](#)) was used, which applies the MB algorithm. Fluid flow was calculated using a semi-empirical correlation for spherical pores and cylindrical throats, which takes into account the pressure drop effects attributed to contraction dissipation, constriction dissipation, and expansion dissipation ([FATHI-GANJEHLOU *et al.*, 2023](#); [LIU *et al.*, 2020](#)). It was observed that, in general, the results obtained with both methods were very similar, achieving greater accuracy for columns with lower column-to-particle diameter ratios. This is because the space through which the fluid flows is smaller in these cases, resulting in lower velocities and, consequently, reduced Taylor dispersion.

[TAGHAVINEJAD *et al.* \(2025\)](#) employed the triple PNM approach proposed by [RABBANI *et al.* \(2020\)](#) to study the physicochemical interactions of CO₂ in shale rocks, which are used for carbon storage. To do so, they generated six representative voxelized samples—three with high porosity and three with low porosity—using the method described in [RABBANI and BABAEI \(2021\)](#). This method involves the se-

quential generation of voxels representing pyrite, calcite, silicate, clay, kerogen, and fractures (in that order). For the simulations, the porous medium was initially saturated with methane at 1 MPa. CO₂ was then injected by increasing its inlet pressure from 1 MPa up to the confining pressure. As a preliminary step, the absolute permeability results obtained from the simulations were compared with experimental data from core samples under a confining pressure of 10 MPa. The simulations reproduced the experimentally observed trend of decreasing absolute permeability with increasing CO₂ inlet pressure under a confining pressure of 10 MPa. After this initial test, two different confining pressures were considered: 25 MPa and 50 MPa. The flow model assumed that every conduit involving a micropore was connected to five micro-throats, as required by the T-PNM formulation. The model also accounted for fracture size variation due to two mechanisms: effective stress change and swelling caused by CO₂ sorption. The study evaluated the total fracture permeability (i.e., permeability contributions from fracture-pore and fracture-fracture connections) and compared cases with and without stress-induced changes. For the 25 MPa case, the fracture permeability ratio (with stress / without stress) decreased with increasing CO₂ inlet pressure. For the 50 MPa case, the behavior was non-monotonic: the ratio decreased for inlet pressures below 25 MPa and increased for pressures above 25 MPa.

2.4 Open-source PNM software

PoreSpy ([GOSTICK *et al.*, 2019](#)) is a Python-based software that generates pore networks representing porous media from X-ray tomography (Micro-CT) images, using the SNOW algorithm proposed by [GOSTICK \(2017\)](#). Its initial version, 0.1.0, was released in July 2015 as an experimental build, followed by a stable version 1.0.0 in February 2019. Notably, the last minor update before version 1, version 0.4.0, introduced two methods for calculating pore surface area and throat cross-sectional area: a standard accuracy method, which estimates properties by counting boundary voxels, and a high-accuracy method, which isolates pore regions and computes

properties using the marching cubes algorithm (LORENSEN and CLINE, 1987) implemented in the scikit-image Python package (VAN DER WALT *et al.*, 2014). Version 2.0.0, released in July 2021, significantly expanded the available controls for generating pore networks compared to version 1.x. Also, it includes an accurate method to calculate pore volume. The latest release, version 2.4.1, was published in March 2024. This version enables the calculation of various pore and throat properties by considering them as 3D regions and 2D surfaces, respectively (details of the properties in Section 3.1.1). However, it does not allow for the computation of properties based on specific geometric representations for pores or throats, such as spheres, cylinders, prisms, or other shapes.

OpenPNM (GOSTICK *et al.*, 2016) is also a Python-based software package, but specifically developed for performing pore network simulations of porous materials. Since its first version, it has included algorithms to simulate invasion percolation, viscous flow, heat conduction, and binary diffusion, as well as tools to generate different types of networks, such as cubic-lattice networks or networks based on Delaunay tessellations. It also provides support for implementing phase properties for fluids like water, air, and mercury. This software can work with networks extracted using *PoreSpy*, as both tools were developed by the same research group. *OpenPNM* has undergone continuous improvements, reaching its current version 3.4.0, released in November 2023. In terms of flow simulation tools, this version includes models for assigning geometric properties to networks according to specific representations. For example, pores can be represented as spheres, cubes, or pyramids, while throats can be modeled as cylinders or cuboids. These geometric models are defined as complete structures that include both pores and throats, rather than independent models for each element. However, the implemented algorithms only consider the presence of a single phase in each corner. Additionally, the invasion sequence does not depend on the chosen geometric representation, since it uses a general expression valid for pores and throats with circular cross-sections.

Chapter 3

Methodology

This chapter details the theory and mathematical formulation used to develop two-phase flow simulations applying pore network models (PNM). We begin in Section 3.1 by presenting the software used and outlining the main functions and input data required to perform flow simulations. Then, we describe the generation of pore networks, analyzing the determination of pore and throat geometrical properties from tomographic images, using two network representations: spherical pores and cylindrical throats and triangular prisms for all elements (Section 3.2), and how artificial networks are constructed to analyze the simulator’s sensitivity to different properties (Section 3.3). In Section 3.4, we discussed the phase properties related to fluid-solid interactions like contact angle, wettability, and interfacial tension. Section 3.5 presents the theory and mathematical fundamentals for fluid displacement in primary drainage and subsequent imbibition under quasi-static conditions, determining how one phase displaces the other and how phases are distributed inside pores and throats after each displacement. Section 3.6 describes the calculation of absolute and relative permeabilities. Conductance calculations for porous elements are presented for both network representations, including mathematical expressions for different phase distributions when using triangular prism elements. Finally, Section 3.7 details a calibration procedure for a pore network generated from a Berea sandstone image. This calibration requires the application of the flow calculations presented in the previous sections.

3.1 PNM softwares

Multiple software packages are used to develop PNMs. Among the commercial packages, we can mention *PoreXpert* and *Avizo*. Regarding open source software, we have *OpenPNM* and *PoreSpy*, two Python packages with strong community support. Like all open-source software, the transparency of the code and the flexible customization to perform specific tasks are important advantages. We chose these two packages as our tools for developing PNMs, using them to predict transport properties from micro-CT images.

3.1.1 PoreSpy

PoreSpy is a Python toolkit developed by [GOSTICK *et al.* \(2019\)](#) to analyze images of porous media and build PNMs from them. It uses the watershed method ([SOILLE and ANSOULT, 1990](#)) to determine the pores and throats. Using 3D micro-CT images, pores are 3D regions and throats are 2D surfaces. The process to obtain pore and throat geometric properties has two main stages: division of the pore space into regions, and conversion of regions into pores and throats. The algorithm for the first stage is explained in detail by [GOSTICK \(2017\)](#) and has the following steps:

1. identification of peaks in the distance map, which is an object that contains the Euclidean distance from each voxel to the nearest “solid” voxel, measured center to center;
2. removal of peaks considered as saddle points, which are those surrounded by other voxels with the same distance value but also connected to voxels with higher distance values;
3. merging of nearby peaks;
4. application of the watershed algorithm to determine the regions in the pore space;

5. creation of boundary regions, where we apply the boundary conditions for flow simulation;

The results from step 1 would generate an oversegmented watershed, but steps 2 and 3 prevent this, creating a subnetwork of the oversegmented watershed. That is why this stage is named SNOW by GOSTICK (2017).

The main Python libraries used on the algorithm implemented on *PoreSpy* are: `edt` (MEIJSTER *et al.*, 2000) to obtain the distance map, `scipy` (VIRTANEN *et al.*, 2020) to find (`maximum_filter` function) and remove (`binary_dilation` function) peaks, and `scikit-image` (VAN DER WALT *et al.*, 2014) to perform the watershed algorithm.

In the stage that transforms the regions into pores and throats, each region is considered a pore, and a throat represents the border between two pores. The properties of the pores are calculated using the information from the distance map and the location of the peaks, which are the pore centroids. From 0.4.0 onwards, we can choose between two methods with different accuracy, **standard** or **high**, for determining pore surface area and throat cross-sectional area. From version 2.0.0 onwards, pore volume can also be calculated using either the standard or high-accuracy methods. Lists of the data obtained at this stage using *PoreSpy* V 2.2.2 for pores and throats are in Tables 3.1 and 3.2, respectively.

Among the properties reported, the *PoreSpy* standard method for calculating the pore surface area is not accurate. Since the pore is not a closed volume, the reported surface area is the pore-solid interfacial area.

3.1.2 OpenPNM

OpenPNM is a software that allows to simulate transport in porous materials using PNM's. Created by GOSTICK *et al.* (2016), this package contains tools to simulate pore and throat invasion and predict the absolute and relative permeability of a pore network using several simplifications. Until version 3.2.0, its restrictions were:

- it can not simulate imbibition, just primary drainage;

Table 3.1: Pore properties using *PoreSpy* V 2.2.2. n_p is the number of pores.

Property	Size	Definition
coords	$n_p \times 3$	Coordinates x , y , z of the center of mass of each pore.
region label	$n_p \times 1$	Number that represents each pore, starting from zero.
region volume	$n_p \times 1$	Pore region volume. Independent of the chosen accuracy, it is calculated by the product of the number of voxels and the volume (3D image) or area (2D image) of one voxel.
equivalent diameter	$n_p \times 1$	Diameter of a sphere of volume equivalent to the volume of each pore.
local peak	$n_p \times 3$	Coordinates of the voxel farthest from the pore contours voxels, which include those belonging to the connected throats.
global peak	$n_p \times 3$	Coordinates of the farthest voxel from the solid that is inside the pore, being the voxel with the largest distance transform value. Throat voxels are not included in the pore contour.
geometric centroid	$n_p \times 3$	Coordinates of the center of mass of each pore. It is equivalent to the property pore coords
inscribed diameter	$n_p \times 1$	Diameter of the largest circle that can be inscribed in the pore. Equivalent to the distance transform of the voxel referring to the pore local peak .
extended diameter	$n_p \times 1$	Diameter of the largest circle that can be fully within the pore network and whose center is located inside the analyzed pore. It is possible that part of the circle is in the neighboring pores. Equivalent to the distance transform of the voxel referring to the pore global peak .
volume	$n_p \times 1$	Using high accuracy the results are calculated using the marching cubes algorithm. Otherwise it is calculated in the same way as region volume .
surface area	$n_p \times 1$	Calculated by the product of the area of voxel's face by the number of voxels belonging to the pore surface (standard) or using the marching cubes algorithm. In both cases, the solid-fluid surface and the pore-throats boundaries are considered as boundary voxels.
boundary	$n_p \times 1$	Bool array that indicates if a pore belongs to the surface of the porous medium (1), that is, it is a boundary pore, or if it is an internal pore (0).

Table 3.2: Throat properties using *PoreSpy* V 2.2.2. n_t is the number of throats.

Property	Size	Definition
conns	$n_t \times 2$	Indicates the pores labels connected to each throat
global peak	$n_t \times 3$	Coordinates of the voxel belonging to the throat that is farthest from the solid.
inscribed diameter	$n_t \times 1$	Diameter of the largest circle that can be inscribed to the throat. Equivalent to the distance transform of the voxel related to the throat global peak .
total length	$n_t \times 1$	Sum of the distances between the throat global peak and the pore.coords of the neighboring pores.
direct length	$n_t \times 1$	Distance between the pore coords of the neighboring pores.
perimeter	$n_t \times 1$	Product of the number of throat voxels whose transformed distance is 1, which means they are neighbors to a solid voxel, by the size of a voxel.
cross sectional area	$n_t \times 1$	Result of multiplying the number of voxels in the throat by the area of a face of a voxel (standard accuracy) or given by the difference between the sum of the pore surface area of the neighboring pores and the surface area of the region obtaining by combining these two pores, using the marching cubes algorithm (high accuracy).
equivalent diameter	$n_t \times 1$	Diameter of a circle whose area is equal to the throat cross sectional area .

- the sequence of pore and throat invasion is performed considering throats as cylindrical tubes or toroids;
- only one phase can be present on each pore or throat;
- a function to calculate flow in non-circular ducts was implemented, but it required geometrical information about the pore cross sections that *PoreSpy* does not determine.

For the flow calculation in the PNM, *OpenPNM* solves a system of linear equations using the **PyPardiso** Python package, whose version depends on the *OpenPNM* version.

3.2 Geometrical properties of pores and throats

The flow through a pore or throat depends on the geometric configuration of the element. Consequently, mathematical formulations that describe the cross-sectional area or the length of the element are essential, as these geometric properties directly influence the flow behavior.. The element cross section is predominantly characterized by the inscribed radius R and the shape factor G . The latter is a dimensionless geometric property of any surface with cross-sectional area A and perimeter P , being defined by:

$$G = \frac{A}{P^2} \quad (3.1)$$

For a triangular cross section, it is also necessary to know the values of its angles.

Regarding the pore and throat lengths, the procedure for extracting geometrical information from an image represented by voxels involves determining the center of mass of all elements, which allows the calculation of the center-to-center distance between connected elements. In this way, the mathematical expressions for calculating pore and throat lengths depend on both the center-to-center distance and the

assumed geometric representation of these elements (e.g., spheres, cylinders, prisms, etc.).

An in-depth analysis of how to obtain these properties for networks with spherical pores and cylindrical throats, and networks composed by triangular prisms is found in Sections 3.2.1 and 3.2.2 respectively.

3.2.1 Spherical pores and cylindrical throats

This is the simplest model with analytic expressions for its geometrical properties.

Shape factor

For circular cylinders, the cross section is a circle with radius R and the shape factor is:

$$G = \frac{A}{P^2} = \frac{\pi R^2}{(2\pi R)^2} = \frac{1}{4\pi} \quad (3.2)$$

Pore, throat, and conduit lengths

A pore-throat-pore conduit L_{ctc} can be defined as the path between the centers of two pores connected by a throat. When the throat center is not in the straight line that connects the two pore centers, the conduit may be defined as the sum of the straight line segments connecting each pore center to the throat center. For the simplest case of a straight conduit formed by a throat t connected to the pores j and k , the pore length L_p is calculated geometrically (see Figure 3.1a) by:

$$L_p = \sqrt{R_p^2 - R_t^2} \quad p = j, k \quad (3.3)$$

It is possible to find an analytical relationship between the lengths of the elements and the conduit, L_{ctc} . If $L_{ctc} - (L_j + L_k) \geq 0$, then the throat length L_t is:

$$L_t = L_{ctc} - (L_j + L_k) \quad (3.4)$$

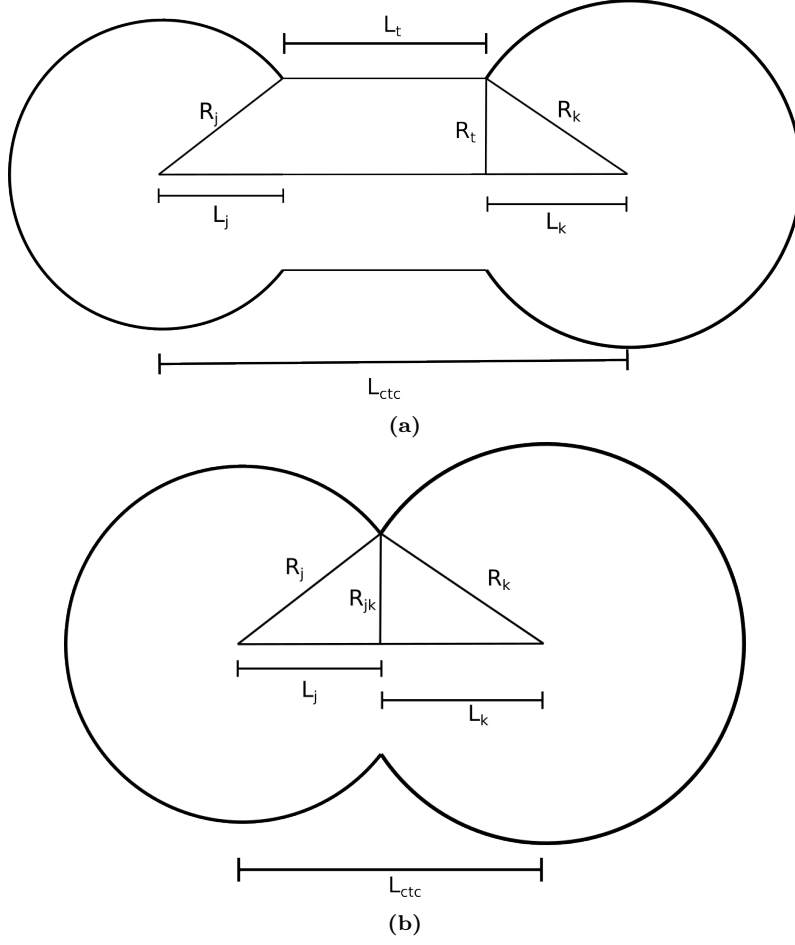


Figure 3.1: Pore length L_j considering a spherical pore: (a) non-overlapping and (b) overlapping pores.

If $L_{ctc} - (L_j + L_k) < 0$, the pores are overlapping. $L_t = 0$ as shown in Figure 3.1b, and L_p is calculated in a different way. The intersecting area between pores has a circular shape of radius R_{jk} (which is different from R_t). Then:

$$R_{jk}^2 = R_j^2 - L_j^2 = R_k^2 - L_k^2 \quad (3.5)$$

Substituting $L_k = L_{ctc} - L_j$ into Equation 3.5, we obtain:

$$R_j^2 - L_j^2 = R_k^2 - (L_{ctc}^2 + L_j^2 - 2L_{ctc}L_j) \Rightarrow L_j = \frac{R_j^2 + L_{ctc}^2 - R_k^2}{2L_{ctc}} \quad (3.6)$$

and comes from $L_k = L_{ctc} - L_j$.

GOSTICK *et al.* (2016) include this model on *OpenPNM*. The package works with a minimum throat length of $L_{min} = 10^{-15}$ to avoid possible division problems

by zero. However, we consider that L_{min} can not be a fixed value because it should depend on the size of the voxel or the conduit length. We tested two options to calculate the minimum throat length, accordingly to:

- image resolution: the minimum length value is equal to the voxel length of the image used to obtain the network, as in Equation 3.7;
- conduit length: the maximum value between the voxel length and the conduit length multiplied by a factor F_L , as in Equation 3.8

$$L_{min} = L_v \quad (3.7)$$

$$L_{min} = \max(L_v, F_L L_{ctc}) \quad (3.8)$$

3.2.2 Triangular prismatic elements

Throat shape factor

After extracting a network using *PoreSpy*, we can calculate the throat shape factor using the cross-sectional area and perimeter. However, the *PoreSpy* method to obtain P consists of counting the throat voxels that share at least one vertex with a solid voxel, which is inaccurate. We decided to represent the throats as isosceles triangles to develop a methodology to correct the shape factor.

First, we built a triangle with n_v voxels using the geometrical information of a real isosceles triangle, such as the half angles and the area. The process to do that is detailed in Appendix A.1. Having the real triangle and the one made by voxels, we obtained the real shape factor G and the one calculated using *PoreSpy* method, G_{ps} . Then, we repeated the process for different triangles with the same n_v . After that, we proposed a correlation to relate G and G_{ps} .

For all triangles with the same n_v value, our correlation ignores the triangles that have all their voxels belonging to the perimeter, except for the triangle with the

highest shape factor among them. This triangle has the lower G and G_{ps} compared to other triangles with the same n_v . So, we represent its real shape factor and *PoreSpy* shape factor as G_{min} and $G_{ps,min}$, respectively. Also, there are two different isosceles triangles with the same G , as long as $\beta_i \neq \pi/6$ (condition for an equilateral triangle). We classified them into two groups according to the value of the non-repeated half angle β_{dif} . In the first group, $\pi/6 < \beta_{dif} < \pi/4$, and in the second group, $0 < \beta_{dif} \leq \pi/6$. We developed a correlation for each group relating G and G_{ps} for a specific n_v in the following form:

$$\frac{G}{G_{min}} = \left(\frac{G_{ps}}{G_{ps,min}} \right)^\zeta \quad (3.9)$$

where ζ is the correlation parameter.

We notice that G_{min} , $G_{ps,min}$, and ζ depends on n_v . So we found expressions for the three parameters. $G_{ps,min}$ is the value when all voxels belong to the perimeter. For a triangle with n_v voxels of length L_v :

$$G_{ps,min} = \frac{A}{P^2} = \frac{n_v L_v^2}{(n_v L_v)^2} = \frac{1}{n_v} \quad (3.10)$$

G_{min} is more difficult to calculate, as it depends on the triangle with $P = n_v$ that has the highest G . We found a mathematical expression for G_{min} which is demonstrated on Appendix A.2:

$$G_{min} = \frac{289}{576 n_v} \quad (3.11)$$

Therefore, Equation 3.9 is expressed as:

$$G = \frac{289}{576} n_v^{\zeta-1} G_{ps}^\zeta \quad (3.12)$$

ζ was calculated from another correlation we built to relate it with n_v , considering separately the two triangle groups defined before, in the following form:

$$\zeta = \frac{\zeta_1}{\log(\log(n_v))} + \zeta_2 \quad (3.13)$$

where ζ_1 and ζ_2 are constant parameters. Their values are reported in Section 5.1.

Throat half-corner angles

The half-corner angles of any triangle satisfy this expression:

$$\beta_1 + \beta_2 + \beta_3 = \pi/2 \quad (3.14)$$

Assuming that $0 < \beta_1 \leq \beta_2 \leq \beta_3 < \pi/2$, it is possible to calculate β_i , depending of the group of isosceles triangles chosen. Appendix A.3 explains in detail.

For group 1, $0 < \beta_1 = \beta_2 \leq \pi/6 \leq \beta_3 < \pi/2$. β_1 and β_2 are calculated using Equation 3.15, and β_3 can be calculated by Equation 3.14.

$$\beta_1 = \beta_2 = \arctan \left(\frac{2}{\sqrt{3}} \cos \left(\frac{\arccos(-12\sqrt{3}G)}{3} - \frac{2\pi}{3} \right) \right) \quad (3.15)$$

For group 2, $0 < \beta_1 < \pi/6 < \beta_2 = \beta_3 < \pi/4$, β_2 and β_3 are calculated using Equation 3.16, and β_1 can be calculated by Equation 3.14.

$$\beta_2 = \beta_3 = \arctan \left(\frac{2}{\sqrt{3}} \cos \left(\frac{\arccos(-12\sqrt{3}G)}{3} \right) \right) \quad (3.16)$$

For the low resolution throats, those with less than 30 voxels, we assume that $G = \sqrt{3}/36$ and $\beta_i = \pi/6$. The flowchart on Figure 3.2 summarizes the calculation process described.

Pore cross-sectional geometric properties

We represent pores with prisms with triangular cross sections. Unlike throats, *PoreSpy* does not provide information related to the pore cross section. Therefore, we calculate the cross-sectional properties A , G , and β_i using the pore volume and its solid interfacial area and the cross-section areas of the connected throats. To de-

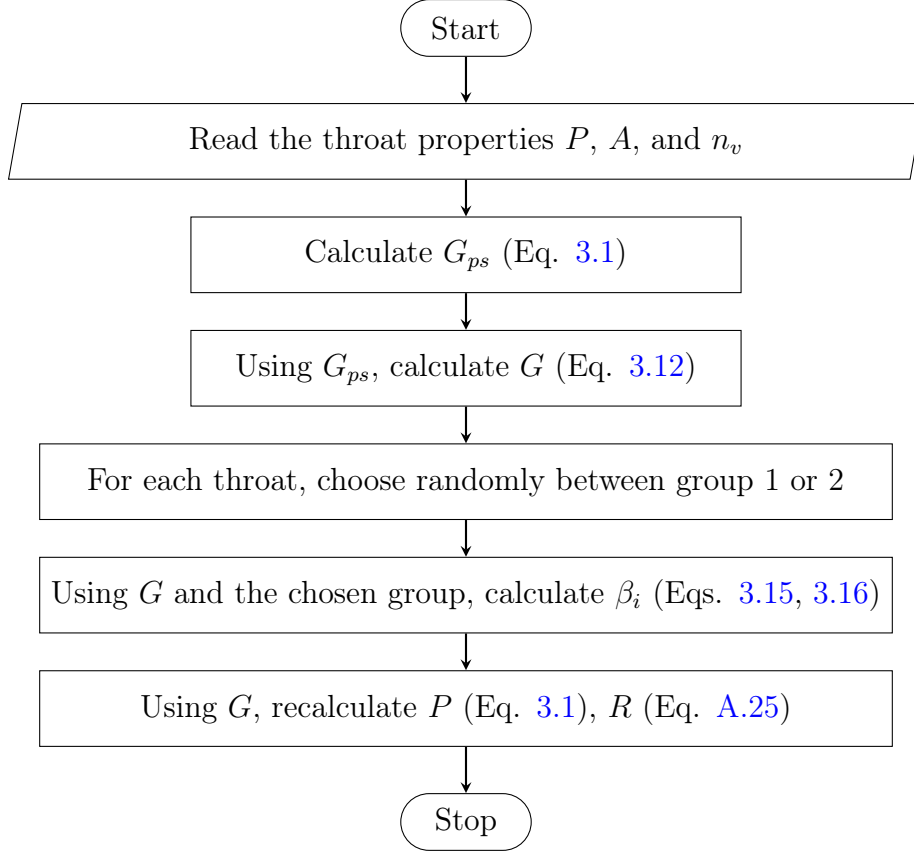


Figure 3.2: Flowchart for calculation of geometry properties of throats.

crease the number of degrees of freedom and make the problem solvable, we assume that a pore is a prism with height h and equilateral triangular cross section with edge length a . So, $\beta_i = \pi/6$ e $G = \sqrt{3}/36$.

The volume V and the superficial area S of the prism are required to calculate a . The former is equal to the pore volume and the latter is the sum of the interfacial solid-pore and the cross-section areas of all connected throats. V and S depend on a and h :

$$V = \frac{a^2\sqrt{3}h}{4} \quad (3.17)$$

$$S = \frac{a^2\sqrt{3}}{2} + 3ah \quad (3.18)$$

If h is isolated from Eqs. 3.17 and replaced in Eqs. 3.18, we obtain:

$$S = \sqrt{3} \left(\frac{a^2}{2} + \frac{4V}{a} \right) \quad (3.19)$$

Equation 3.19 tells us that for a fixed V , there are innumerable values of S . However, if we calculate the partial derivative of S with respect to a and set it equal to zero, we can calculate the minimum surface area, S_{min} , for a triangular prism of volume V . This is important, since we must identify the pores with $S < S_{min}$ and assume that for those pores, $S = S_{min}$. Differentiating S we obtain:

$$\frac{\partial S}{\partial a} = \sqrt{3} \left(a - \frac{4V}{a^2} \right) = 0 \quad \text{and} \quad \frac{\partial^2 S}{\partial a^2} = \sqrt{3} \left(1 + \frac{24V}{a^3} \right) > 0 \quad (3.20)$$

$$a = \sqrt[3]{4V} \quad (3.21)$$

$$S_{min} = 3\sqrt{3}\sqrt[3]{2V^2} \quad (3.22)$$

Continuing with the analysis of Equation 3.19, it can be written as a polynomial:

$$a^3 - \frac{2S}{\sqrt{3}}a + 8V = 0 \quad (3.23)$$

Equation 3.23 is a depressed cubic. Considering the possible values of S and V , two positive values and one negative value of a can be obtained (see Appendix B). Therefore, h must be calculated from Equation 3.17 considering only the positive values of a . Since it is undefined whether a is greater than h or vice versa, to select the pair with a more homogeneous aspect ratio, each pair (a, h) is evaluated by dividing the largest value by the smaller one.

$$\text{Aspect ratio} = \frac{\max(a, h)}{\min(a, h)} \quad (3.24)$$

The pair with the smallest result of that division is chosen and the pore cross-sectional area is calculated:

$$A = \frac{a^2\sqrt{3}}{4} \quad (3.25)$$

Using the geometric information of the cross section, we can calculate the radius of the circle inscribed in the pore cross-section area, R , (Eq. 3.26, detailed in Appendix A.3). Below, we summarize the steps to estimate the geometric properties of the pore cross sections with the information obtained by *PoreSpy*:

1. read the geometric properties of pores and throats and their connections;
2. calculate S_{min} (Eq. 3.22) and S ;
3. for those pores with $S < S_{min}$, consider $S = S_{min}$;
4. determine a from the positive roots of Eq. 3.23, and calculate h from Eq. 3.17;
5. choose the best a for each pore according to their aspect ratio (Eq. 3.24);
6. calculate the area and the radius of the inscribed circle (Eq. 3.26) for each pore cross section.

$$A = R^2 \sum_{i=1}^3 \cot \beta_i \quad (3.26)$$

Notice that we use h instead of L because that dimension does not represent the pore length. The criteria for defining pore length are explained later.

If the pore cross section is represented as an isosceles triangle, G is defined as the average of G from the connected throats. Then, a group of isosceles triangles is randomly selected. Finally, the same procedure used for throats with an isosceles triangular cross section is applied to compute β_i

Pore, throat, and conduit lengths

Although prismatic elements in network models have been used by different researchers (BLUNT, 1998; PATZEK and SILIN, 2001; VALVATNE and BLUNT, 2004), no information was found to relate the lengths of the elements that take into

account the spatial orientation of the prismatic pore. Even though not explicitly stated by these authors, we assume they ignored the effects of how the prismatic elements are connected. We consider that the calculation method must take into account the pore volume and center-to-center distances, ignoring element orientation effects. Thus, we assumed that the length values calculated by assuming spherical pores and cylindrical throats (Section 3.2.1) are valid for prismatic elements. However, different diameters can be calculated for a prism, such as the diameter of an inscribed sphere or the diameter of a sphere with the same volume as the prism. For that reason, in Section 5.3.1 we perform a comparison of permeability results that were calculated using different types of diameter, selecting the best one.

3.3 Network construction

We create cubic-lattice pore networks with a pore spacing λ . We choose between two connection modes between pores: uniform coordination number of the simple cubic lattice or multi-directional connectivity with up to 26 neighbor pores. The former mode provides a uniform connectivity $Z = 6$. The latter mode considers non-uniform connectivity varying from 1 to 26 with a mean value of 6. MACHADO *et al.* (2023) proposed an algorithm to build networks with multi-directional connectivity, which consists of three steps: first, set $Z = 26$ for all pores; then eliminate 30% of pores and the throats connected to those pores; to finally reach a mean Z of 6 by removing throats randomly.

After creating pores and throats, topological properties are defined considering that a prism with an isosceles triangle as its cross-sectional shape represents each element. The calculation of the properties involves the following steps:

1. the pore equivalent diameter $D_{eq,p}$ is defined as a random number from a distribution within the interval $[D_{p,min}; D_{p,max}]$, with mean $\bar{D}_{eq,p}$ and standard deviation σ_{Dp} , avoiding pore overlapping using the methodology described in Appendix C.2;

2. the pore length L_p is defined as a random number from a uniform distribution within the interval $[0.2\lambda; 0.7\lambda]$;
3. with $D_{eq,p}$ and L_p , calculate the pore volume $V_p = \pi D_{eq,p}^3/6$ and cross-sectional area $A_p = V_p/L_p$;
4. define the throat cross-sectional area as $A_t = \min(A_{p1}, A_{p2})F_{At}$, where F_{At} is a reduction factor and A_{p1} , A_{p2} are the areas related to the pores connected to the throat;
5. the throat length L_t is calculated with the conduit length and the equivalent diameters of the neighbor pores: $L_t = L_{ctc} - (D_{eq,p1} + D_{eq,p2})/2$, where L_{ctc} is the center-to-center distance between pores;
6. calculate throat volume $V_t = A_t L_t$;
7. the shape factor of the throat cross sections, G_t , are random numbers from a uniform distribution within the interval $[0.001G_{max}; G_{max})$, where $G_{max} = \sqrt{3}/36$ is the shape factor for an equilateral triangle and the minimum value of the interval corresponds to two different isosceles triangles: $\beta_1 = \beta_2 = 0.022^\circ$ and $\beta_3 = 89.966^\circ$; or $\beta_1 = 0.011^\circ$ and $\beta_2 = \beta_3 = 44.994^\circ$;
8. the shape factor of a pore cross section G_p is the average G_t of the connected throats.

To define the value of λ , F_{At} , and statistical properties related to $D_{eq,p}$, we examined the properties of the Berea sandstone sample after correcting the properties of the pore network extract from the tomographic image to ensure consistency with the k_{abs} values computed from direct numerical simulation, which are detailed in Section 5.5.

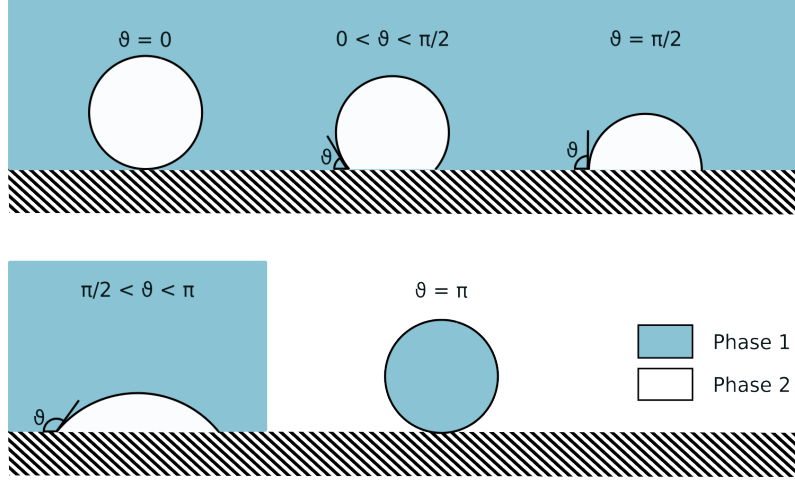


Figure 3.3: Examples of wettability. Phase 1 is taken as a reference to measure the contact angle. Values in radians. Adapted from [BLUNT \(2017\)](#)

3.4 Phase properties

3.4.1 Contact angle and wettability

In a scenario where two or more fluids are in contact with a solid surface, the contact angle θ is the angle formed between a fluid-fluid interface and the fluid-solid interface. This value is related to the affinity that the solid surface has with each phase. By convention, the contact angle in a two-phase system is the one measured from the densest phase. For two phases in contact with a solid surface at a static equilibrium, when $\theta < \pi/2$, the denser phase is called the wetting phase and the other phase is the non-wetting phase; otherwise, the non-wetting phase is the denser one ([BLUNT, 2017](#)). Figure 3.3 shows different cases of an oil-water system.

The contact angle can vary during the movement of the fluid-fluid interface. In two-phase flows, if the non-wetting phase displaces the wetting phase, the angle formed is called the receding contact angle. If it is the wetting phase that displaces the non-wetting phase, the angle is the advancing contact angle.

3.4.2 Interfacial tension

[BLUNT \(2017\)](#) explains that the interfacial tension, represented by σ , is the energy per unit area of the surface between two phases, solid or liquid, or the change in

free energy for a change in the same area. The interfacial tension between two fluids can be easily estimated if one of them is non-polar with van der Waals attraction forces. In this scenario, σ is the absolute value of the difference between the surface tensions of the two fluids, being the surface tension the energy per unit area of the interface between a liquid and its vapor in thermodynamic equilibrium.

The interfacial tensions on a system with two liquids and one solid are related by the Young equation:

$$\sigma_{nw-s} = \sigma_{w-s} + \sigma \cos \theta \quad (3.27)$$

where σ_{nw-s} , σ_{w-s} , and σ are the interfacial tensions between the non-wetting phase and the solid, the wetting phase and the solid, and the two liquids, respectively. This equation can only be applied to an equilibrium state with no reactions or external forces.

3.5 Quasi-static model for network invasion

The quasi-static model assumes that the flow is capillarity dominated and the influence of viscosity is negligible. The capillary number Ca of each phase is the parameter used to verify this condition. The quasi-static algorithm considers that $Ca = \mu v / \sigma \leq 10^{-4}$, where μ is dynamic viscosity, v is fluid velocity and σ is fluid-fluid interfacial tension. With this assumption, the elements' invasion in a porous network is determined as a sequence of configurations in mechanical equilibrium, which are obtained once at a time, that is, all interfaces remain static except for a single interface that moves. (VALVATNE and BLUNT, 2004).

ØREN *et al.* (1998) proposed a complete quasi-static algorithm to calculate the relative permeability k_{rel} of a porous medium assuming a two-phase model. Subsequently, other researchers such as PIRI (2003) and VALVATNE and BLUNT (2004) improved or complemented the algorithm. According to these references, two main stages are identified:

1. calculation of displacement events and phase distribution in all pores and throats, and
2. calculation of the relative permeability.

3.5.1 Displacement events and phase distribution

To determine the invasion order of the elements, we must know the type of invasion: if the invading phase is non-wetting, the invasion process is called **drainage**, if it is wetting, the process is called **imbibition**.

The local capillary pressure p_c is usually defined as the pressure difference between phases inside an element: $p_c = p_{nw} - p_w$, where p_{nw} and p_w are the pressure of the non-wetting and the wetting phases inside an element, respectively. However, wettability changes can occur during the imbibition process, causing the initial wetting phase to become the non-wetting one. For that reason, we define $p_c = p_1 - p_2$ being p_1 , p_2 the pressures for phases 1 and 2, respectively. Phase 1 is the invading phase during drainage and the invaded phase during imbibition, and must be the wetting phase during primary drainage, while phase 2 is the other phase. The quasi-static model assumes a negligible dynamic pressure loss throughout the porous medium. With this hypothesis, the phase pressure in all elements is the same at a given phase-distribution configuration. For that reason, the boundary conditions define p_{nw} and p_w in the whole porous medium, defining p_c for all fluid-fluid interfaces where the invading phase is connected to an inlet pore and the invaded fluid is connected to an outlet pore.

The threshold local capillary pressure required to invade the element must be known to determine if a phase invades a pore or throat. This is called the entry capillary pressure p_c^e (details of calculations in Sections 3.5.2 and 3.5.3). This property depends on:

- type of element: pore or throat;
- cross-sectional geometrical properties: for a triangular prismatic element, the

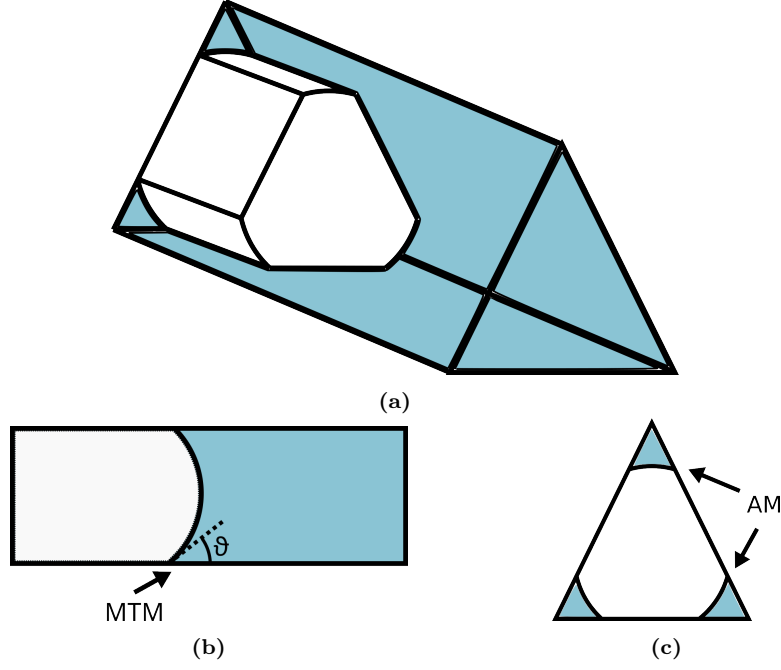


Figure 3.4: Two phases, white and light blue, in an element. a) 3D representation of a prism with a triangular cross section b) parallel lateral cut, showing the main terminal meniscus c) cross section, showing the arc menisci.

relevant properties are the shape factor G , half-corner angles β , and inscribed radius R ;

- phase properties: interfacial tension σ , and contact angle θ ;
- interface displacement type: main terminal menisci (MTM) or arc menisci (AM) displacements (see Figure 3.4);
- phase distributions in the element and its neighbors.

The values of p_c^e and p_c are compared to determine if an interface in a given element can be displaced.

3.5.2 Primary drainage

In this process, the porous medium, initially filled with the wetting phase, is invaded by the non-wetting phase. To perform the invasion, p_c is gradually increased.

During primary drainage, pores and throats are invaded by the displacement of an MTM. This type of displacement is known as the piston-like displacement or

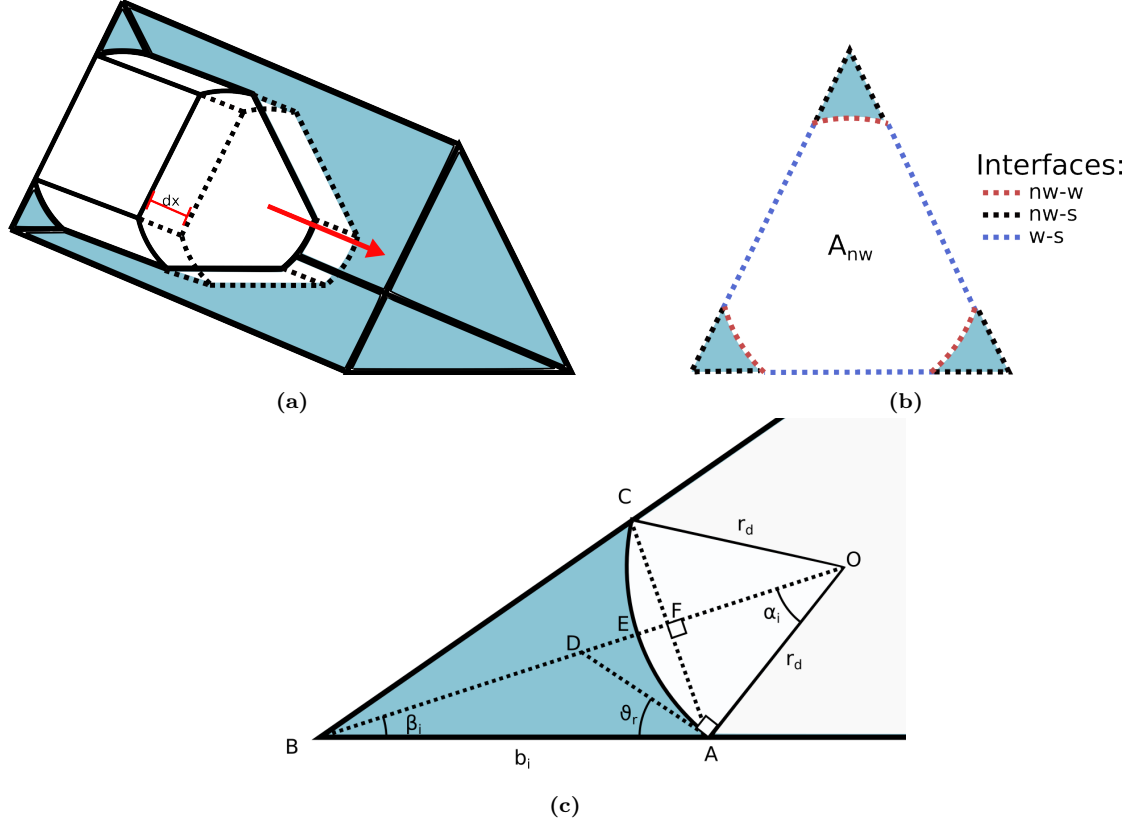


Figure 3.5: Geometrical information for a piston-like displacement event showing (a) the displacement dx , (b) the effective area and the length of the interfaces in the element cross section, and (c) the geometrical details of a corner with an AM. Before invasion, only the $nw - s$ interface exist, occupying all the perimeter of the cross-section area of the element. The variable α_i is used in Appendix D.1.1.

PLD. Figure 3.5 shows this type of displacement. The non-wetting phase occupies the center of a PNM element and the wetting phase might stay in its edges, as shown in Figure 3.5a.

The condition to invade an element is $p_c \geq p_c^e$. To calculate the p_c^e required for the displacement, the MS-P method presented by LENORMAND *et al.* (1983) and later developed by ØREN *et al.* (1998) for elements with triangular cross section is used. This method starts by comparing two mechanical equilibrium configurations, calculating the work required to displace the MTM by dx as the change in the surface free energy:

$$p_c^e A_{nw} dx = [L_{nw-w} \sigma + L_{nw-s} (\sigma_{nw-s} - \sigma_{ws})] dx \quad (3.28)$$

where A_{nw} is the cross-sectional area occupied by the non-wetting phase after the

invasion, L_{nw-w} is the fluid-fluid interface total length in all existing arc menisci, L_{nw-s} is the total length of the interface between the solid and the non-wetting phase, σ is the interfacial tension between phases, σ_{nw-s} is the interfacial tension between the solid and the non-wetting phase and σ_{w-s} is the interfacial tension between the solid and the wetting phase (see Figures 3.5a, 3.5b). Note that the subtraction in Equation 3.28 symbolizes the energy change of the fluid-solid interface due to the substitution of the wetting phase by the non-wetting phase. We can rewrite Equation 3.28 using the Young equation (Equation 3.27) and the relation between p_c^e and σ given by:

$$p_c^e = \frac{\sigma}{r_d} \quad (3.29)$$

where $1/r_d$ is the curvature of all fluid-fluid interfaces within an element, and θ_r is the receding contact angle (see Figure 3.5c). Thus, Eq. 3.28 becomes:

$$\frac{p_c^e}{\sigma} = \frac{1}{r_d} = \frac{L_{nw-w} + L_{nw-s} \cos \theta_r}{A_{nw}} \quad (3.30)$$

Appendix D.1.1 demonstrates the following expressions for A_{nw} , L_{nw-s} , and L_{nw-w} for a triangle with inscribed radius R :

$$\begin{aligned} A_{nw} &= (\text{triangle area}) - (\text{sum of corner areas}) \\ &= A - r_d^2 \sum_{i=1}^n \left[\frac{\cos \theta_r \cos(\theta_r + \beta_i)}{\sin \beta_i} + \theta_r + \beta_i - \frac{\pi}{2} \right] \\ &= \frac{R^2}{4G} - r_d^2 \Psi_1, \end{aligned} \quad (3.31)$$

$$\Psi_1 = \sum_{i=1}^n \left[\frac{\cos \theta_r \cos(\theta_r + \beta_i)}{\sin \beta_i} + \theta_r + \beta_i - \frac{\pi}{2} \right], \quad (3.32)$$

$$\begin{aligned}
L_{nw-s} &= (\text{Triangle perimeter}) - (\text{sum of non-wetting/solid interface lengths}) \\
&= \frac{R}{2G} - 2r_d \sum_{i=1}^n \frac{\cos(\theta_r + \beta_i)}{\sin \beta_i} \\
&= \frac{R}{2G} - 2r_d \Psi_2,
\end{aligned} \tag{3.33}$$

$$\Psi_2 = \sum_{i=1}^n \frac{\cos(\theta_r + \beta_i)}{\sin \beta_i}, \tag{3.34}$$

$$\begin{aligned}
L_{nw-w} &= \text{sum of non-wetting/wetting interface lengths} \\
&= 2r_d \sum_{i=1}^n \left(\frac{\pi}{2} - \theta_r - \beta_i \right) \\
&= r_d \Psi_3,
\end{aligned} \tag{3.35}$$

$$\Psi_3 = 2 \sum_{i=1}^n \left(\frac{\pi}{2} - \theta_r - \beta_i \right), \tag{3.36}$$

where Ψ_1 , Ψ_2 and Ψ_3 are variables defined to simplify these equations, n is the number of corners with the wetting phase after the invasion (number of AM), which are those that satisfy the $\beta_i < \pi/2 - \theta_r$ criterion, which is the condition for the presence of an AM with a convex surface as viewed from the wetting phase.

Substituting Equations 3.31, 3.33, and 3.35 in equation 3.30, we can get a quadratic equation for r_d , whose solution allows to calculate p_c^e as (see Appendix D.1.1):

$$p_c^e = \frac{\sigma \cos \theta_r (1 + \sqrt{1 + 4G\Psi_4 / \cos^2 \theta_r})}{R} \tag{3.37}$$

where:

$$\Psi_4 = \Psi_1 - 2\Psi_2 \cos \theta_r + \Psi_3 \tag{3.38}$$

In summary, to calculate p_c^e for a PLD, we need the phase properties σ and θ_r ,

at the end of the previous drainage process, $p_{c,max}$, and the geometric information in Figure 3.5c (demonstration in Appendix D.1.1):

$$b_i = r_{d,min} \frac{\cos(\theta_r + \beta_i)}{\sin \beta_i} = \frac{\sigma}{p_{c,max}} \frac{\cos(\theta_r + \beta_i)}{\sin \beta_i} \quad (3.39)$$

where $r_{d,min}$ is the radius of curvature of the AM at the end of the previous drainage process. During imbibition, we can express b_i in terms of the hinging contact angle $\theta_{h,i}$ and the local capillary pressure p_c :

$$b_i = \frac{\sigma}{p_c} \frac{\cos(\theta_{h,i} + \beta_i)}{\sin \beta_i} \quad (3.40)$$

Solving equations 3.39 and 3.40, we find an expression for $\theta_{h,i}$:

$$\theta_{h,i} = \arccos \left[\frac{p_c}{p_{c,max}} \cos(\theta_r + \beta_i) \right] - \beta_i \quad (3.41)$$

For an AM, the contact angle reaches value of θ_a for a specific p_c value, p'_c , calculated as follows:

$$p'_c = p_c(\theta_a, \beta_i, p_{c,max}) = p_{c,max} \frac{\cos(\theta_a + \beta_i)}{\cos(\theta_r + \beta_i)} \quad (3.42)$$

If $\theta_a + \beta_i > \theta/2$, this AM is displaced at a negative p_c . The definitions of **spontaneous** and **forced** invasion are related to the possibility of invasion at a negative p_c . The former is a phase displacement in an element at a positive local capillary pressure $p_c > 0$. The latter occurs when the phase displacement occurs at $p'_c < 0$ for all AM. That is important because, when the contact angle of an AM reaches θ_a and $p_c > 0$, the interface displaces smoothly, and b_i increases. Otherwise, for $p'_c < 0$ at any AM, the AM curvature changes sign (see Figure 3.6) and it moves instantly to the center of the element, causing its invasion (BLUNT, 1998; ØREN *et al.*, 1998). Thus, spontaneous and forced invasions do not have the same mathematical analysis.

In an imbibition process, three different mechanisms can result in the invasion

of an element:

- piston-like displacement (PLD), only for throats,
- pore body filling (PB), only for pores,
- snap off (S), for pores and throats.

VALVATNE and BLUNT (2004); ØREN *et al.* (1998) describe the theory and equations of these mechanisms.

Piston-like displacement (PLD)

As in the drainage process, this process involves the MTM inside a throat moving from one end to the other, filling the throat center with the invading phase. If a PLD takes place in an imbibition process, p_c^e is influenced by the contact angle. If $\theta_r = \theta_a$, it is possible to use the results obtained in the drainage process (Equation 3.37). Otherwise, a more elaborate analysis is required.

In the case that $p'_c > 0$ for all AM, the element invasion is spontaneous and an analysis similar to that performed in the case of drainage can be made (Equations 3.30 to 3.37). The differences are:

- when the MTM is moving, its contact angle is θ_a , which substitutes θ_r in Equation 3.30, giving:

$$\frac{p_c^e}{\sigma} = \frac{1}{r_{imb}} = \frac{L_{nw-w} + L_{nw-s} \cos \theta_a}{A_{nw}} \quad (3.43)$$

where r_{imb} is the AM radius of curvature in the imbibition process;

- if $p_c < p'_c$ for a given AM, its triple contact line is fixed and its contact angle is hinging and calculated by Equation 3.41. b_i is calculated from Equation 3.39;
- if the contact angle of an AM becomes θ_a , the interface starts to move slowly and Equation 3.44 is used to obtain b_i .

$$b_i = r_{imb} \frac{\cos(\theta_a + \beta_i)}{\sin \beta_i} \quad (3.44)$$

Notice that Equation 3.43 assumes that the space initially occupied by the invaded phase is completely filled by the invading phase. The mathematical analysis becomes complicated if we consider layer formation (an event described later in this section). For that reason, we ignore layer formation at the present implementation of this model.

With the considerations described above, Equations 3.31, 3.33, and 3.35 are substituted by:

$$A_{nw} = A - r_{imb}^2 \sum_{i=1}^n \left[\frac{\cos \theta_{h,i} \cos(\theta_{h,i} + \beta_i)}{\sin \beta_i} + \theta_{h,i} + \beta_i - \frac{\pi}{2} \right] \quad (3.45)$$

$$L_{nw-s} = \frac{R}{2G} - 2 \sum_{i=1}^n b_i \quad (3.46)$$

$$L_{nw-w} = 2r_{imb} \sum_{i=1}^n \sin^{-1} \left(\frac{b_i \sin \beta_i}{r_{imb}} \right) \quad (3.47)$$

The system of equations formed by Eq. 3.45 to 3.47 cannot be solved analytically. Thus, we must calculate r_{imb} through an iterative procedure and then calculate p_c^e . To start the iteration, we must know the values of β_i , b_i (Equation 3.39), n (the number of corners with an AM), and $p_{c,max}$ at the start of the imbibition, as well as the phase and pore properties. A proposed iteration method is shown in Figure 3.7.

It is possible to determine if a throat is invaded spontaneously ($p_c^e > 0$). Substituting the limiting value of $p_c^e = 0$ in Equation 3.43, we have $\cos(\theta_a + \beta_i) = 0$ or $\theta_a + \beta_i = \pi/2$. The maximum contact angle for spontaneous invasion $\theta_{a,max}$ is calculated using Equations 3.46 and 3.47 (see Appendix D.1.2) as:

$$\cos \theta_{a,max} = - \frac{-4G \sum_{i=1}^n \cos(\theta_r + \beta_i)}{Rp_{c,max}/\sigma - 4G (\cos \theta_r \sum_{i=1}^n \cot \beta_i - n \sin \theta_r)} \quad (3.48)$$

If $\theta_a > \theta_{a,max}$ ($p_c' < 0$), the interface curvature changes direction, and a forced invasion takes place. The value of p_c can be calculated using Equations 3.45 to 3.47 as long as the piston-like displacement can occur, that is, when the contact angle

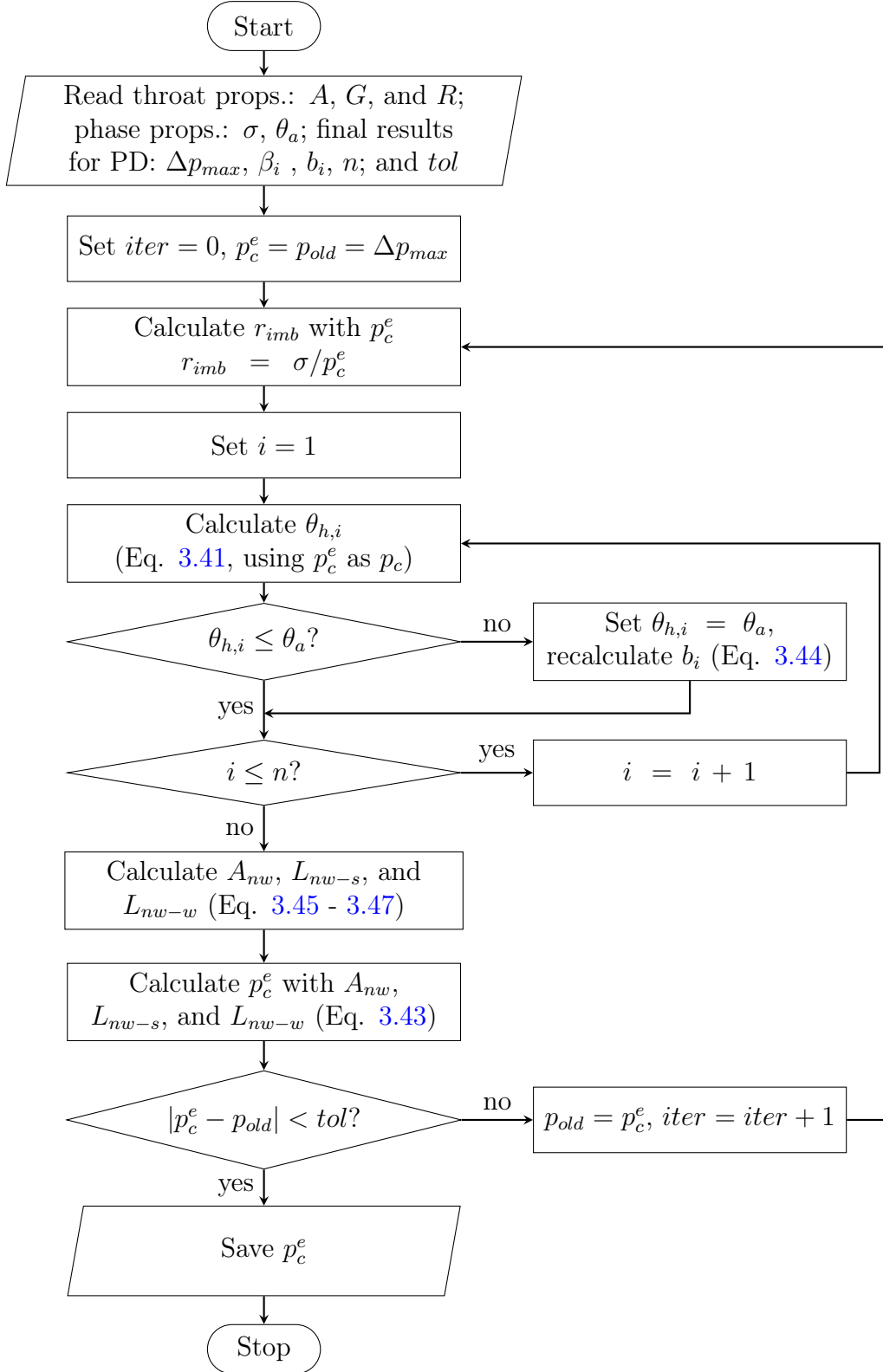


Figure 3.7: Iteration to calculate p_c^e for a throat invaded considering a PLD. $iter$ is the number of iterations. tol is the tolerance. The lower the value of i , the lower β_i value.

related to the MTM reaches the value of θ_a before any of the AM's contact angles does. If this is not achieved, snap-off takes place.

Pore body filling (PB)

Pore invasion depends on the pore geometry, the phase properties, and the phase distribution of the connected throats (LENORMAND *et al.*, 1983), as exemplified in Figure 3.8. The development of an analytic expression for pore invasion is extremely complex for pores with a large number of connected throats, a common event in a pore network. For this reason, researchers such as BLUNT (1998) and ØREN *et al.* (1998) proposed semi-empirical expressions. The analytical part of the expression comes from the method used to obtain p_c^e for a PLD. The empirical part introduces the effect of the phase distribution at the connected throats.

Following VALVATNE and BLUNT (2004), we calculated p_c^e from :

$$p_c^e = \frac{2\sigma \cos \theta_a}{R_p} - \sigma \sum_{i=1}^N \psi_i \eta_i \quad (3.49)$$

where R_p is the inscribed radius of the pore, N is the number of connected throats with the non-wetting phase at the center, ψ_i are input parameters, and η_i are random numbers between zero and one. The values of ψ_i suggested by VALVATNE and BLUNT (2004) depend on the absolute permeability k_{abs} but are independent of the assumed shape of the pore:

$$\psi_N = \begin{cases} 0 & , \text{ if } N = 1 \\ 0.03k_{abs}^{-0.5} & , \text{ if } N > 1 \end{cases} \quad (3.50)$$

k_{abs} was chosen in this model due to the relationship with the throat size distribution, and its calculation is described in Section 3.6.4.

Snap-off (S)

Snap-off occurs on pores and throats when at least one AM is displaced toward the center. The displaced AMs have contact angles equal to θ_a , and move until two of

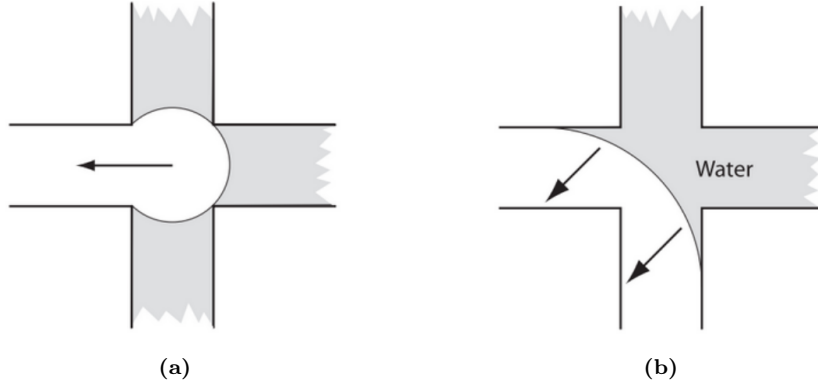


Figure 3.8: Different pore-body filling events with (a) $N = 1$ and (b) $N = 2$. Extracted from BLUNT (2017).

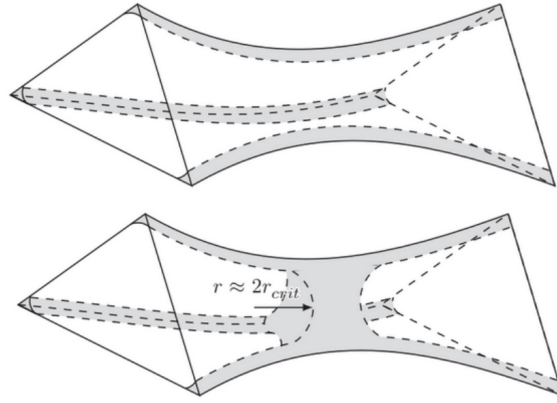


Figure 3.9: A snap-off event. Extracted from BLUNT (2017).

them collide. After the collision, the cross-section is fully filled with the wetting phase (see Figure 3.9).

The first AM contact angle to reach θ_a is always related to the sharpest corner, which is proved in Appendix D.2. For $p'_c > 0$, when the AM contact angle reaches the value of θ_a , the interface begins to move smoothly. The collision between two AMs takes place on the solid surface. There are three scenarios for collision:

1. the AM in the sharpest corner moves and collides with the AM of the largest corner (Figure 3.10a);
2. all AMs move simultaneously, and the AMs of the two sharpest corners collide (Figure 3.10b);
3. two AMs move simultaneously, and the other remains fixed.

The derivation of the relevant equations for the first two scenarios is in Appendix

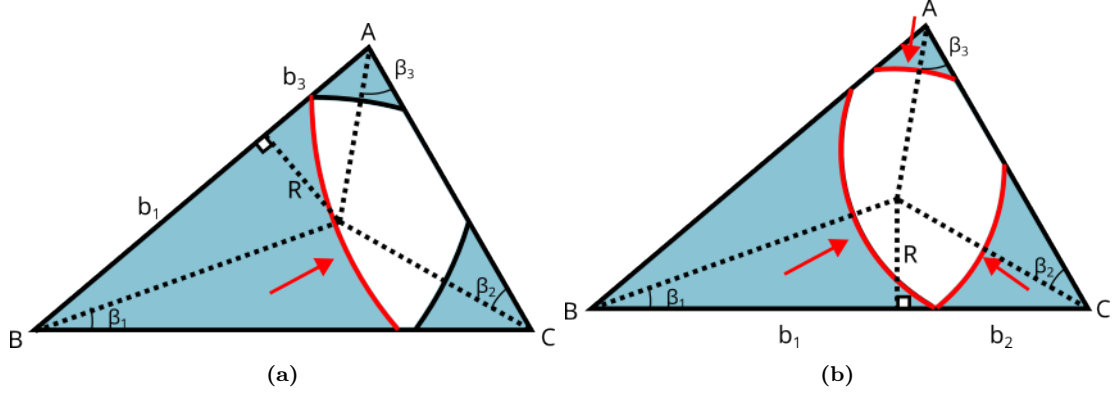


Figure 3.10: AM displacements and collision. The AMs in red are moving towards the center. We show (a) just one AM moving, and (b) all AM are moving.

D.2. For the first interface collision scenario, the equation for p_c^e is:

$$p_c^e = \frac{\sigma}{R} \left(\frac{\cos \theta_a \cot \beta_1 - \sin \theta_a + \cos \theta_{h,3} \cot \beta_3 - \sin \theta_{h,3}}{\cot \beta_1 + \cot \beta_3} \right) \quad (3.51)$$

where $\theta_{h,3}$ is the hinging contact angle related to the largest β . The equation for the second scenario is:

$$p_c^e = \frac{\sigma}{R} \left(\cos \theta_a - \frac{2 \sin \theta_a}{\cot \beta_1 + \cot \beta_2} \right) \quad (3.52)$$

Appendix D.2 details the procedure to obtain both expressions. For the third scenario, we must compare the p_c^e of the other two scenarios. The one with the highest p_c^e occurs.

If $p_c' < 0$, for an AM, it moves instantly towards the center. Thus, the analysis is performed at the moment when the AM's contact angle reaches its maximum possible value. On the other hand, the triangle geometry limits the contact angle of any AM to $\theta + \beta \leq \pi$ (see Figure 3.6). For those conditions, we can calculate p_c^e using a similar expression to the one given by Equation 3.42, with θ_a instead of θ_h for the sharpest corner:

$$p_c^e = p_{c,max} \frac{\cos(\min(\theta_a + \beta_1, \pi))}{\cos(\theta_r + \beta_1)} \quad (3.53)$$

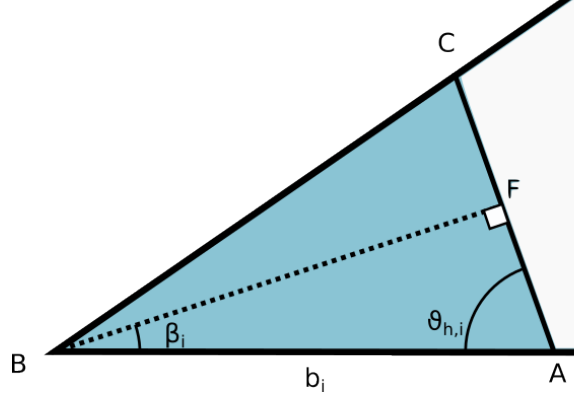


Figure 3.11: Planar fluid-fluid interface

Layer formation (LF) and collapse (LC)

After the invasion during imbibition, a layer of the non-invaded fluid can be formed in a corner if $\theta_a > \pi/2 + \beta_i$, which corresponds to the condition under which the invading phase acts as the wetting phase. Figure 3.11 shows a planar fluid-fluid interface with a hinging contact angle where $\theta_{h,i} + \beta_i = \pi/2$, which is only possible if this condition is met. The invading phase becomes wetting after $\theta_{h,i}$ increases. The invaded-phase layer, sandwiched between an inner and an outer interface as shown in Figure 3.12c, maintains the connectivity of the non-wetting phase. It can break if both interfaces collide (VALVATNE and BLUNT, 2004). If the two phases forming the interface are not trapped, layer collapse (LC) happens when:

$$p_c^e = \frac{\sigma}{b_i} \left(\frac{\cos(\arccos(2 \sin \beta_i + \cos \theta_a) + \beta_i)}{\sin \beta_i} \right) \quad (3.54)$$

The demonstration of the expressions for the layer formation and collapse is given in Appendix D.3.

After a layer collapse, we assume that a thin layer of non-wetting phase remains, maintaining the non-wetting phase connectivity. All collapsed layers can be restored in subsequent drainage processes at the same p_c^e value before collapse and with the same interface properties.

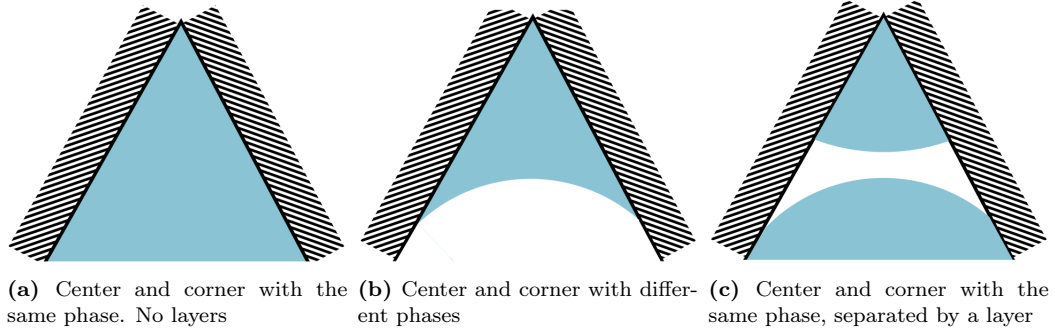


Figure 3.12: Different fluid configurations.

3.5.4 Phase locations

We define as *phase location* the position a phase can occupy inside an element. We have three possible phase locations: center, corner, and layer. Figure 3.12 shows different configurations based on the fluid in each phase location. The phase locations occupied by a fluid in a pore or throat are altered if invasion or layer collapse occurs.

During the primary drainage process, when an element is invaded, the center and corners with $\beta_i \geq \pi/2 - \theta_r$ contain the non-wetting phase. The other corners contain the wetting phase.

During the displacement in the subsequent imbibition process, a layer can be formed and subsequently collapse according to the theory explained in Section 3.5.3.

Figure 3.13 represents the configuration changes after different types of displacement.

3.5.5 Clusters

We use an algorithm similar to the one proposed by PIRI (2003) to identify clusters. The idea is to start choosing an element and selecting one of its phase locations. Then, we identify its neighboring elements and their phase locations. Once we have this information, we evaluate if the selected phase location is connected with the phase location in a neighboring element. If it is true, we move to that phase location and repeat the process until all connections are identified. All visited phase locations make up a unique cluster, represented by an index. The whole process is repeated

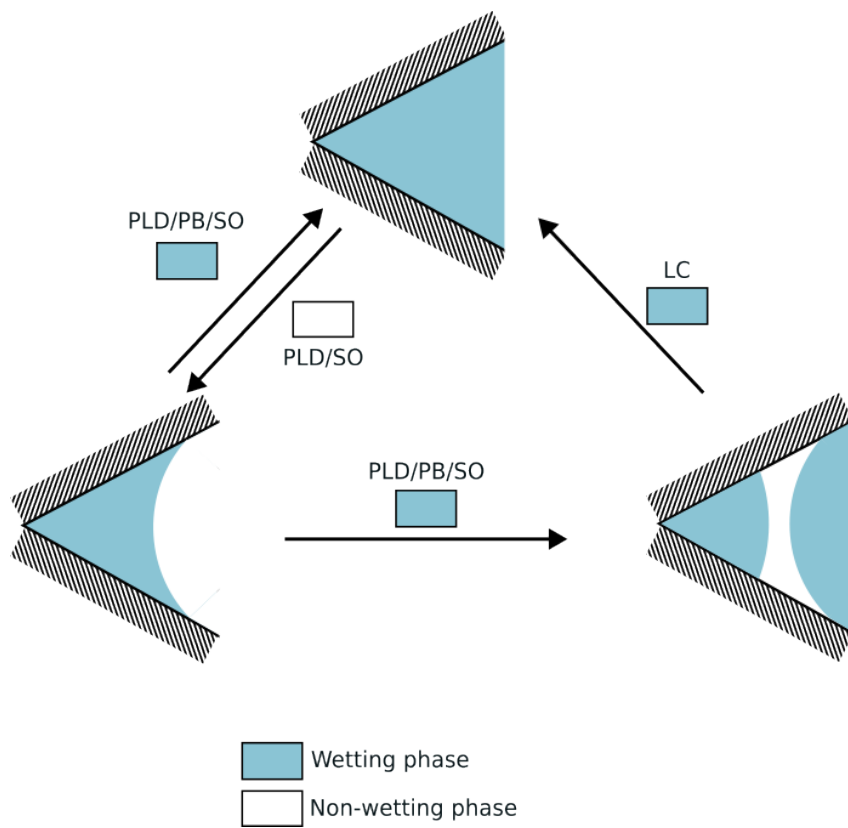


Figure 3.13: Possible displacements according to the invading phase (indicated in boxes) and the fluid configuration inside the element. The displacements considered are: piston-like displacement (PLD), pore-body Filling (PB), snap-off (SO), and layer collapse (LC).

Table 3.3: Criteria for connectivity in adjacent elements. Extracted from [PIRI \(2003\)](#).

Phase location in element 1	Phase location in element 2	Connectivity
Corner	Corner	Yes
Corner	Layer	No
Corner	Center	No
Layer	Layer	Yes
Layer	Center	Yes
Center	Center	Yes

with another phase location that still does not belong to a cluster, until we have allocated all phase locations in clusters. Figure 3.14 describes the algorithm.

The connection between two phase locations depends on its position: center, corner or layer. Table 3.3 lists the possible connections.

Trapped, non-trapped and continuous clusters

When an invasion process occurs, we must identify the trapped clusters. A trapped cluster is one that has lost connectivity with the boundary pores that control the pressure of the phase to which it belongs. To identify a trapped cluster, we follow these rules:

- if a cluster that belongs to the **invading** phase loses connectivity with the **inlet** pores, it becomes trapped.
- if a cluster that belongs to the **invaded** phase loses connectivity with the **outlet** pores, it becomes trapped.

Trapped clusters may appear by splitting a non-trapped cluster. The phase locations of a trapped cluster can not move until the cluster becomes connected again. When a cluster is trapped, its pressure is not controlled by the boundary pores. In that case, the phase pressure is modified to preserve the p_c value at the moment of trapping. That means that b_i and θ_i for the AMs do not change. Reconnection of trapped clusters occurs when the phase configuration of an element of this cluster is modified, allowing a connection between the trapped cluster and a non-trapped cluster (see Table 3.3 for connectivity options).

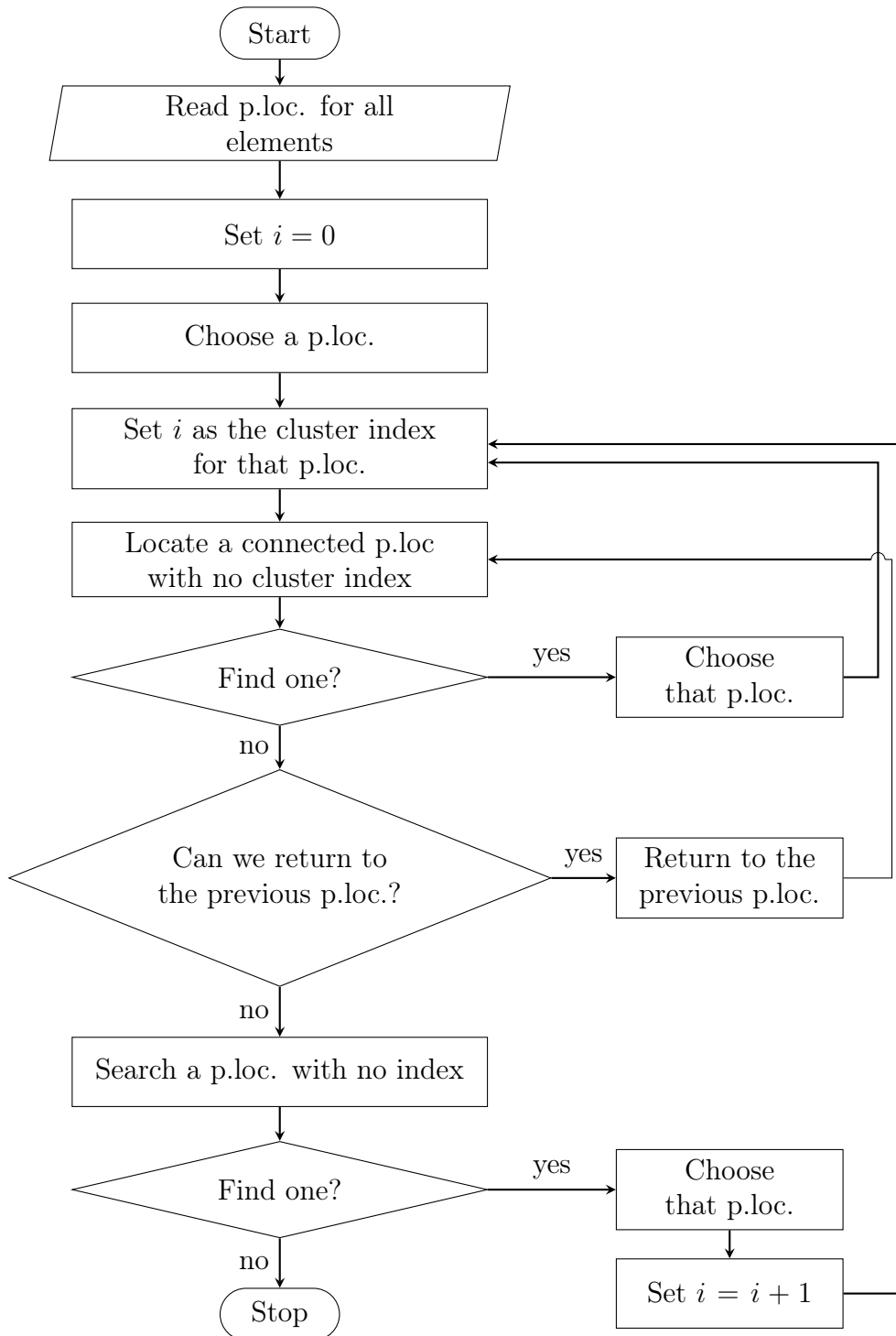


Figure 3.14: Procedure to identify clusters. “p.loc.” is the abbreviation for “phase location”

Continuous clusters are important for the phase flow calculation. These clusters, usually called sample-spanning clusters, are connected to an inlet and outlet pore. So, a non-trapped cluster is not necessarily continuous.

After assigning indexes to all phase locations, the indexes of the phase locations of the boundary pores can easily be used to identify trapped and continuous clusters.

3.5.6 Invasion simulation

For a quasi-static simulation, the pressure of each phase is the same in all elements of non-trapped clusters. That means that $p_c = p_{nw} - p_w$ is constant for all interfaces corresponding to two non-trapped clusters and is related to the pressure differences between the inlet and outlet pores $\Delta p = p_{in} - p_{out}$, imposed by the boundary conditions. For that reason, we can set the p_c values for our simulations.

Primary drainage

The invasion algorithm for primary drainage requires as input the following information:

- pore and throat properties: inscribed radius R , half corner angles β_i , shape factor G , cross-sectional area A and connections;
- phase properties: the receding contact angle θ_r and the fluid-fluid interfacial tension σ ;
- boundary conditions: pressures at inlet and outlet pores, maximum Δp desired.

The algorithm must determine which elements are invaded at a specific quasi-static state s and the minimum Δp required to reach this state.

We notice that the primary drainage process would be easy to simulate if the invaded phase remains in at least one corner of all the elements after the invasion, which is possible if $\theta_r < \pi/3$ and the sharpest corner, which always satisfy the

condition $\beta_1 \leq \pi/6$, must also fulfill the condition $\beta_1 < \pi/2 - \theta_r$. In that scenario, trapped clusters do not exist and the unique condition to invade an element is its connection to an invaded element. The only pressure-related information required to calculate multiphase flow for a quasi-static state is the actual p_c for that state.

However, if $\theta_r \geq \pi/3$, an invaded element can be completely saturated with the non-wetting phase. This can divide the initial wetting phase cluster, creating trapped clusters. As explained before, elements with trapped clusters can not be invaded. In this scenario, all the information related to the clusters in the network, including the list of p'_c values when trapped clusters lose their connectivity with the boundary pores and become trapped, must be updated after each invasion. Therefore, we propose the algorithm in Figure 3.15, which performs all possible invasions during primary drainage. Notice that Δp is defined in the first invasion and modified if the next invaded element has a $p_c^e > \Delta p$. If we decide to set $p_{c,max}$ the algorithm stops when $p_{c,s} > p_{c,max}$, saving the current invasion results for a new state with $\Delta p = p_{c,s} = p_{c,max}$.

Imbibition

The network configuration for the imbibition process is the one obtained at the maximum Δp reached at the end of the primary drainage process, which is equal to $p_{c,max}$. This configuration defines the input information required to start simulating the invasion of the wetting phase.

We consider that during imbibition, the invading phase enters the network through the same pores from which it exits during primary drainage. That means the “outlet” pores in drainage are the “inlet” pores in imbibition and the “inlet” pores in drainage are the “outlet” pores in imbibition. That being said, we must invade the inlet pores before determining which element starts to be invaded. The initial Δp , which is the pressure difference between the inlet and outlet pores, is negative. To avoid confusion, we have decided to work with p_c instead.

If an element has its center filled with the non-wetting phase, it can be invaded

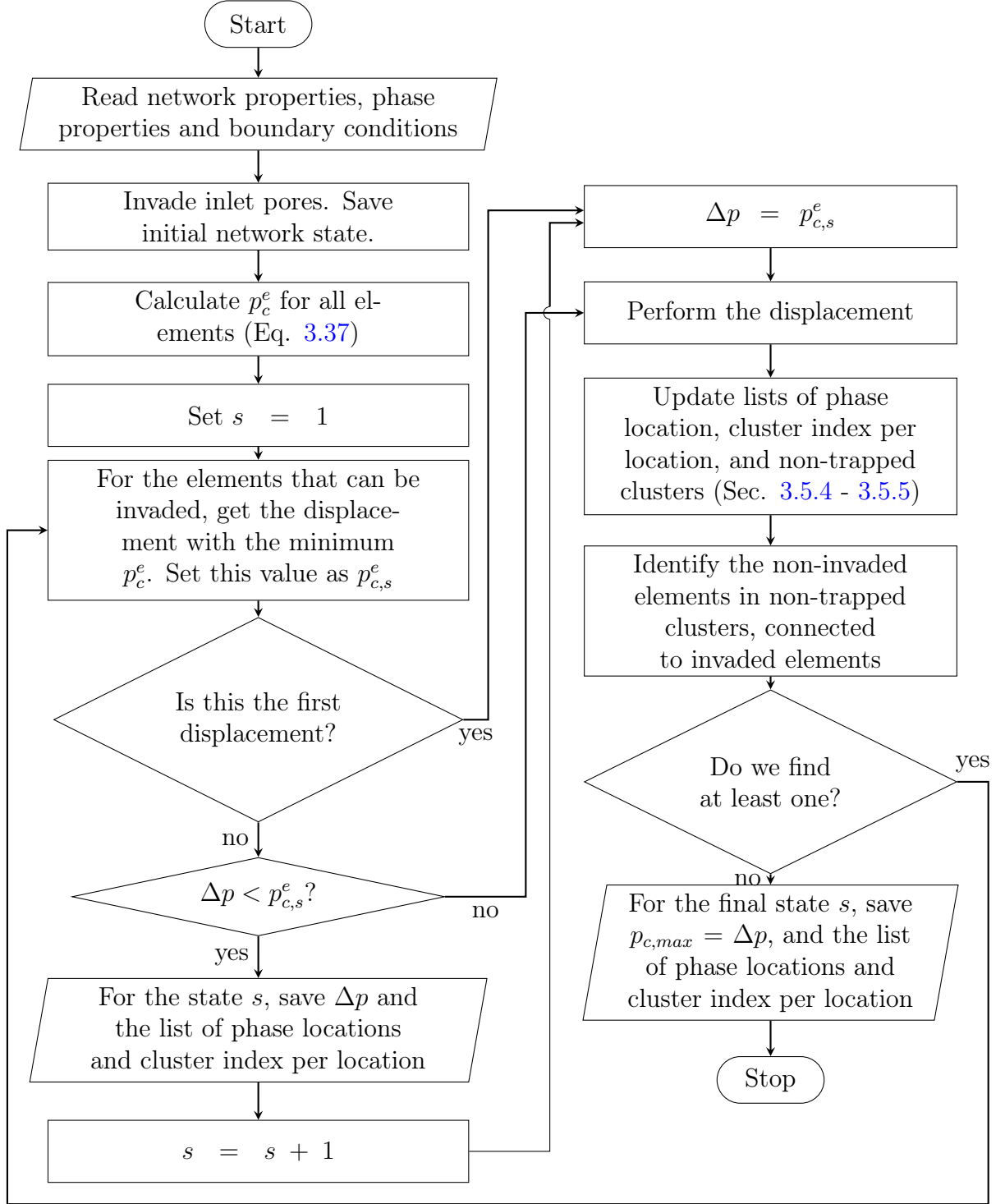


Figure 3.15: Procedure for invasion in primary drainage. $p_{c,s}^e$ is the minimum p_c^e obtained at the current invasion state.

in two different ways:

- if the invasion is caused by the MTM, that means that a connected element has its center filled with the wetting phase, the invasion may be a PLD for throats or a PB for pores;
- if the invasion is caused by an AM, snap-off may take place.

If both displacements are possible, the one with the highest p_c^e occurs. In this process, trapped clusters can appear. This is why we must update the cluster list after an element is invaded. We enforce the following rules.

- If a piston-like displacement or pore body filling occurs, the center of the invaded element belongs to the same cluster of the phase located at the center of the neighbor element responsible for its invasion.
- If a snap-off occurs, the center of the invaded element belongs to the same cluster as the phase located at the corners of the element.
- After a displacement, we need to analyze the connectivity of the invaded/non-wetting phase between the invaded element and its neighbors. If the connectivity is lost, the phase locations related to the disconnected cluster must have new cluster indexes. The new cluster connected to the **outlet** pores preserves the index. The other clusters receive new index numbers.
- After a displacement, two or more disconnected clusters related to the wetting phase can merge. The index cluster for the new one is the index number related the lower value of the previous clusters.

The invasion algorithm is shown in Figure 3.16. In this process, Δp is defined in the first invasion and modified if the next invaded element has a $p_c^e < \Delta p$.

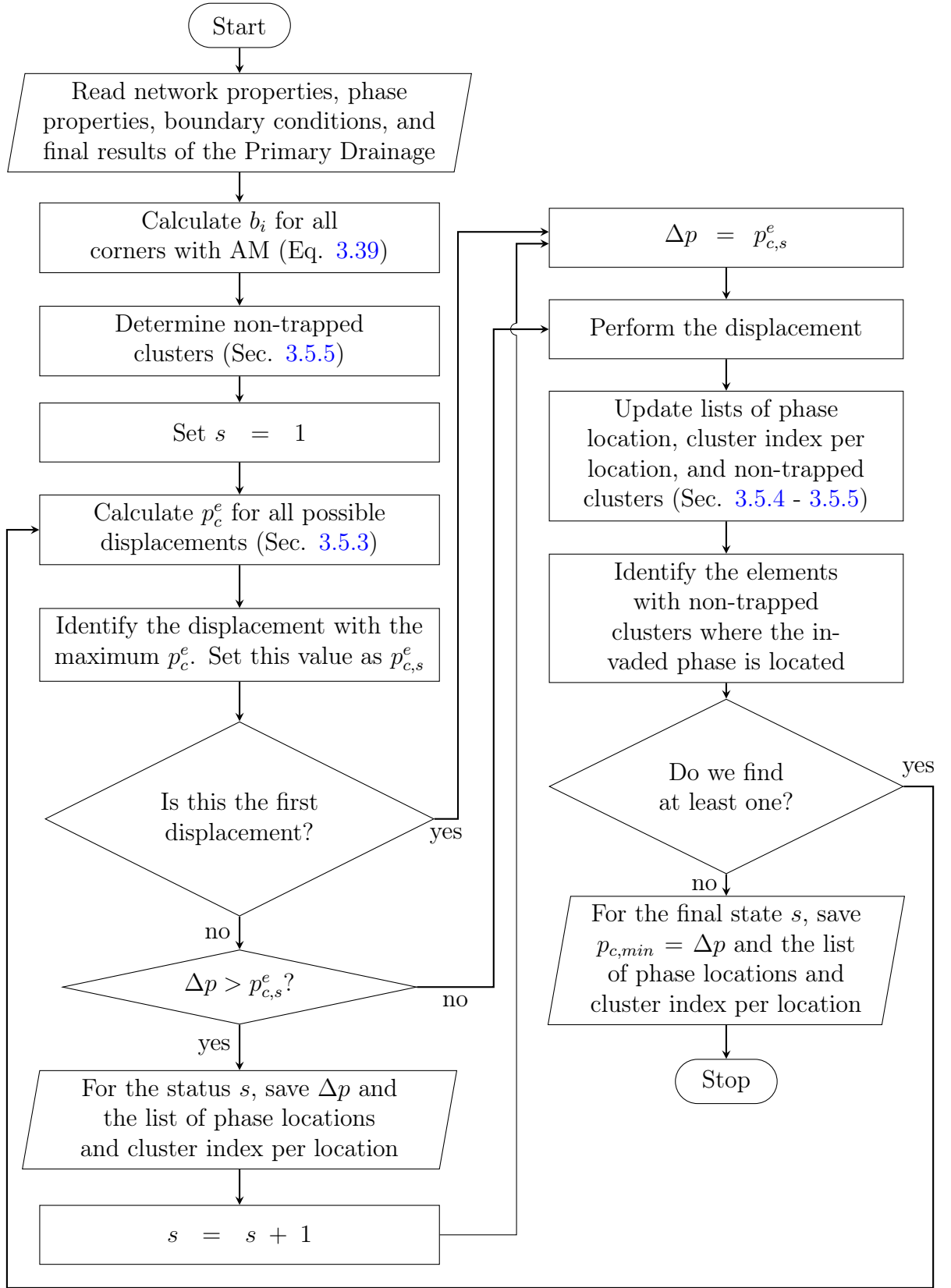


Figure 3.16: Procedure for invasion in imbibition. $p_{c,s}^e$ is the maximum p_c^e obtained at the current invasion state.

3.6 Relative permeability calculation

3.6.1 Pore and throat conductance for single-phase flow

Pores and throats are treated as pipes for flow analysis. Assuming steady fully-developed flow of an incompressible Newtonian fluid with constant viscosity, the flow rate, q , and the pressure drop, Δp , on a pipe of constant cross section and length L are related by [PATZEK and SILIN \(2001\)](#):

$$q = g \left(\frac{\Delta p}{L} + \rho \Omega \right) \quad (3.55)$$

where g is the hydraulic conductance, ρ is the fluid density, and Ω is the magnitude of the body force per unit mass in the flow direction. If gravity effects are ignored, then:

$$q = g \frac{\Delta p}{L} \quad (3.56)$$

We use the assumptions stated above to calculate g in this work.

Spherical pores and cylindrical throats

A throat is represented by a cylinder, which has a constant circular cross section. For a cylindrical pipe with cross-sectional radius R , cross-sectional area A , and length L , the Hagen-Poiseuille equation ([WHITE, 2002](#)) is used:

$$\Delta p = \frac{8\mu L q}{\pi R^4} = \frac{8\pi\mu L q}{A^2} \quad (3.57)$$

where μ is the fluid viscosity. From Equations [3.57](#) and [3.56](#) we obtain an expression for the throat conductance:

$$g = \frac{A^2}{8\pi\mu} \quad (3.58)$$

A pore is represented by a pipe with a variable circular cross section. For a pipe

with length L and a variable cross section of area A , located in the yz plane, we use the expression of resistance (the opposite of conductance) for laminar, single-phase flow in slowly-varying microchannels of arbitrary cross-section (see Figure 3.17) proposed by AKBARI *et al.* (2011):

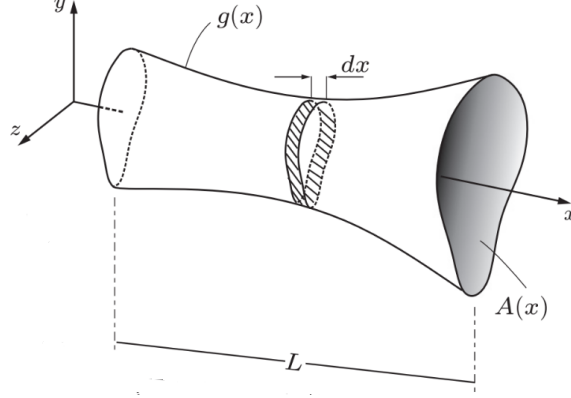


Figure 3.17: Tube with an arbitrary cross section. Extracted from AKBARI *et al.* (2011)

$$g/L = \left(16\pi^2\mu \int_0^L \frac{I_p^*}{A^2} dx \right)^{-1} \quad (3.59)$$

where I_p^* is the specific polar momentum of inertia, x is the parallel axis of the flow direction, and L is the pipe length. The length value used to calculate the conductance of a pore in a conduit is the distance from the pore center to the center of the area of the connected throat, and it is lower than the pore radius for a spherical pore ($L < R$). Equation 3.59 ignores the inertial loss. I_p^* is calculated by:

$$I_p^*(x) = \frac{I_p(x)}{[A(x)]^2} = \frac{1}{[A(x)]^2} \int_A (y^2 + z^2) dA \quad (3.60)$$

where I_p is the polar momentum of inertia. Solving Equation 3.60 for a circular cross section of radius $R^c(x)$ within a spherical pore of radius R , as in Figure 3.18, I_p^* can be calculated converting the Cartesian coordinates into polar coordinates ($y = r \cos \phi$, $z = r \sin \phi$, $dA = r dr d\phi$)

$$\begin{aligned}
I_p^* &= \frac{1}{(\pi R^c(x)^2)^2} \int_0^{2\pi} \int_0^{R^c(x)} [(r \cos \phi)^2 + (r \sin \phi)^2] r dr d\phi \\
&= \frac{1}{\pi^2 R^c(x)^4} \int_0^{2\pi} \int_0^{R^c(x)} r^3 dr d\phi \\
&= \frac{0.5\pi R^c(x)^4}{\pi^2 R^c(x)^4} = \frac{1}{2\pi}
\end{aligned} \tag{3.61}$$

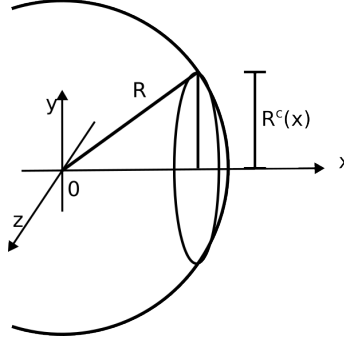


Figure 3.18: Part of an sphere with radius R , and a cross section of radius $R^c(x)$

After that, we can integrate Equation 3.59 knowing that the cross sectional area is $A = \pi R^c(x)^2 = \pi(R^2 - x^2)$ (see Figure 3.18).

$$\begin{aligned}
\int_0^L \frac{I_p^*}{A^2} dx &= \frac{1}{2\pi} \int_0^L \frac{1}{\pi^2(R^2 - x^2)^2} dx \\
&= \frac{1}{2\pi^3} \int_0^L \frac{1}{R^4(1 - (x/R)^2)^2} dx \\
&= \frac{1}{2\pi^3 R^3} \int_0^{L/R} \frac{1}{(1 - (x/R)^2)^2} d(x/R)
\end{aligned} \tag{3.62}$$

To solve the integral, we do a substitution: $u = x/R$. If $L < R$, then $u < 1$.

$$\begin{aligned}
\int \frac{1}{(1 - u^2)^2} du &= \int \left[\frac{1}{1 - u^2} + \frac{u^2}{(1 - u^2)^2} \right] du \\
&= \int \left[\frac{0.5}{1 - u^2} + 0.5 \left(\frac{1}{1 - u^2} + \frac{2u^2}{(1 - u^2)^2} \right) \right] du \\
&= 0.5 \left(\operatorname{arctanh}(u) + \frac{u}{1 - u^2} \right) + C
\end{aligned} \tag{3.63}$$

After that:

$$\int_0^L \frac{I_p^*}{A^2} dx = \frac{1}{4\pi^3 R^3} \left[\operatorname{arctanh} \left(\frac{L}{R} \right) + \frac{LR}{R^2 - L^2} \right] \tag{3.64}$$

Table 3.4: $f\text{Re}$ for different isosceles triangles. Extracted from [WHITE \(2002\)](#)

β_{dif}, deg	G	$f\text{Re}_{Dh}$
0	0	48.0
10	0.0310	51.6
20	0.0446	52.9
30	0.0481	53.3
40	0.0456	52.9
50	0.0395	52.0
60	0.0311	51.1
70	0.0214	49.5
80	0.0109	48.3
90	0	48.0

Replacing this result into Equation 3.59, we can obtain:

$$g/L = \frac{\pi R^3}{4\mu} \left[\text{arctanh} \left(\frac{L}{R} \right) + \frac{LR}{R^2 - L^2} \right]^{-1} \quad (3.65)$$

which is the simplified equation for spherical pores.

Triangular prismatic elements

To calculate the conductance for a pipe with a constant triangular cross section, [PATZEK and SILIN \(2001\)](#) proposed the general equation:

$$g = \frac{3}{5} \frac{A^2 G}{\mu} \quad (3.66)$$

Which could be approximately used for any triangular cross section of area A and shape factor G , independent of the other geometric properties. However, [WHITE \(2002\)](#) proposed the following expression to calculate flow considering isosceles triangles as cross sections.

$$q = \frac{32}{f\text{Re}_{Dh}} \frac{A^2 G}{\mu L} \Delta p \quad (3.67)$$

where the value of $f\text{Re}_{Dh}$ depends of the angles of the triangle. The terms at the left of Δp are equivalent to the conductance g . Table 3.4 and Figure 3.19 show the values of G and $f\text{Re}_{Dh}$ for each value of β_{dif} , which is the half value of the angle of the triangle that is different from the other two.

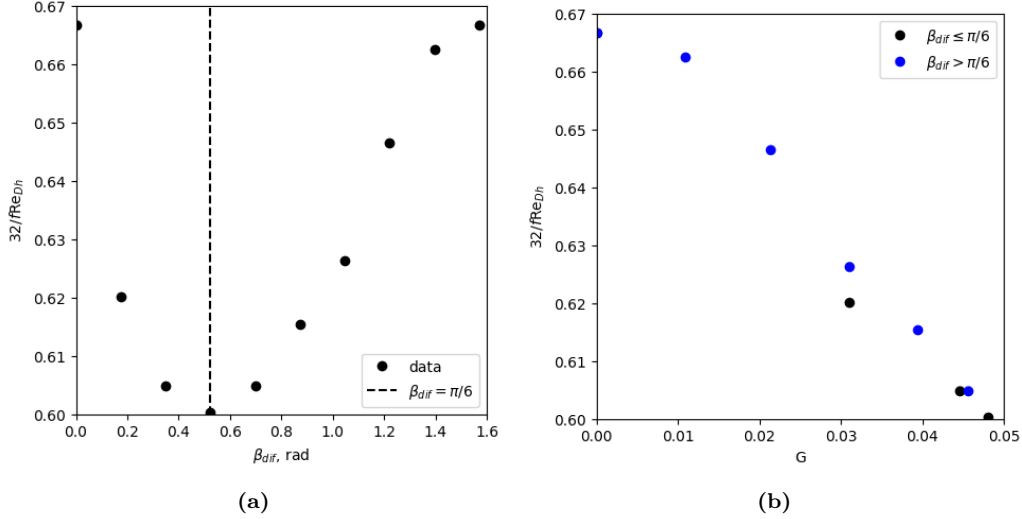


Figure 3.19: Value of $32/(fRe_{Dh})$ for different isosceles triangles. β_{dif} is the different β on the triangle.

After comparing the expressions from PATZEK and SILIN (2001) and WHITE (2002), we decided to use the latter because it gives a more accurate conductance for the geometry of an isosceles triangle, which is one of our hypotheses. However, we decided to rewrite it in a similar way to Equation 3.66. To do that, we write Equation 3.67 using a correction factor F_g :

$$q = 0.6F_g \frac{A^2 G}{\mu L} \Delta p \quad (3.68)$$

F_g is a bijective function which depends on the non-repeated half angle β_{dif} . We tested trend lines to estimate F_g and the results are in Section 5.2

Boundary elements

The network obtained by *PoreSpy* has boundary pores, which were created by the software to impose boundary conditions. Those pores are part of only one conduit, which we named as a “boundary conduit”. Since the throat of a boundary conduit was also created by the software, the conductance of a boundary conduit must depend only on the non-boundary pore. Thus, for the boundary pores and throats, $g = \infty$. We consider that we can represent that pore as a pipe. If its cross section is a circle, we use Equation 3.58 with $A = \pi R_p^2$. If its cross section is a triangle, A_p

is calculated as in Section 3.2.2.

3.6.2 Pore and throat conductance for multiphase flow

We define expressions to calculate the flow conductance for all phase locations in an element. The expressions are used for elements with simultaneous occupation of both phases, which are those represented by triangular prisms. We use the work of VALVATNE and BLUNT (2004) as the main reference. The phase properties are constant and gravitational effects are ignored.

Phase at an element center

Regarding the existence of different phases at corners, PIRI (2003) and VALVATNE and BLUNT (2004) use an equation analogous to Equation 3.66, replacing the total cross-sectional area with the cross-sectional area occupied by the phase at the cross-section center. By the same logic, we decided to use Equation 3.68, which is more accurate if the cross section is represented by an isosceles triangle, using the area occupied by the phase at the center.

Phase at an element corner

For the conductance of the phase located at a corner, the semiempirical correlation proposed by VALVATNE and BLUNT (2004) was used. This correlation assumes a no-slip boundary condition of the element walls. If a layer is present, the calculation uses the information of the region delimited by the interface closest to the corner, which is the inner interface. First, for an specific corner, its corner area A_{co} , perimeter P_{co} , and shape factor G_{co} are calculated by:

$$A_{co} = \left(\frac{b \sin \beta}{\cos(\theta + \beta)} \right)^2 \left(\frac{\cos \theta \cos(\theta + \beta)}{\sin \beta} + \theta + \beta - \frac{\pi}{2} \right) \quad (3.69)$$

$$P_{co} = 2b \left(1 - \frac{\sin \beta}{\cos(\theta + \beta)} \left(\theta + \beta - \frac{\pi}{2} \right) \right) \quad (3.70)$$

$$G_{co} = \frac{A_{co}}{P_{co}^2} \quad (3.71)$$

where β is the half-corner angle and b is the AM distance to the corner. The expressions for A_{co} and P_{co} are proved in Appendix E. G_{co} is used to calculate a conductance factor κ_{co} with a correlation proposed by VALVATNE and BLUNT (2004). This correlation also requires the shape factor assuming a planar fluid interface, represented by $G_{r \rightarrow \infty}$:

$$G_{r \rightarrow \infty} = \frac{\sin \beta \cos \beta}{4(1 + \sin \beta)^2} \quad (3.72)$$

The correlation is:

$$\kappa_{co} = 0.364 + 0.28 \frac{G_{r \rightarrow \infty}}{G_{co}} \quad (3.73)$$

Finally, the corner conductance g_{co} is calculated:

$$g_{co} = \kappa_{co} \frac{A_{co}^2 G_{co}}{\mu_{p,co}} \quad (3.74)$$

Phase at an element corner layer

To proceed with the derivations, we use the geometric data provided in Figure 3.20. In this figure, two fluid–fluid interfaces are shown: the one closest to the corner is referred to as the inner interface, and the one farthest from the corner is the outer interface. All properties related to the inner interface are denoted with the subscript *in*, while those related to the outer interface use the subscript *o*.

First, we calculate two dimensionless numbers related to the corner areas delimited by the outer interface \tilde{A}_o , and the inner interface \tilde{A}_{in} . These are obtained by dividing each area (Eq. 3.69) by the square distance from the corner to the outer interface b_o . For the outer interface:

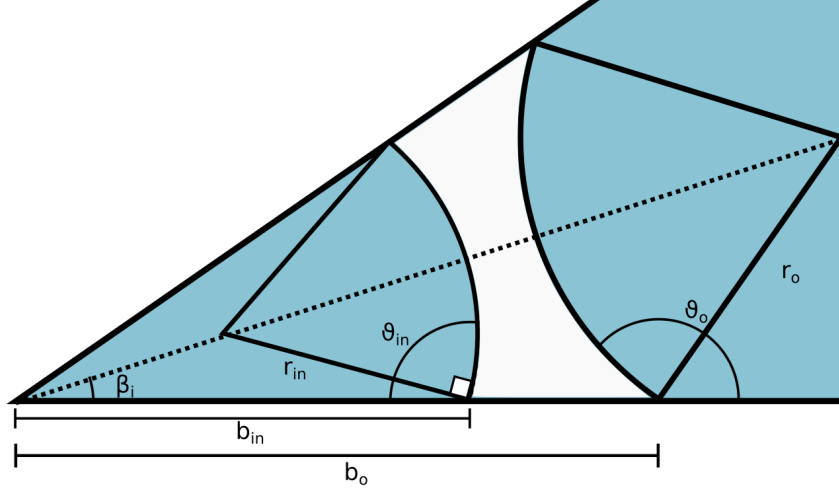


Figure 3.20: Geometrical analysis of a corner layer.

$$\tilde{A}_o = \frac{A_o}{b_o^2} = \left(\frac{\sin \beta}{\cos(\theta_o - \beta)} \right)^2 \left(\frac{\cos \theta_o \cos(\theta_o - \beta)}{\sin \beta} - \theta_o + \beta + \frac{\pi}{2} \right) \quad (3.75)$$

where θ_o is the contact angle measured from the outer interface and A_o is the cross-sectional corner area limited by the outer fluid-fluid interface. For the inner interface:

$$\tilde{A}_{in} = \frac{A_{in}}{b_o^2} = \left(\frac{\tilde{b}_{in} \sin \beta}{\cos(\theta_{in} + \beta)} \right)^2 \left(\frac{\cos \theta_{in} \cos(\theta_{in} + \beta)}{\sin \beta} + \theta_{in} + \beta - \frac{\pi}{2} \right) \quad (3.76)$$

where θ_{in} is the contact angle measured from the inner interface, A_{in} is the cross-sectional corner area limited by the inner fluid-fluid interface, and $\tilde{b}_{in} = b_{in}/b_o$, with b_{in} representing the distance from the corner to the inner interface length. The subtraction between both dimensionless areas gives us the dimensionless layer area \tilde{A}_l .

$$\tilde{A}_l = \tilde{A}_o - \tilde{A}_{in} \quad (3.77)$$

Then, the dimensionless lengths of the outer interface \tilde{L}_o and the inner interface \tilde{L}_{in} are calculated. These are also obtained by dividing the fluid-fluid interface (Eq. E.2 in Appendix E) by b_o .

$$\tilde{L}_o = \frac{L_o}{b_o} = \frac{2 \sin \beta}{\cos(\theta_o - \beta)} \left(\frac{\pi}{2} - \theta_o + \beta \right) \quad (3.78)$$

$$\tilde{L}_{in} = \frac{L_i}{b_o} = \frac{2\tilde{b}_i \sin \beta}{\cos(\theta_i + \beta)} \left(\frac{\pi}{2} - \theta_i + \beta \right) \quad (3.79)$$

where L_{in} and L_o are the inner and outer interface lengths, respectively. Figure 3.12c shows that the layer perimeter is composed of the length for two fluid-fluid interfaces and two solid-fluid interfaces. The length of the total solid-fluid interface is $2(b_o - b_{in})$, which means that its dimensionless length is $2(1 - \tilde{b}_{in})$. Thus, the layer shape factor G_l is obtained by dividing the dimensionless layer area by the square of the dimensionless layer perimeter:

$$G_l = \frac{\tilde{A}_l}{(\tilde{L}_o + \tilde{L}_{in} + 2(1 - \tilde{b}_{in}))^2} \quad (3.80)$$

The dimensionless conductance \tilde{g}_l was calculated using the empirical equation proposed by VALVATNE and BLUNT (2004):

$$\ln \tilde{g}_l = \kappa_1 \ln^2(\tilde{A}_l^3 G_l) + \kappa_2 \ln(\tilde{A}_l^3 G_l) + \kappa_3 \quad (3.81)$$

where $\kappa_1 = -0.02401$, $\kappa_2 = 0.2840$ and $\kappa_3 = -2.953$. Those values were obtained by comparing the results of the proposed layer conductance correlation with results obtained by numerical finite element simulations. Then, the layer conductance g_l can be calculated by:

$$g_l = \frac{b_o^4 \tilde{g}_l}{\mu} \quad (3.82)$$

3.6.3 Conduit conductance

A conduit is the path that connects the center of two pores that are linked by the same throat. For a two-phase flow simulation, the conduit conductance must be calculated for each phase that belongs to a sample-spanning cluster (connected with

inlet and outlet pores). Analyzing a conduit formed by the pores j, k and the throat t , the conduit conductance g_{ctc} is calculated using the conductance and length of each element.

$$\frac{g_{ctc}}{L_{ctc}} = \left(\frac{L_j}{g_j} + \frac{L_t}{g_t} + \frac{L_k}{g_k} \right)^{-1} \quad (3.83)$$

where L_{ctc} is the conduit length. Section 3.2 explains how to obtain L_j , L_t , and L_k . This expression for the conduit conductance is used for both single and two-phase scenarios, considering the phase occupancy.

3.6.4 Transport properties of the pore network

Flow rate calculation for each phase

The flow rate of each phase through the pore network is the sum of the flow rates through all sample-spanning clusters of this phase. For each sample-spanning cluster, a linear system of equations, one equation per conduit, is solved. Assuming two pores j, k connected by a throat t , the conduit flow rate q_{ctc} is the flow rate through the throat q_t and is calculated using the pore pressures p_j , p_k , and the conduit properties:

$$q_{ctc} = q_t = \frac{g_{ctc}}{L_{ctc}}(p_j - p_k) \quad (3.84)$$

Considering the hypothesis of incompressible fluids, the net flow rate at each pore is zero ($\sum_j q_{ctc} = 0$), generating a linear system to determine the pressures at all pores of a cluster.

Absolute permeability

The absolute permeability k_{abs} gives information about how easily a phase flows through the porous medium. A common expression for its calculation is derived from Darcy's law:

$$k_{abs} = \frac{q_{pn}\mu L_{pn}}{A_{pn}\Delta p} \quad (3.85)$$

where A_{pn} is the cross-sectional area of the porous medium, L_{pn} is the length of the porous medium, equivalent to the distance between the inlet and outlet regions, q_{pn} is the phase flow rate with viscosity μ , and Δp is the pressure difference across the porous medium.

Relative permeability

The relative permeability for a phase k_{rel} is the ratio between the flow rate for that phase in a two-phase flow system (q_{mph}) and in a single-phase flow system (q_{sph}) for the same boundary conditions:

$$k_{rel} = \frac{q_{mph}}{q_{sph}} \quad (3.86)$$

3.6.5 Algorithm to calculate relative permeability

The information saved for a specific quasi-static state during primary drainage or imbibition simulation (See Section 3.5.6) is used to calculate the flow rate for each phase that occupies the network, consisting of:

- list of phase locations for this phase;
- list of cluster indexes for all phase locations;
- cross-sectional areas for the phase locations and;
- for each corner, the presence of inner (subscript *in*) and outer (subscript *o*, used when two layers are present) AM, contact angles θ_{in} , θ_o , and interface distances b_{in} , b_o .

In addition, input properties required to simulate invasion are also needed now. These properties are:

- element properties: length L , cross-sectional inscribed radius R , and their connections to other elements;
- phase properties: interfacial tension σ , viscosity μ ;
- boundary conditions: Inlet and outlet pores, inlet pressure p_{int} and outlet pressure p_{out} . If Δp is given instead, we assume that $p_{int} = \Delta p$ and $p_{out} = 0$.

With this information, we determine the multiphase flow rate q_{mph} as indicated in Figure 3.21. Finally, the relative permeability is computed using Equation 3.86.

3.7 Berea pore network calibration

The absolute permeability values of the Berea pore network must be close to the values obtained by MACHADO *et al.* (2024), using direct numerical simulations (DNS) in the domain obtained from the micro-tomographic images of the Berea sandstone sample. We propose a correction formula to modify the throat radius R_t to calibrate our network:

$$R_{t,new} = R_{t,old} + (F_{R1} \min(R_j, R_k) - R_{t,old}) F_{R2} \quad (3.87)$$

where R_j and R_k are the radii of the neighbor pores, and F_{R1} and F_{R2} are correction factors. We set $F_{R1} = 0.7$ to keep the throat's diameter smaller than that of the connected pores. F_{R2} is calculated through iteration, which is described in Section 4.2.

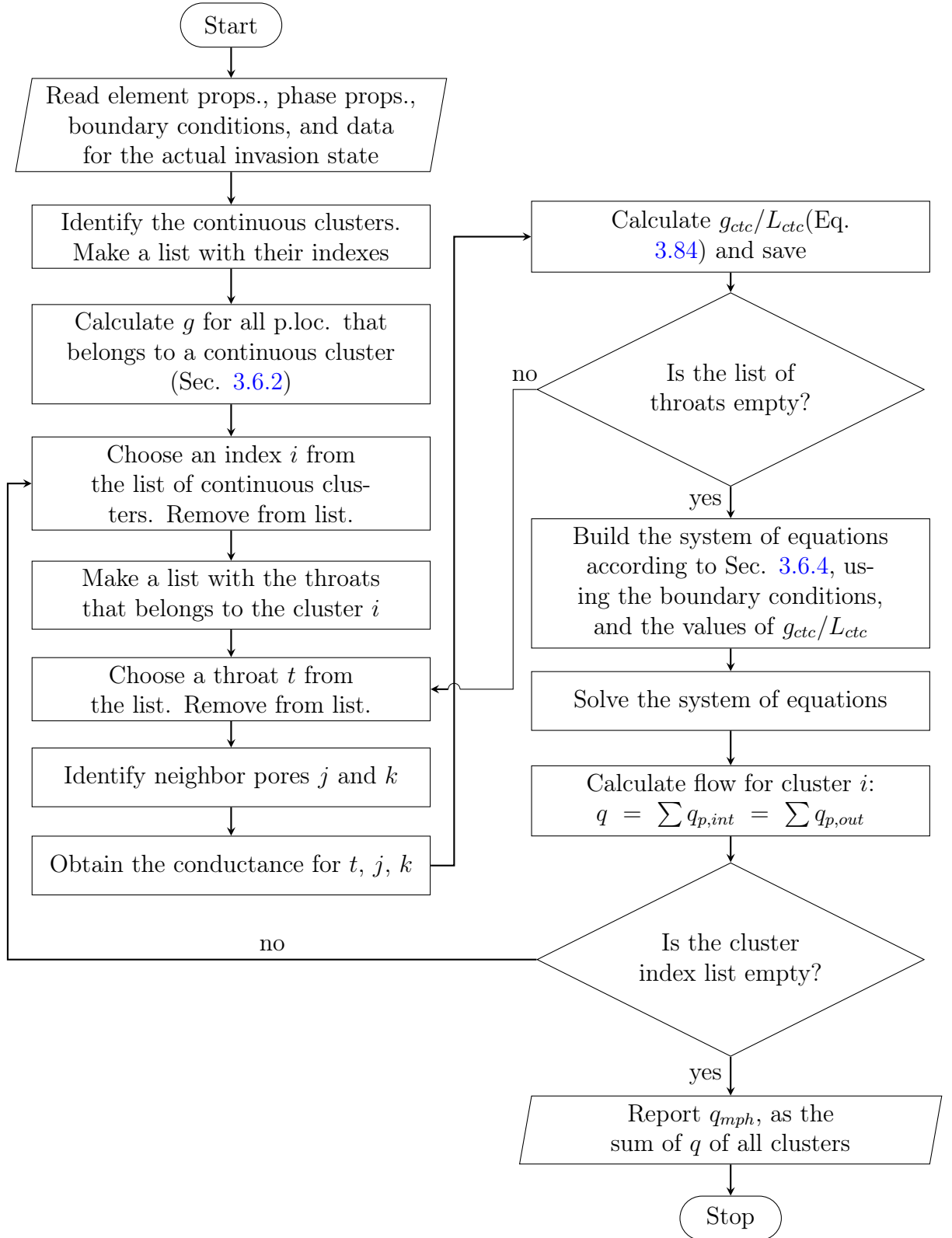


Figure 3.21: Algorithm to calculate flow rate for one phase during a specific quasi-static state. $q_{p,int}$ and $q_{p,out}$ are the phase flow rate on an inlet or outlet pore, respectively. p.loc. means “phase locations”.

Chapter 4

Numerical Procedure

4.1 Determination of parameters of correlations

We had to estimate parameters that are used to correct the *PoreSpy* results for the throat shape factor (Equations 3.12 and 3.13 in Section 3.2.2), and to calculate the correction factor for the conductance on an isosceles triangular prism (Equation 3.68 in Section 3.6.1). We estimated these parameters using the `scipy.ODR` Python package, which solves orthogonal distance regression (ODR) problems. This solution requires a set of data (x_i, y_i) , $i = 1, \dots, j$, where the values of y_i are a function of x_i and a set of unknown parameters represented by B , such that:

$$y_i = f_i(x_i + \delta_i; B) - \epsilon_i \quad (4.1)$$

where δ_i and ϵ_i are the unknown errors of x_i and y_i respectively, and f_i are the proposed model. B , δ_i , and ϵ_i must be estimated in order to minimize a given objective function. The simplest function would be:

$$\min \sum_{i=1}^j (\epsilon_i^2 + \delta_i^2) \quad (4.2)$$

but we can introduce weights in the minimization problem and define the objective function as:

$$\min \sum_{i=1}^j (w_{\epsilon i} \epsilon_i^2 + w_{\delta i} \delta_i^2) \quad (4.3)$$

where $w_{\delta i}$ and $w_{\epsilon i}$ are obtained by dividing 1 by the variance of x_i and y_i respectively, as indicated by [BOGGS *et al.* \(1992\)](#).

To calculate ζ (Eq. 3.12) and F_g (Eq. 3.68) we did not use any weights. However, we determine the standard deviation for all ζ values obtained for different n_v values, which were used to calculate $w_{\epsilon i}$ when estimating ζ_1 and ζ_2 (Eq. 3.13). We used *SciPy* version 1.9.1, and values for non-mentioned parameters, like tolerance or iterations, were the package's default values.

4.2 Network calibration using the absolute permeability

To obtain absolute permeability values close to our reference values, representing pores and throats as triangular prisms, we estimate F_{R2} from Equation 3.87 using a binary search in the interval $[0, 1]$. Our objective function is:

$$\min \sum e_{rel} = \min(e_{rel,x} + e_{rel,y} + e_{rel,z}) \quad (4.4)$$

where $e_{rel,x}$, $e_{rel,y}$, $e_{rel,z}$ are the relative errors of the absolute permeability calculated for the flow in the x , y , and z directions, respectively. As the relative errors preserve their sign (i.e., we do not use their absolute values), $\sum e_{rel}$ is always negative when evaluated at the upper bound. Thus, at each iteration, if the value of $\sum e_{rel}$ evaluated at the midpoint is positive, we choose the upper half of the interval for the next iteration; otherwise, we choose the lower half. . The binary search ends when the absolute value of the difference between the values of $\sum e_{rel}$ of the two last iterations was less than 10^{-5} .

4.3 Tuning network porosity and permeability

MACHADO *et al.* (2023) proposes an algorithm that tunes the network's absolute permeability k_{abs} and porosity Φ by tweaking the mean value of the throat diameter distribution and the mean value of the pore diameter distribution, respectively. This algorithm considers a network represented by spherical pores and cylindrical throats. Our method is based on that algorithm, tuning k_{abs} by adjusting F_{At} , and Φ by adjusting $\bar{D}_{eq,p}$. We use the binary search method for tuning. For F_{At} , the low value is 0, and the high value is 0.7. The search ends if:

$$e_{rel,k} = \left| \frac{k_{abs}^{cal} - k_{abs}^{ref}}{k_{abs}^{ref}} \right| < 0.1\% \quad (4.5)$$

where $e_{rel,k}$, is the relative error for k_{abs} , k_{abs}^{cal} is the calculated k_{abs} , and k_{abs}^{ref} , is the reference k_{abs} . Figure 4.1 shows the corresponding binary search algorithm.

For $\bar{D}_{eq,p}$, the low value is $D_{p,min}$ and the high value is $(D_{p,min} + D_{p,max})/2$ ($D_{p,min}$ and $D_{p,max}$ are the parameters used to construct the network as explained in Section 3.3). We use that high value instead of $D_{p,max}$ to avoid overlapping pores at the iteration start. Before starting the binary search, the two vectors required for the algorithm to avoid pore overlapping must be created (see Appendix C.2): the vector containing the values of $\mathbb{F}_{rel}^T(D_{eq,p})$ which is the cumulative distribution of $D_{eq,p}$, and the vector \mathbf{p} which contains the pore order. The search ends if:

$$e_{rel,\Phi} = \left| \frac{\Phi^{cal} - \Phi^{ref}}{\Phi^{ref}} \right| < 0.1\% \quad (4.6)$$

where $e_{rel,\Phi}$ is the relative error for Φ , Φ^{cal} is the calculated Φ , and Φ^{ref} is the reference Φ . Figure 4.2 shows the corresponding binary search algorithm.

Since adjusting either F_{At} or $\bar{D}_{eq,p}$ modifies both k_{abs} and Φ if the pore space volume is attributed to the pores and throats, we employ an iterative procedure, which ends if:

- the absolute difference in F_{At} before and after its adjustment is less than 0.001,
- or

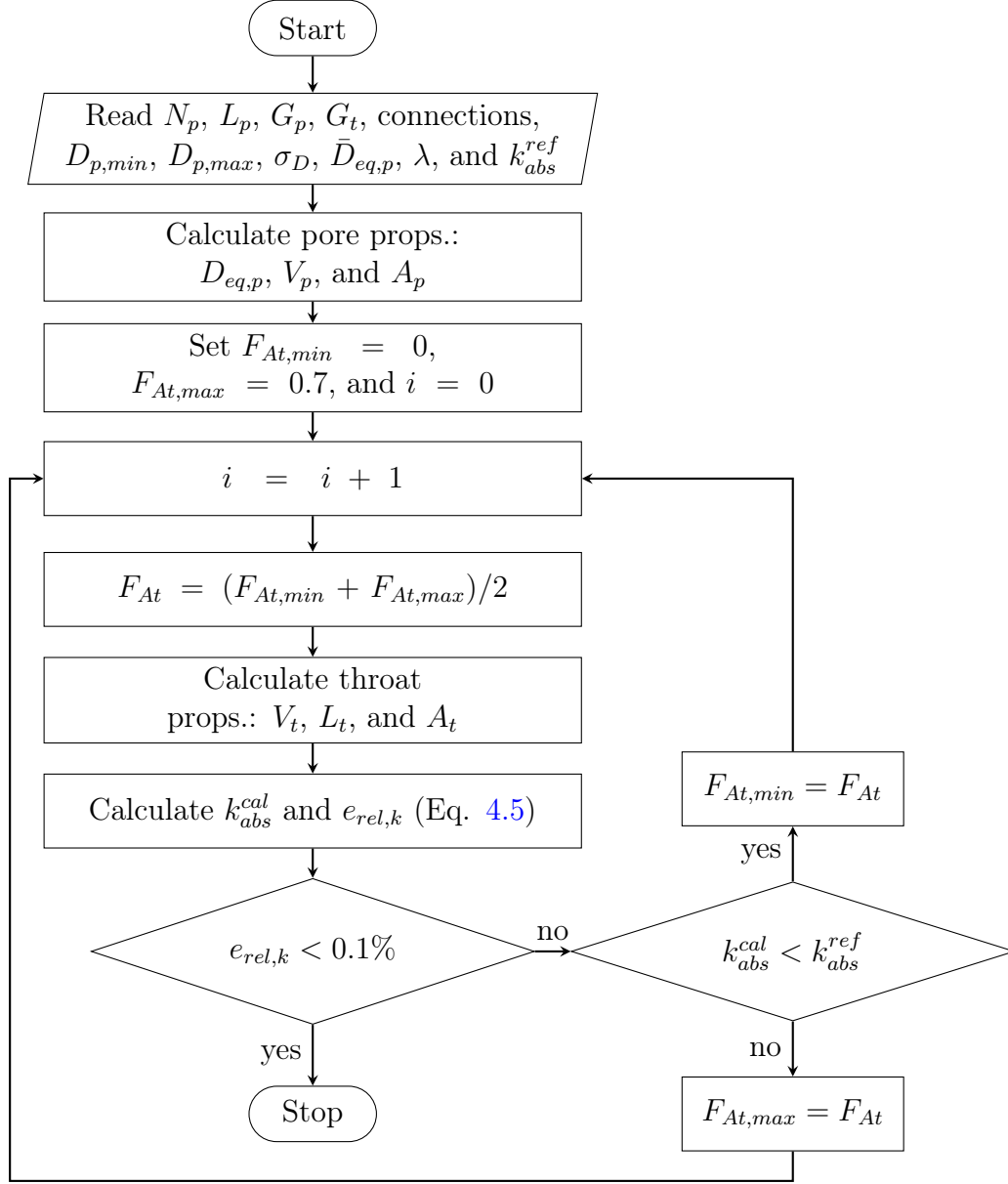


Figure 4.1: Procedure for tuning network permeability k_{abs} by binary search. All pore and throat properties are calculated according to the algorithm in Section 3.3.

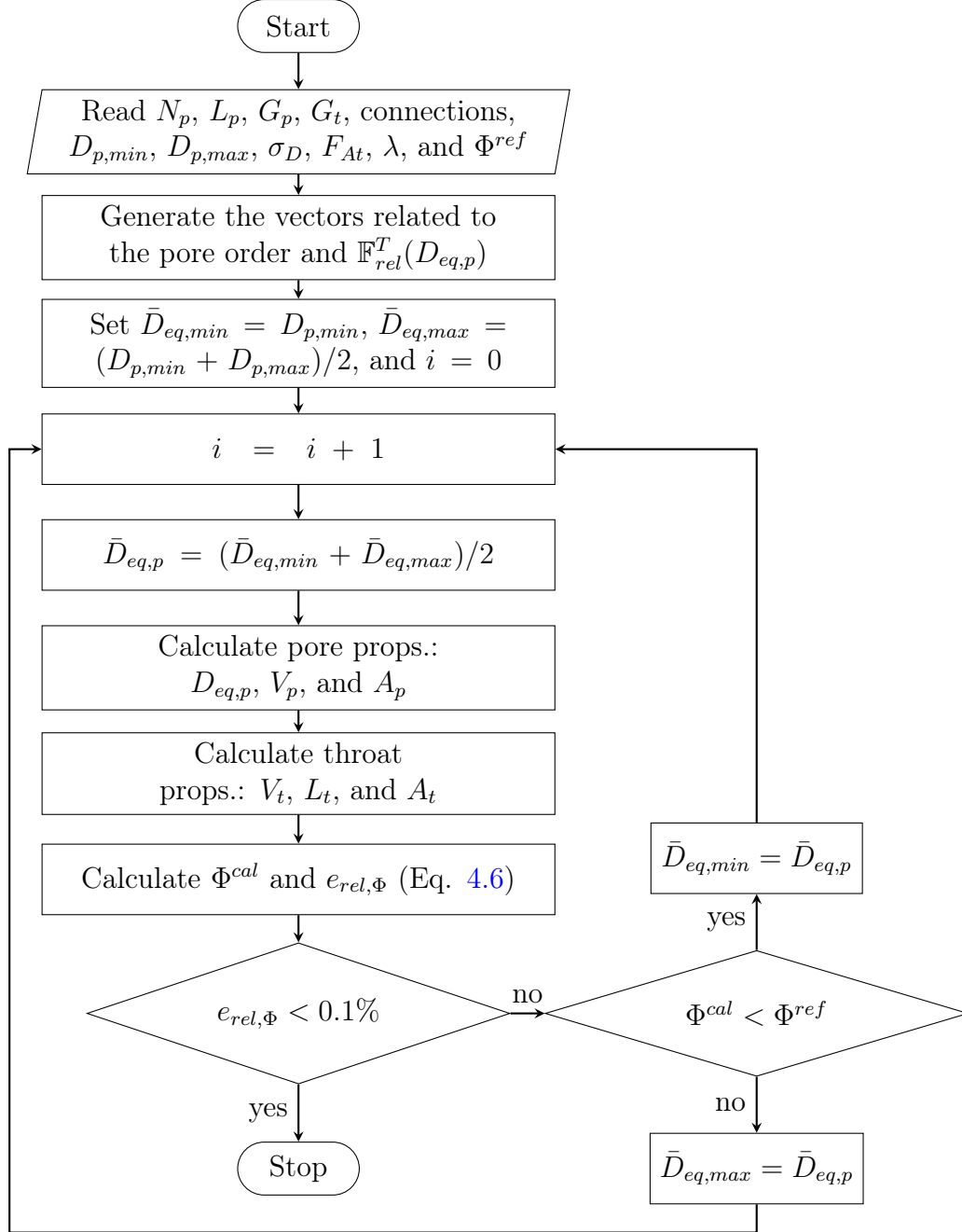


Figure 4.2: Procedure for tuning network porosity Φ by binary search. All pore and throat properties are calculated according to the algorithm in Section 3.3.

Table 4.1: Iteration history for the tuning of network CZ20T (network details on Table 5.10). The reference values are: $k_{abs}^{ref} = 1.662D$, $\phi^{ref} = 19.47 \times 10^{-2}$. The main iterations are those where we complete the cycle of tuning both parameters k_{abs} and Φ . TBSI is the total binary search iterations.

Properties	Iteration ⁽⁰⁾					
	0	1	2	3	4	5
First stage: Tuning permeability						
F_{At}	0.360	0.288	0.262	0.253	0.251	0.249
TBSI ⁽¹⁾	–	16	12	15	16	17
k_{abs}^{cal} (D)	–	1.662	1.662	1.662	1.662	1.662
Φ^{cal} ($\times 10^{-2}$)	–	18.66	19.18	19.37	19.43	19.46
Second stage: Tuning porosity						
$\bar{D}_{eq,p}$ (μm)	79.62	81.45	82.10	82.28	82.40	82.40
TBSI ⁽²⁾	10	9	10	10	9	9
k_{abs}^{cal} (D)	2.443	1.969	1.765	1.689	1.681	1.662
Φ^{cal} ($\times 10^{-2}$)	19.47	19.49	19.48	19.46	19.48	19.46

⁽⁰⁾ i from algorithm in Fig. 4.3

⁽¹⁾ Maximum i from algorithm in Fig. 4.1

⁽²⁾ Maximum i from algorithm in Fig. 4.2

- the absolute difference in $\bar{D}_{eq,p}$ before its after the adjustment is less than 0.1 μm .

To start the tuning process, we first set $F_{At}^0 = 0.36$, which corresponds to the value in the reference network, and then begin adjusting $\bar{D}_{eq,p}$. The complete algorithm is shown in Figure 4.3, and the iteration history of a tuned network is shown in Table 4.1. The process ends at iteration 5, where we obtain an adjusted value of $\bar{D}_{eq,p} = 82.40 \text{ } \mu m$ for a F_{At} value of 0.249, which satisfies the tolerance when compared to the $\bar{D}_{eq,p}$ value from iteration 4.

Notice that the algorithm requires that the number of pores, throats, and the connections between pores and throats be defined before tuning. In the scenario that the tuned network has multi-directional connectivity, it must be constructed to match the reference network in terms of the number of pores and throats as well as the network volume. This matching can be achieved by eliminating throats only, without altering the number of pores.

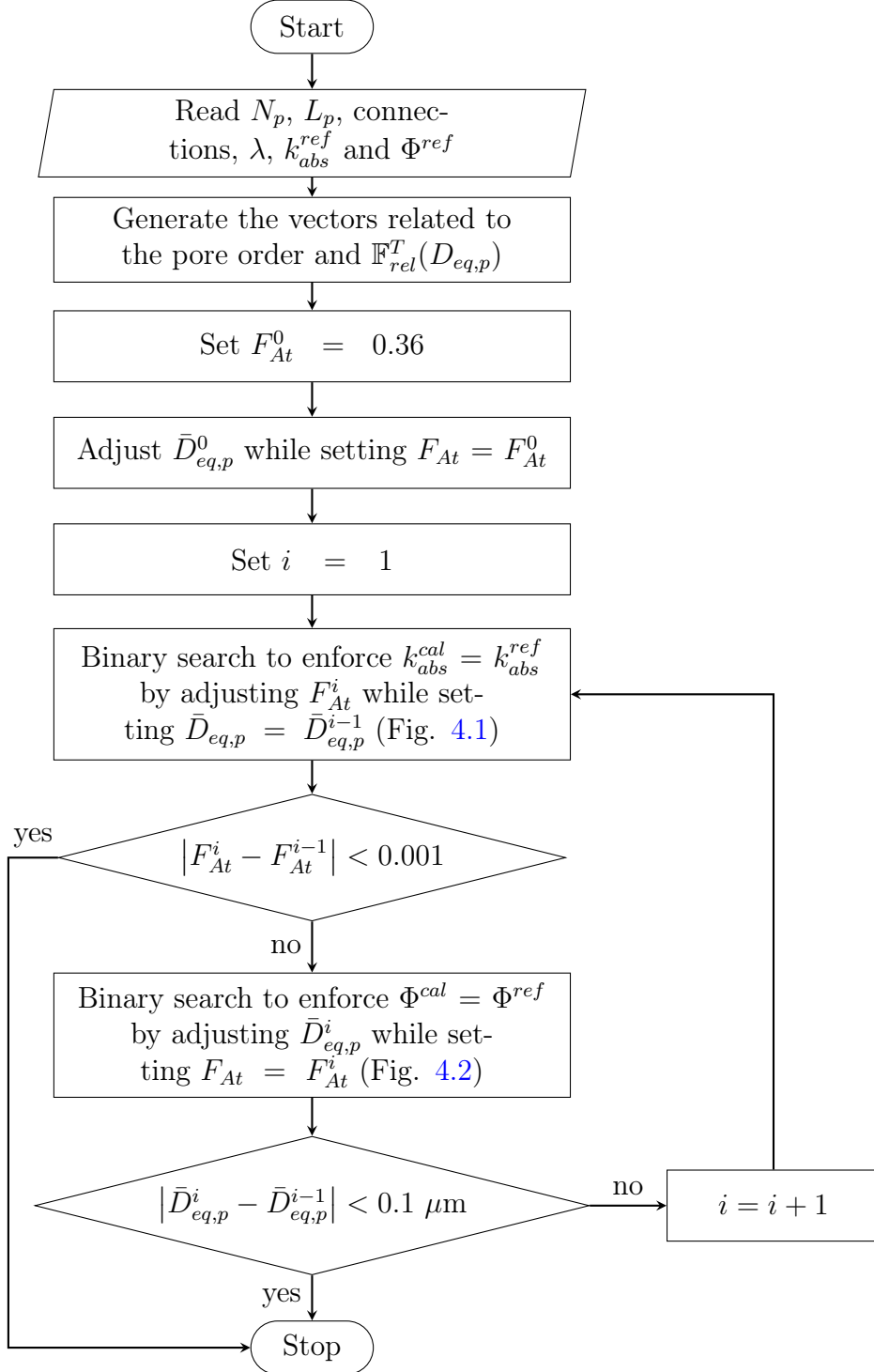


Figure 4.3: Procedure for tuning networks

Chapter 5

Results and Discussions

This chapter presents the results obtained with our two-phase flow simulator . We tested our simulator using a network that comes from an x-ray microtomographic (micro-CT) image of a Berea sample (BLUNT, 2022), and statistically generated networks. Section 5.1 describes the calculation of the parameters required to define accurate geometrical properties of the cross-sectional shape of throats extracted from the Micro-CT image. Section 5.2 presents the derivation of an expression to calculate F_g . In Section 5.3 we adjust the Berea sandstone network to match the absolute permeability values obtained from direct numerical simulations (DNS) of the same Micro-CT image. Section 5.4 presents three sensitivity analysis during the primary drainage process using the calibrated network from Section 5.3. Section 5.5 explores the results of multiple statistically generated networks under primary drainage and imbibition processes. The analysis focused on the effects of randomness in network generation, throat size distribution, coordination number, and contact angle variability.

We treated the Micro-CT image with *PoreSpy* V 2.2.2, and its properties are shown in Table 5.1. This treatment applies the method `snow` with the “high” accuracy, and the legacy option to trim saddle points to define the number of pores and throats and calculate their properties as indicated in Section 3.1.1.

All the results were obtained using *OpenPNM* V 3.2.0. The pore and throat lengths are calculated as indicated in Section 3.2.1. All boundary elements are

Table 5.1: Properties of the Berea image.

Properties	Units	Value
Image size	voxels	$400 \times 400 \times 400$
Voxel edge size (L_v)	μm	5.345
Porosity	—	0.196
Experimental ⁽¹⁾ k_{abs}	mD	650
Average ⁽¹⁾ ⁽²⁾ k_{abs}	mD	1286

⁽¹⁾ Reported by [DONG \(2007\)](#)

⁽²⁾ Calculated using a lattice-Boltzmann simulation

Table 5.2: Parameters value to improve G for throats

Triangle group	ζ_1	ζ_2
1	0.23913	0.79507
2	0.21057	0.82264

treated as indicated in Section [3.6.1](#).

Also, we mention different diameters, such as extended, inscribed, equivalent, and prism inscribed. That is because *OpenPNM* works with the “diameter” property and not with “radius”. For all types of diameters, the value of the radius is half the corresponding diameter.

5.1 Improvement of the throat cross-sectional data

First, we estimate the parameter ζ used on Equation [3.9](#), which is the correlation between the real shape factor G and the *PoreSpy* shape factor G_{ps} for different isosceles triangles that can be represented by n_v voxels, such that $A = n_v$. Results for $n_v = 20, 30, 100, 1000$ are on Figure [5.1](#).

We notice that the higher n_v is, the lower e_{95} we get. For $n_v = 30$, $e_{95} \approx 12\%$, and that is our limit value. Therefore, for $n_v \geq 30$, we estimate the parameters ζ_1 and ζ_2 of Equation [3.13](#) (throats with $n_v < 30$ are considered low resolution throats). The trend lines for each triangle group are presented in Figure [5.2](#) and the fitting results are in Table [5.2](#)

The variations of the throat shape factor due to the correction explained are in Figure [5.3](#). After the correction, all internal throats are isosceles triangles and 41.6%

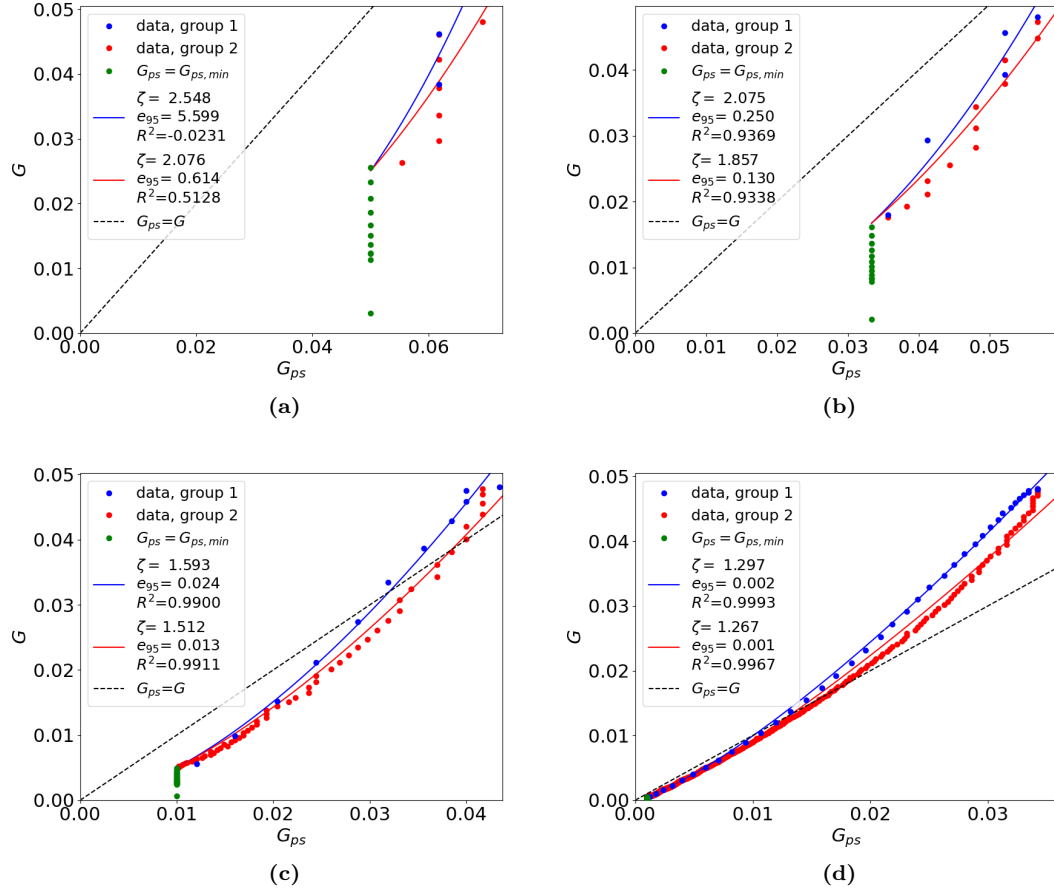


Figure 5.1: Relation between the shape factor calculated with PoreSpy and the real shape factor for different isosceles triangles that can be represented with (a) 20 voxels, (b) 30 voxels, (c) 100 voxels, and (d) 1000 voxels. The trend lines using Equation 3.12 with their 95% confidence error and R-squared are shown.

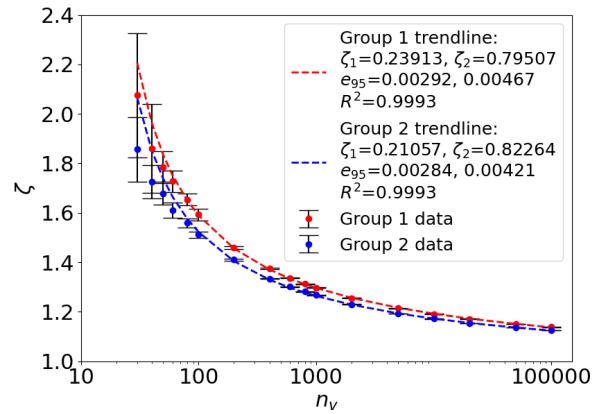


Figure 5.2: ζ data, errorbar, and trend line for each triangle group.

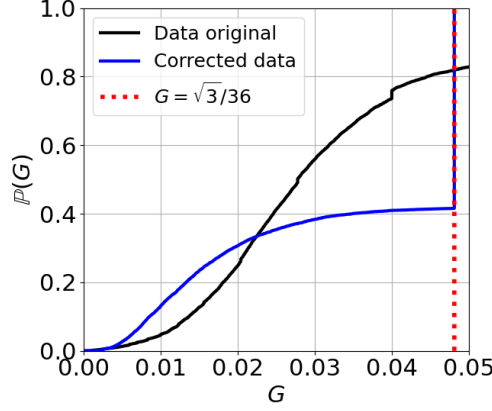


Figure 5.3: Cumulative distribution of the internal throat shape factors of the Berea network, after and before correction

of them, those with values less than $\sqrt{3}/36$, are non-equilateral triangles.

5.2 Correction factor for conductance in triangular ducts

To calculate F_g , which is our correction factor in the expression used to calculate the conductance on triangular ducts (Equation 3.68), we propose two trend lines: a sinusoidal correlation and a third-degree polynomial correlation. Figure 5.4 shows the fitting results.

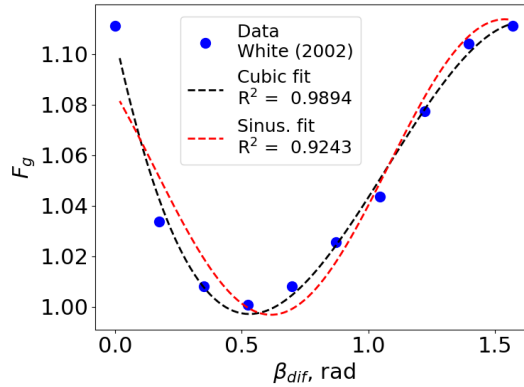


Figure 5.4: Correction factor F_g for different trend lines. The cubic function is $F_g(x) = c_0 + c_1x + c_2x^2 + c_3x^3$. The sinusoidal function is $F_g(x) = c_0 + c_1 \sin(c_2x + c_3)$. The optimization method used to calculate the coefficients is least squares.

The best trend line is the polynomial one. So the results of these functions are

shown in Table 5.3.

Table 5.3: Results for the polynomial function $F_g(x) = c_0 + c_1x + c_2x^2 + c_3x^3$ with the error at 95 % confidence interval

i	c_i	$ e_{95} $ (%)
0	1.10634	0.0131 (1.2%)
1	-0.46276	0.0741 (16.0%)
2	0.57966	0.1117 (19.3%)
3	-0.17998	0.0464 (25.8%)

And the equation to calculate F_g using β_{dif} is:

$$F_g(\beta_{dif}) = 1.10634 - 0.46276\beta_{dif} + 0.57966\beta_{dif}^2 - 0.17998\beta_{dif}^3 \quad (5.1)$$

5.3 Absolute permeability of the Berea sandstone network

To calculate K_{abs} , we use the conductance calculation provided in Section 3.6.1. Geometric property calculations are explained in Section 3.2.

5.3.1 Impact of the categories of pore diameter on the absolute permeability

The pore's inscribed, extended, and equivalent diameters were used to predict the absolute permeability of the Berea sandstone network with spherical pores and cylindrical throats. To calculate L_{min} , we used the rigorous option with $F_L = 0.05$ in Equation 3.8. The results were compared with the DNS results from MACHADO *et al.* (2024) and shown in Table 5.4.

The results obtained using the equivalent diameter of pores are the closest to the DNS values. From now on, we use the pore equivalent diameter on our PNM simulations.

Table 5.4: Absolute permeability (mD) of a Berea image using *OpenPNM* V 3.2.0 considering spherical pores and cylindrical throats using their equivalent diameters and $F_L = 0.05$ in Eq. 3.8.

Type of simulation	Type of pore diameter used	$k_{abs,x}$	$k_{abs,y}$	$k_{abs,z}$	Source
DNS	—	1627	1772	1840	MACHADO et al. (2024)
PNM	equivalent	1161	1387	1430	Present work
PNM	extended	580	700	719	Present work
PNM	inscribed	537	646	660	Present work

Table 5.5: Absolute permeability (mD) of a Berea network represented with spherical pores and cylindrical throats using *OpenPNM* V 3.2.0, considering equivalent diameter of pores and throats, and $L_{min} = L_v$.

Type of simulation	Type of pore	Cross-sectional shape for throats	$k_{abs,x}$	$k_{abs,y}$	$k_{abs,z}$	Source
DNS	—	—	1627	1772	1840	MACHADO et al. (2024)
PNM	sphere	circle	1162	1393	1432	Present work
PNM	sphere	isosceles triangle	388	437	430	Present work
PNM	prism	isosceles triangle	401	452	443	Present work

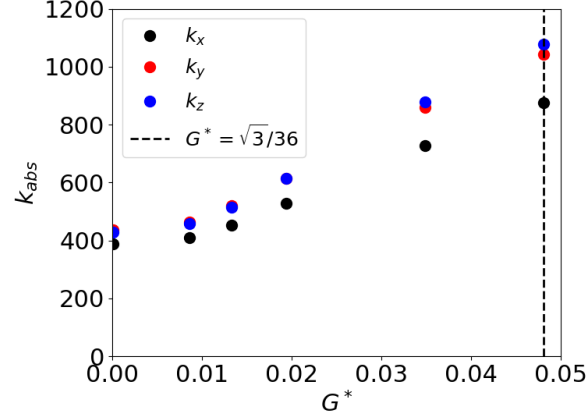
5.3.2 Impact of the calculation of the minimum length on the absolute permeability

We calculate k_{abs} using the equivalent pore diameters just as in Section 5.3.1, except that in this case we try the simpler option to calculate L_{min} given by Equation 3.7. We obtain that the absolute permeability values on the x , y , and z directions are 1162, 1393, and 1432 mD, respectively. The difference between those values and the ones in Table 5.4 is less than 0.5%. So, to reduce the computational cost, from now on, we consider the simple option to calculate L_{min} .

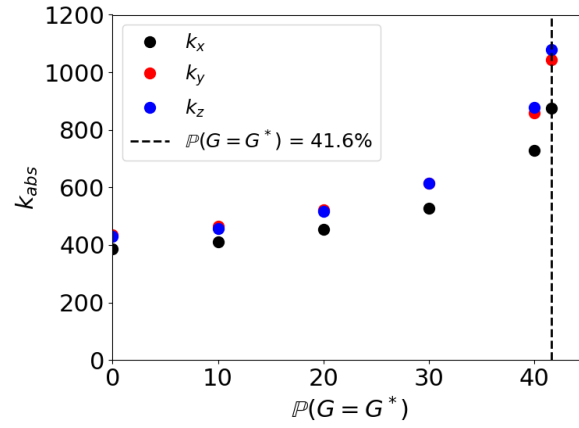
5.3.3 Impact on the absolute permeability by using triangles as cross-sectional shapes for throats and pores

We calculate k_{abs} for two different models: spherical pores and prismatic throats, and prismatic pores and throats. The equivalent diameter for pores and throats is used. The results were compared with the DNS results and shown in Table 5.5.

It was to be expected that k_{abs} would decrease after replacing cylindrical throats



(a)



(b)

Figure 5.5: Absolute permeability (mD) of the Berea sandstone network if we set $G = G^*$ for the throats with $G < G^*$. The abscissa are (a) the different values of G^* and (b) the percentual values of the cumulative distribution at G^* . *OpenPNM* V 3.2.0 was used, considering equivalent diameter of pores and throats, and $L_{min} = L_v$. We represent pores as spheres, and throats as prisms with isosceles triangles as cross sections.

by prismatic throats, given the conductance for both representations. To evaluate the effect of the throat shape factor distribution, we performed new simulations modifying the shape factor of the throats with $G < G^*$ to $G = G^*$, being G^* the value of G at which the cumulative shape factor distribution has a given value. After altering G , the half angles β_i are modified without modifying the triangle group. The percentual values of the cumulative G distribution used were 10%, 20%, 30%, 40%, and 41.6%; the last one being the fraction of non-equilateral triangles. Results are on Figure 5.5.

In Figure 5.5, the rightmost values for k_{abs} on the axes x , y , and z are 875, 1043, and 1078 mD respectively, and represent equilateral triangular cross-sections for the

throats. They are approximately 60% of the DNS values. This implies that it is impossible to reach the values of absolute permeability obtained by DNS with the actual network geometry properties.

Before calibrating the absolute permeability, we obtain the distributions of the ratio of the throat diameter to the minimum connected pore diameter in terms of the throat conductance and throat cross-sectional area. Figure 5.6 shows these distributions, which show that the throats with an equilateral triangle cross section are those with the smallest areas and thus, with low resolution of the CT image. They have the lowest conductances and most of them have small aspect ratios in relation to their neighboring pores. Therefore, assuming these throats have an intrinsic error due to low resolution, we apply the calibration method in Section 3.7, considering only the low-resolution throats.

We obtain that the best value for F_{R2} , used in Equation 3.87, is 0.38126, obtaining values of k_{abs} of 1636 ($e_{rel} = 0.553\%$), 1771 ($e_{rel} = -0.056\%$), and 1831 ($e_{rel} = -0.489\%$) in the x , y , and z directions, respectively. For this case, Equation 3.87 becomes:

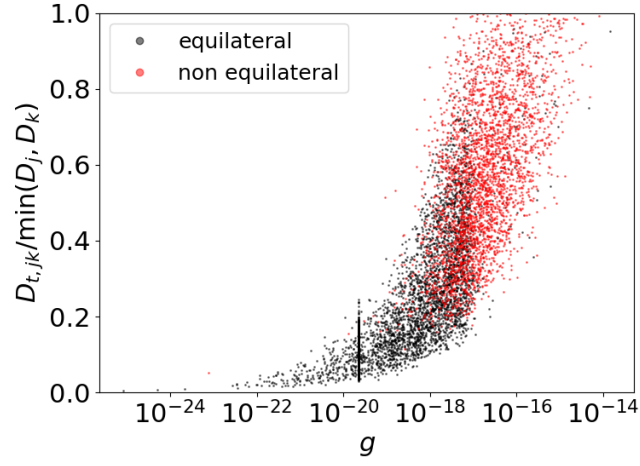
$$R_{t,new} = 0.61874R_{t,old} + 0.266882\min(R_j, R_k) \quad (5.2)$$

5.4 Relative permeability of the Berea network

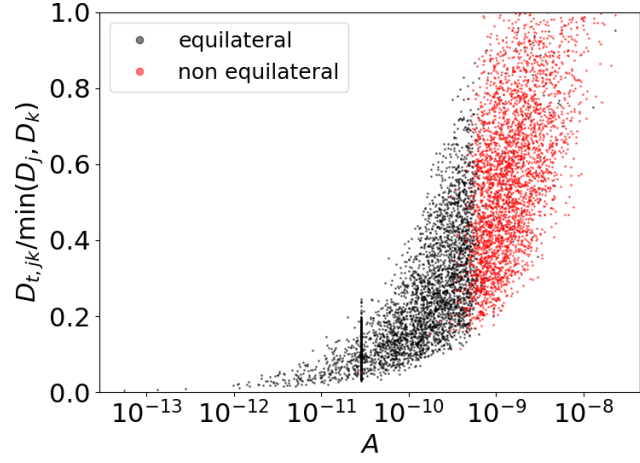
The simulations were carried out using the network model obtained with the following settings to get the best values of k_{abs} :

- equivalent radius of pores and throats;
- simple option to calculate L_{min} ;
- correction of equivalent radius for low resolution throats, according to Equation 5.2

We simulate oil and water flooding. Table 5.6 shows the employed phase properties, which were obtained from VALVATNE and BLUNT (2004).



(a)



(b)

Figure 5.6: Distribution plots of the ratio of the throat equivalent diameter to the minimum connected pore equivalent diameter; compared to (a) the throat conductance ($\mu = 0.001$ Pa.s), and (b) the throat cross-sectional area; for the Berea network. All throats are represented as prisms with an isosceles triangle as the cross-sectional shape.

Table 5.6: Phase properties used to simulate two-phase invasion

Property	Unit	Value
Water viscosity	mPa/s	1.05
Oil viscosity	mPa/s	1.39
Interfacial tension	N/m	30

A sensitivity analysis of the following properties were carried out:

- receding contact angle, θ_r ;
- throat volume used to calculate saturation;
- pore shape factor.

We tested four values for θ_r : 0° , 20° , 40° , and 60° , whose results for the drainage are in Figure 5.7.

The existence of throat volumes was evaluated because *PoreSpy* considers a 2D representation for throats, and, therefore, they have zero volume. We assign a volume for each throat using the cross-sectional area and length properties used in the conductance calculation. Half the throat volume is diminished from the volume of each one of the neighboring pores. Reallocation of a portion of the pore volume to a neighboring throat is not performed for those pores that would end up with a negative volume. Figure 5.8 compares the results for two representations of the Berea sandstone network: one considering null throat volumes and another assigning a volume to each throat. We observe that assigning throat volumes shifts the k_{rel} and p_c curves to the right. This occurs because, when a pore is invaded by oil, the volume effectively occupied by the oil is reduced in the scenario where a portion of the pore volume has been reallocated to its connected throats.

The throat shape factor was evaluated due to the assumed hypothesis of equilateral cross section for pores. For the test, we considered that the shape factor of each pore is equivalent to the average shape factor of its neighboring throats. Figure 5.9 compares the results for the original Berea sandstone network (with equilateral pores) and a modified version where pores are isosceles, following the described process. The only observed difference is in the $k_{rel,w}$ results, which increase for the isosceles case at a given X_w . This can be explained by the presence of corner angles larger than $\pi/3$ ($\beta_i > \pi/6$), which enhance water flow despite the simultaneous restriction imposed by the more acute angles. Since water primarily flows through the

corners, the net effect of isosceles triangles as pore cross sections favors an increase in $k_{rel,w}$.

5.5 Evaluation of the simulator using statistically built networks

First, we examined the properties of the pore-space elements of the Berea sandstone sample after applying the correction described in Section 5.3 that defined the parameter values of the network (Section 3.3). The distribution of the pore equivalent diameter is well approximated by a truncated lognormal distribution with $D_{p,min} = 24.59 \mu\text{m}$, $D_{p,max} = 266.69 \mu\text{m}$, $\bar{D}_{eq,p} = 80.32$, and $\sigma_{Dp} = 38.00 \mu\text{m}$, as shown in Figure 5.10. We use this information to define the pore diameters using the method explained in Appendix C.1 to statistically build PNMs as indicated in Section 3.3.

The values of λ and F_{At} in Equations were determined for a cubic-lattice network with uniform coordination number of 6 and similar porosity, Φ , and permeability, k_{abs} , of the Berea sandstone network. The Berea network has 3965 pores, $k_{abs} = 1746$ mD, and $\Phi = 0.196$. To work with a similar number of pores, we use a $16 \times 16 \times 16$ network. For F_{At} we first consider three possible values: 0.14, which is the mean value for the low-resolution throats (those represented by less than 30 voxels), which are 57.3% of the total; 0.36, which is the mean value for the other group of throats, which are 42.7% of the total; and 0.25, which is the average of the two values. The λ values that satisfy the condition $\lambda > D_{p,max}$ avoid pore overlapping. Still, if $\lambda \leq D_{p,max}$, we can work with values higher than $145.64 \mu\text{m}$ if we reorganize the pores' location in the network to avoid pore overlapping (explained in Appendix C.2). However, it was observed that when using the highest value of F_{At} , it was necessary to use $\lambda = 146 \mu\text{m}$ to achieve permeability and porosity values close to those of Berea. For this reason, we have decided to use $F_{At} = 0.36$ and $\lambda = 146 \mu\text{m}$ for our constructed networks.

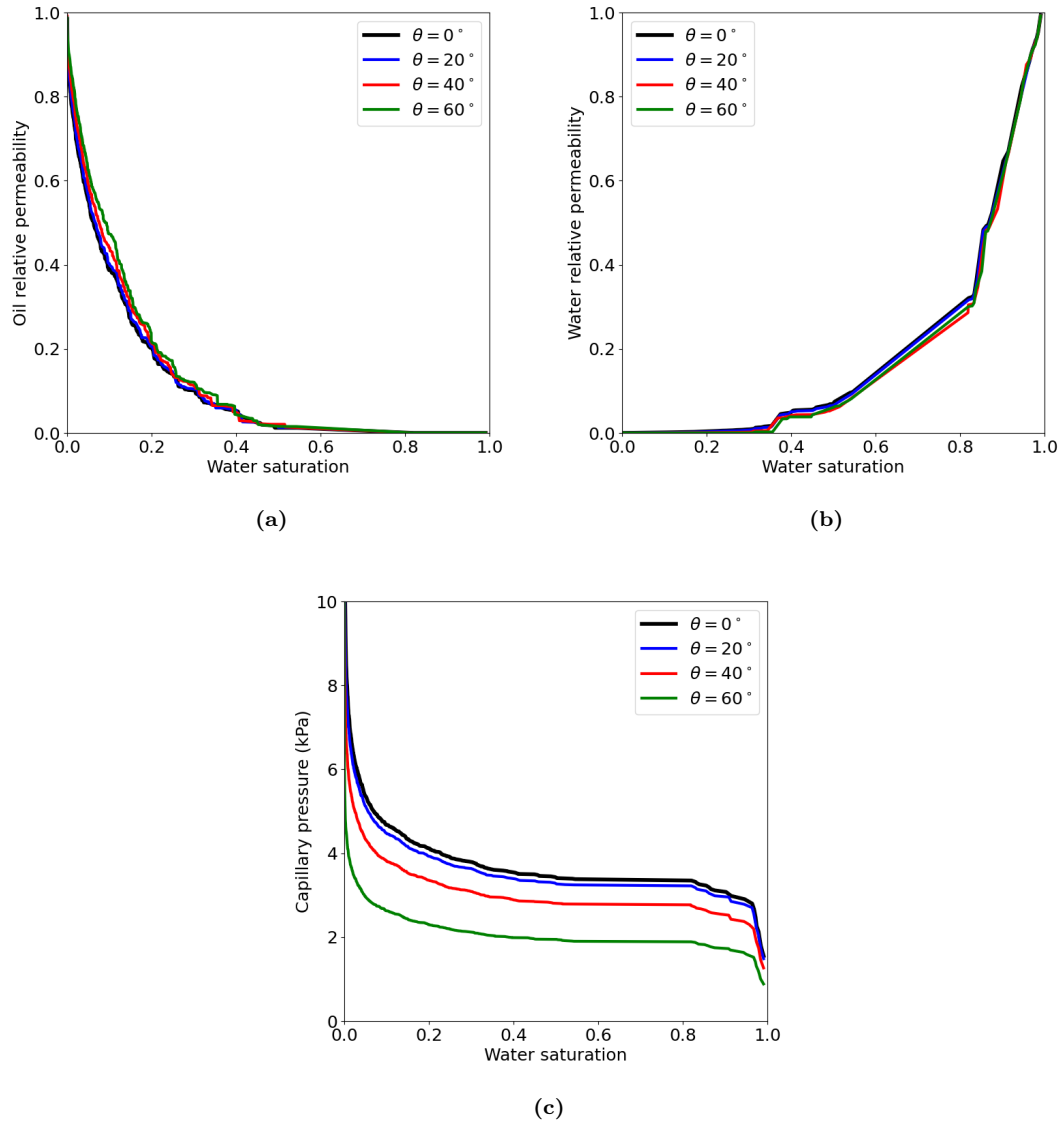
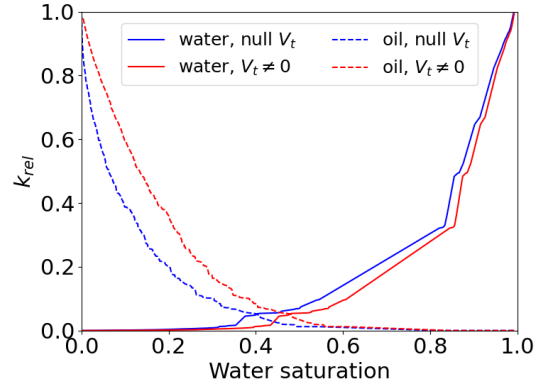
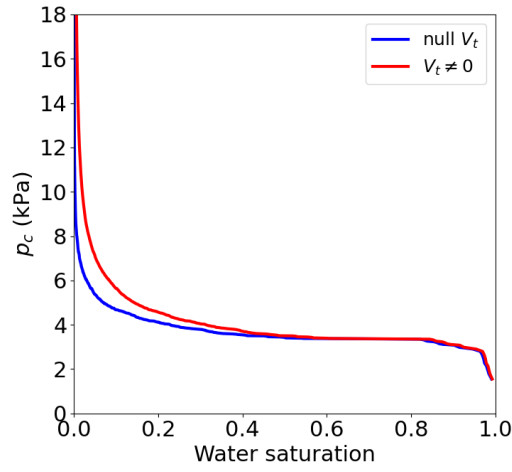


Figure 5.7: Sensitivity analysis of the contact angle on the primary drainage simulation, for a Berea network represented by prismatic pores and throats. We show the results of (a) oil relative permeability, (b) water relative permeability and (c) capillary pressure according to the water saturation

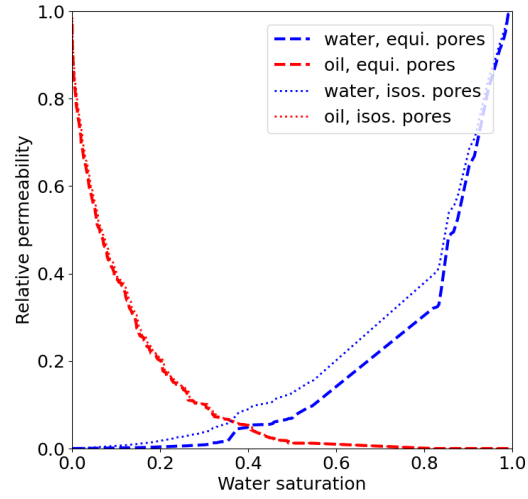


(a)

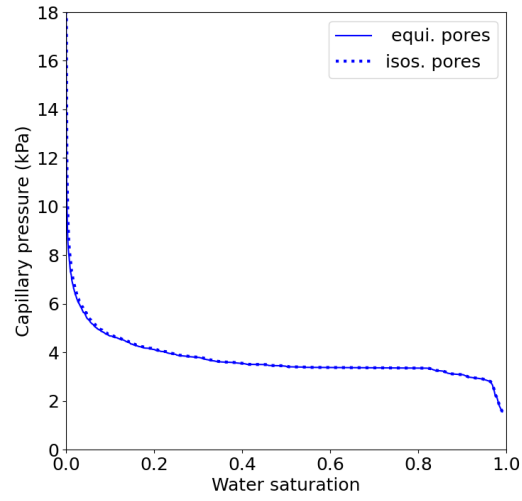


(b)

Figure 5.8: Sensitivity analysis of the throat volume on the primary drainage simulation, for a Berea network represented by prismatic pores and throats. We show the results of (a) oil and water relative permeability, and (b) capillary pressure according to the water saturation



(a)



(b)

Figure 5.9: Sensitivity analysis of the throat shape factor on the primary drainage simulation, for a Berea network represented by prismatic pores and throats. We show the results of (a) oil and water relative permeability, and (b) capillary pressure according to the water saturation

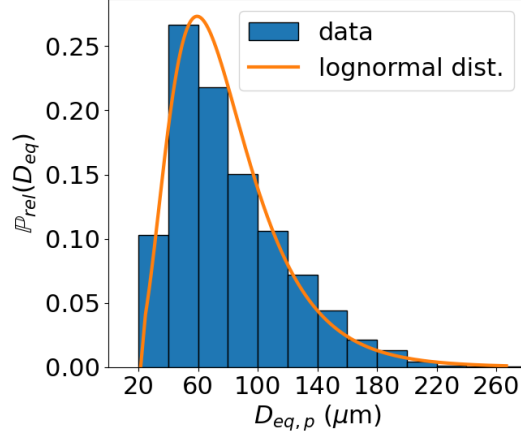


Figure 5.10: Histogram of the pore equivalent diameter data from the Berea sample and a lognormal distribution curve with the same mean and standard deviation as the Berea data

Following the specification of network parameters, we chose contact angles as referential phase properties to establish evaluation reference cases. We take the dynamic contact angle values on an oil-brine system found by [YANG *et al.* \(1999\)](#). We considered two sets of contact angles: $\theta_r = \theta_a = 0^\circ$ and $\theta_r = 60^\circ$, $\theta_a = 110^\circ$, that correspond to the angles for a decane-brine system without and with aging, respectively. The aging process was with crude oil for 14 days at 80°C .

In this section, we present the simulation results for constructed networks with constant Z and networks with multi-directional connectivity. We refer to the first as C-type networks and the second as CZ-type networks. We established a naming convention for these networks: first, we use C or CZ, depending on the type of connectivity. Then, we indicate a number X , which corresponds to the number of pores along each face of the cubic lattice. Finally, we include either the value of F_{At} or the letter T if the network has been tuned.

For example, C10F36 refers to a $10 \times 10 \times 10$ cubic-lattice network with constant connectivity and a target area fraction $F_{At} = 0.36$. The name C10T refers to a tuned network with the same lattice size, whose reference network is indicated in the text or in a table.

Table 5.7: Properties of $10 \times 10 \times 10$ networks with similar Φ , k_{abs} . For those networks: $\lambda = 146 \mu\text{m}$, $N_p = 1000$, $N_t = 2700$, the $D_{eq,p}$ distribution corresponds to a lognormal distribution with an interval of $[24.59\mu\text{m}, 266.69\mu\text{m}]$ and $\sigma_D = 38.00 \mu\text{m}$.

Properties	Description	
Name	C10F36	CZ10T
Connectivity mode	Constant	Multi-directional
F_{At}	0.360	0.201
$\bar{D}_{eq,p} (\mu\text{m})$	80.32	83.34
$\Phi (\times 10^{-2})$	17.51	17.52
$k_{abs} (\text{D})$	1.337	1.337

Table 5.8: Simulation details for $10 \times 10 \times 10$ networks

Properties	Sim. 1	Sim. 2	Sim. 3	Sim. 4
Network	C10F36	C10F36	CZ10T	CZ10T
θ_r	0°	60°	0°	60°
θ_a	0°	110°	0°	110°
max Δp (kPa)	96.0	50.4	123.9	62.6

5.5.1 Preliminary Test

We check the imbibition simulator using two $10 \times 10 \times 10$ cubic-lattice networks: one with a simple cubic lattice with constant $Z = 6$, $F_{At} = 0.36$ and $\bar{D}_{eq,p} = 80.32 \mu\text{m}$, and other which is a tuned multidirectional network with shares the same number of pores, throats, porosity and permeability than the first one. The procedure to construct and tune the second network is explained in Section 4.3. Their properties are shown in Table 5.7. Table 5.8 indicates the network used, the maximum Δp reached in the primary drainage process, and the values for θ_r and θ_a for each simulation. Figures 5.11 and 5.12 present for each simulation: the relative permeability, the capillary pressure (difference between oil pressure and brine pressure), and the cumulative number of displacements as a function of water saturation, considering piston-like displacement (PLD), pore-body filling (PB), and snapoff (SO,p, for pores and SO,t, for throats). The type of displacement that did not occur throughout the simulation process is not plotted.

Comparing simulations for different networks, we notice that simulations with the same values for θ_r and θ_a give similar results. In fact, the simulations that use $\theta_r = \theta_a = 0^\circ$ (which represents a scenario where water is a strongly wetting phase) show that imbibition stops at a lower water saturation with a final $k_{rel,w}$ of

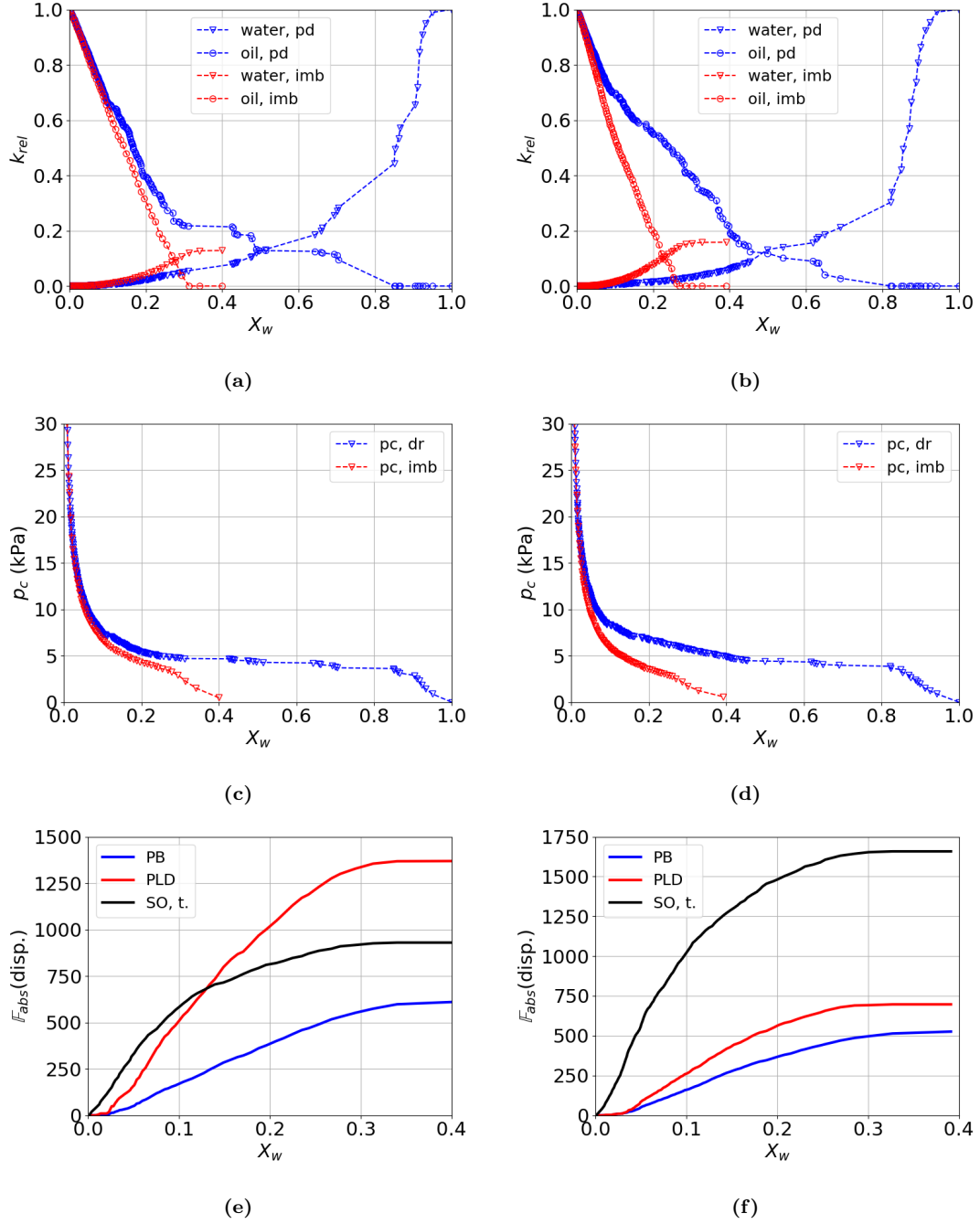


Figure 5.11: Flow simulation results for the C10F36 (a, c, e) and CZ10T (b, d, f) networks, considering $\theta_r = \theta_a = 0^\circ$. (a,b) relative permeability, (c,d) capillary pressure, and (e,f) cumulative number of displacements are shown. The quasi-static states are sampled at different intervals: for drainage is at every 10 states, for imbibition is at every 20 states.

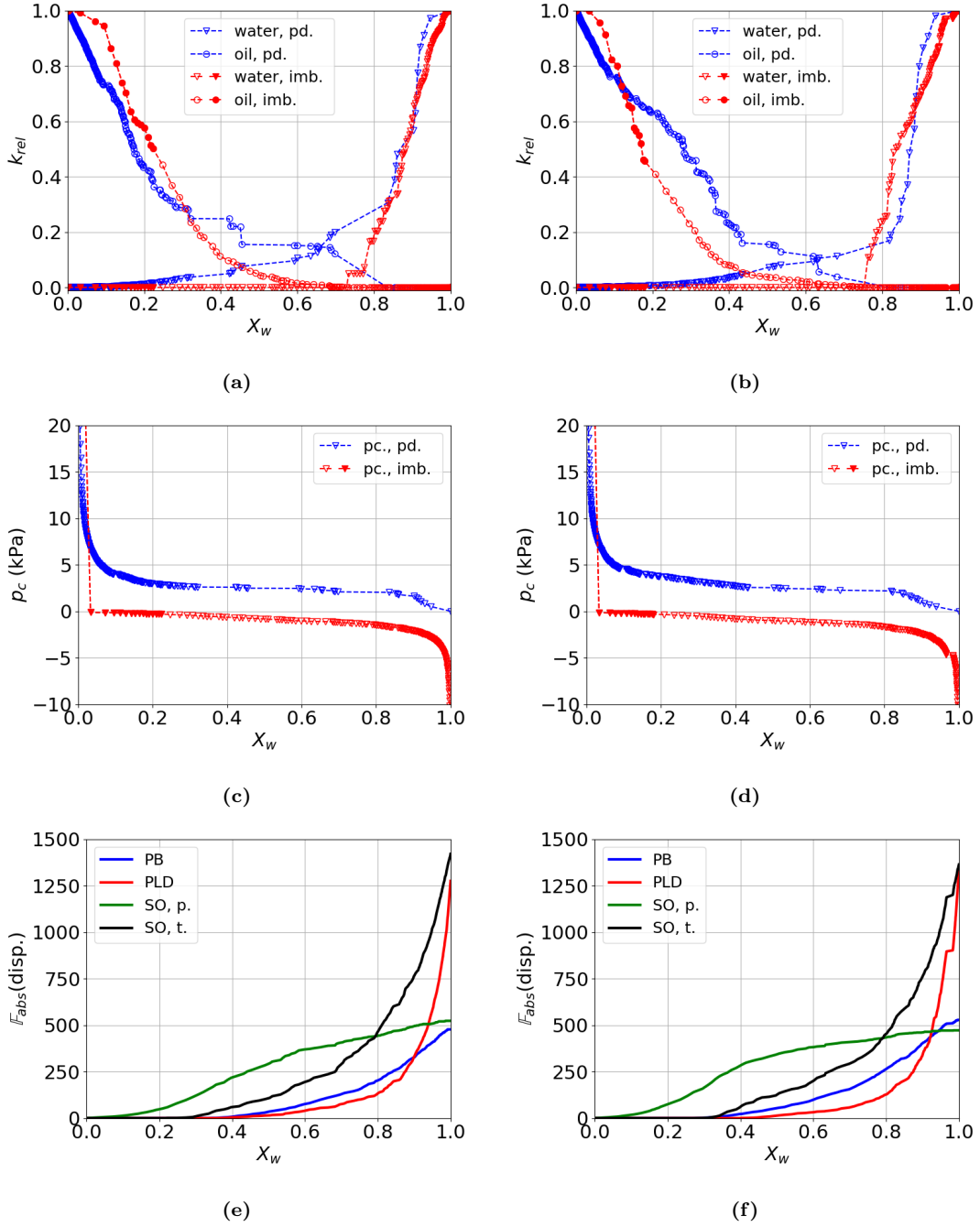


Figure 5.12: Flow simulation results for the C10F36 (a, c, e) and CZ10T (b, d, f) networks, considering $\theta_r = 60^\circ$, $\theta_a = 110^\circ$. (a,b) relative permeability, (c,d) capillary pressure, and (e,f) cumulative number of displacements are shown. The quasi-static states are sampled at different intervals: for drainage is at every 10 states, for imbibition, they are sampled first at every 4 states (filled markers) and at every 20 states afterward (unfilled markers).

approximately $X_w = 0.4$ (Figures 5.11a and 5.11b) and a positive p_c (Figures 5.11c and 5.11d). During these imbibition simulations, the displacements caused by the MTM were preferred on pores for both networks and on throats for the network with constant Z (Figures 5.11e and 5.11f), which is probably due to the strong adhesion of water to the walls. Snapoff did not occur in both cases. The preference of snapoff over PLD in the throats on the CZ10T network can be explained by either the loss of connectivity in pores with lower Z or the lower F_{At} of the CZ10T compared to the C10F36. Snapoff events cause loss of connectivity between the oil clusters and the outlet pores. The higher frequency of this displacement explains why imbibition ends at a low water saturation.

On the other hand, the simulations that use $\theta_r = 60^\circ$ and $\theta_a = 110^\circ$ ends after invading almost all the network with oil (Figures 5.12a and 5.12b) with a negative p_c (Figures 5.12c and 5.12d). Snapoff is the preferred displacement throughout the process (Figures 5.12e and 5.12f). However, connectivity is never lost because of the formation of sandwiched oil layers, possible only because oil becomes the wetting phase in imbibition ($\theta_a > 90^\circ$). For both networks, the water relative permeability has lower values ($k_{rel,w} < 2 \times 10^{-5}$) at the start of imbibition explained because at the start the water only flows at the corners, but suddenly becomes higher than 0.05 at $X_w \approx 0.75$, which can be explained if the first path of invaded elements between the inlet and outlet is formed at this saturation value. The negative pressure is caused due to the change of wettability.

5.5.2 Proposed case studies

First, we conducted a statistical analysis using 10 network realizations, as our network construction method randomly determines three properties: pore equivalent diameter, pore length, and throat shape factor. All networks were sequentially built using a single series of random numbers for all these three properties. Both $10 \times 10 \times 10$ and $20 \times 20 \times 20$ were analyzed. We used cubic-lattice networks: one with constant Z and the other with multi-directional connectivity constructed using

Table 5.9: Base properties of the network groups used for statistical analysis

Properties	Group 1	Group 2	Group 3	Group 4
Code	C10F36	CZ10F36	C20F36	CZ20F36
Size	$10 \times 10 \times 10$	$10 \times 10 \times 10$	$20 \times 20 \times 20$	$20 \times 20 \times 20$
Connectivity mode	Constant	Multi-directional	Constant	Multi-directional
N_p	1000	700	8000	5600
N_t	2700	2100	22800	16800
Z	5.4	6	5.7	6

Table 5.10: Properties of $20 \times 20 \times 20$ networks with $\lambda = 146\mu\text{m}$, $N_p = 8000$, $N_t = 22800$, and lognormal distribution with interval $[24.59\mu\text{m}; 266.69\mu\text{m}]$ and standard deviation $\sigma_D = 38.00\mu\text{m}$.

Properties	Description			
Name	C20F36	CZ20T	C20F31	C20F41
Connectivity mode	Constant	Multi-directional	Constant	Constant
F_{At}	0.360	0.249	0.310	0.410
$\bar{D}_{eq,p}$ (μm)	80.32	82.40	80.32	80.32
Φ ($\times 10^{-2}$)	19.47	19.46	18.92	20.03
k_{abs} (D)	1.662	1.662	1.284	2.063

pore and throat elimination ([MACHADO et al., 2023](#)). All networks were created as indicated in Section 3.3. The number of pores and throats for each network type and size is indicated in Table 5.9. The simulations are done using the same two pairs of contact angles used on the validation test.

Then, to analyze the simulations' dependence on properties like the throat size or the contact angles, and the results for networks with similar porosity and absolute permeability, $20 \times 20 \times 20$ networks were used. The built networks are listed in Table 5.10. All networks were created as indicated in Section 3.3 and tuning as indicated in Section 4.3. C20F36 and CZ20T have similar porosity and permeability. C20F31 and C20F41 were built under the same conditions as C20F36, except for F_{At} , to analyze the sensitivity of the results regarding the mean throat area.

The proposed analysis is:

1. Repeat the comparison done with $10 \times 10 \times 10$ networks using $20 \times 20 \times 20$ networks.
2. Observe the dependence of the primary drainage and imbibition results on the throat cross-sectional area (networks C20F31, C20F36, and C20F41), using

Table 5.11: Simulation details to test θ_a . The same network C20F36 is used in all cases.

Properties	Sim. 1	Sim. 2	Sim. 3
θ_r	0°	30°	60°
θ_a	60°	60°	60°

Table 5.12: Simulation details to test θ_a . The same network C20F36 is used in all cases.

Properties	Sim. 1	Sim. 2	Sim. 3	Sim. 4	Sim. 5
θ_r	0°	0°	60°	60°	60°
θ_a	0°	60°	60°	80°	110°

the same phase conditions ($\theta_r = 60^\circ$, $\theta_a = 110^\circ$).

3. Observe the dependence of the drainage and imbibition results on the values of θ_r , considering values shown in Table 5.11.
4. Observe the dependence of the imbibition results on the values of θ_a , considering values shown in Table 5.12.

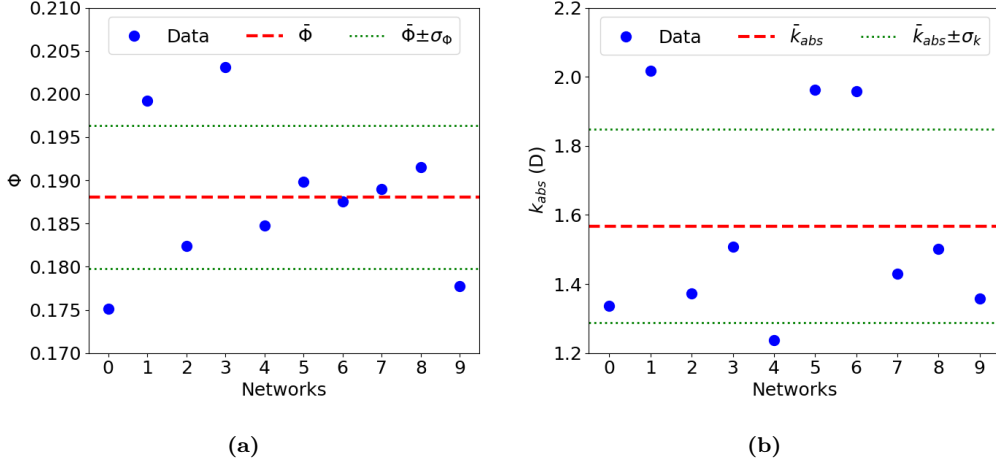


Figure 5.13: Statistical analysis of properties for C10F36 networks. a) porosity, with $\bar{\Phi} = 0.188$ and $\sigma_{\Phi} = 0.008$. b) absolute permeability, with $\bar{k}_{abs} = 1.57$ D and $\sigma_k = 0.28$ D.

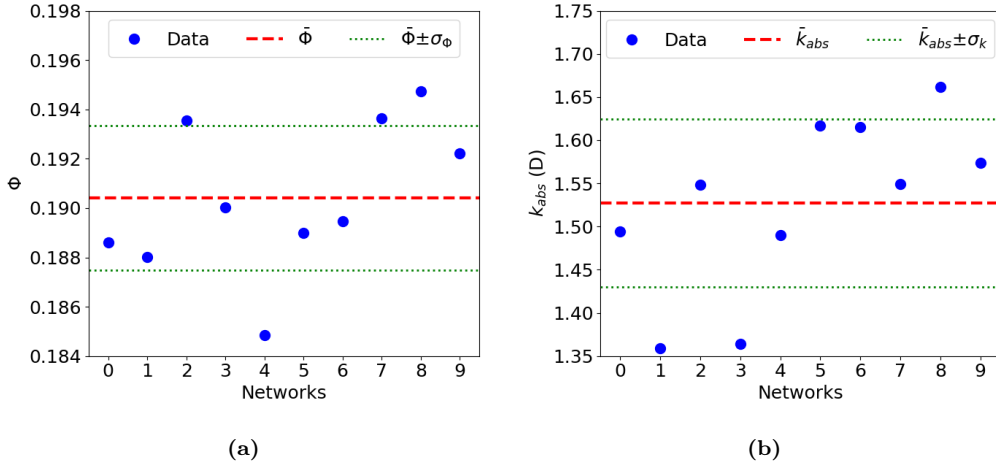


Figure 5.14: Statistical analysis of properties for C20F36 networks. a) porosity, with $\bar{\Phi} = 0.190$ and $\sigma_{\Phi} = 0.003$. b) absolute permeability, with $\bar{k}_{abs} = 1.53$ D and $\sigma_k = 0.10$ D.

5.5.3 Statistical analysis of PNM properties

Constant connectivity networks

For networks with constant connectivity, their properties are presented on Figures 5.13 and 5.14 show the properties of CXF36 networks ($X = 10, 20$). The values of \bar{k}_{abs} and $\bar{\Phi}$ for the two network sizes agree within their standard deviation ranges. As expected, the standard deviations are smaller for the larger networks. Also, for both network sizes, the ratios between the standard deviation and the mean for k_{abs} are the largest, being almost 16% for the smaller network and 6.5% for the larger network.

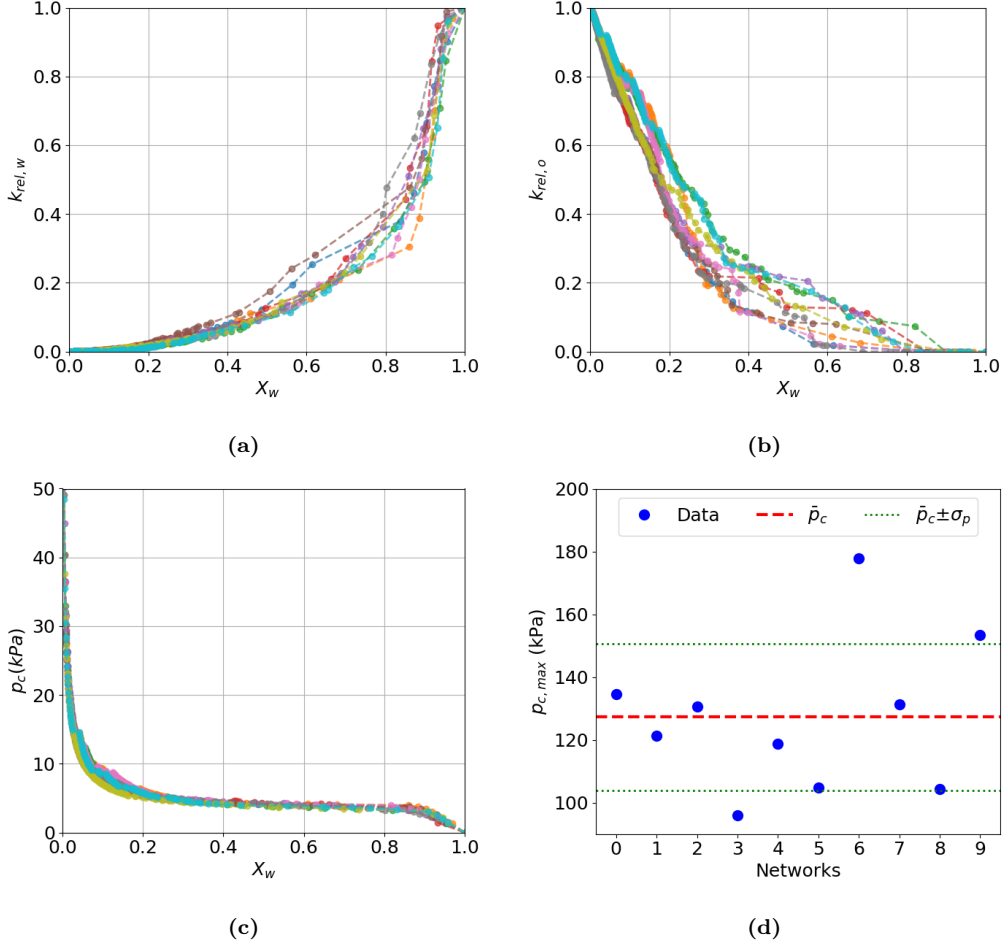


Figure 5.15: Statistical analysis of the drainage simulation results for C10F36 networks, considering $\theta_r = \theta_a = 0^\circ$. a) water relative permeability, b) oil relative permeability, and c) capillary pressure are sampled at every 10 states. d) maximum capillary pressure, with $\bar{p}_c = 127.3$ kPa and $\sigma_p = 23.3$ kPa.

The simulation results considering $\theta_r = \theta_a = 0^\circ$ are shown in Figures 5.15 and 5.16 for the smaller networks, and in Figures 5.17 and 5.18 for the larger networks. For the $10 \times 10 \times 10$ networks, despite variability in $p_{c,max}$ (Figure 5.15d), and in X_w and $k_{rel,w}$ after imbibition (Figures 5.16d and 5.16e), the relationships between k_{rel} and X_w and between p_c and X_w exhibit similar trends for all network realizations, with notable dispersion for the relative permeabilities. (Figures 5.15a, 5.15b, 5.16a and 5.16b). In contrast, the relative permeability dispersion is significantly reduced for the realizations of the $20 \times 20 \times 20$ networks, whose final mean water saturation exhibits a standard deviation of less than 2% of its value (Figure 5.18d).

The simulation results considering $\theta_r = 60^\circ$, $\theta_a = 110^\circ$ are shown in Figures 5.19 and 5.20 for the smaller networks, and in Figures 5.21 and 5.22 for the larger

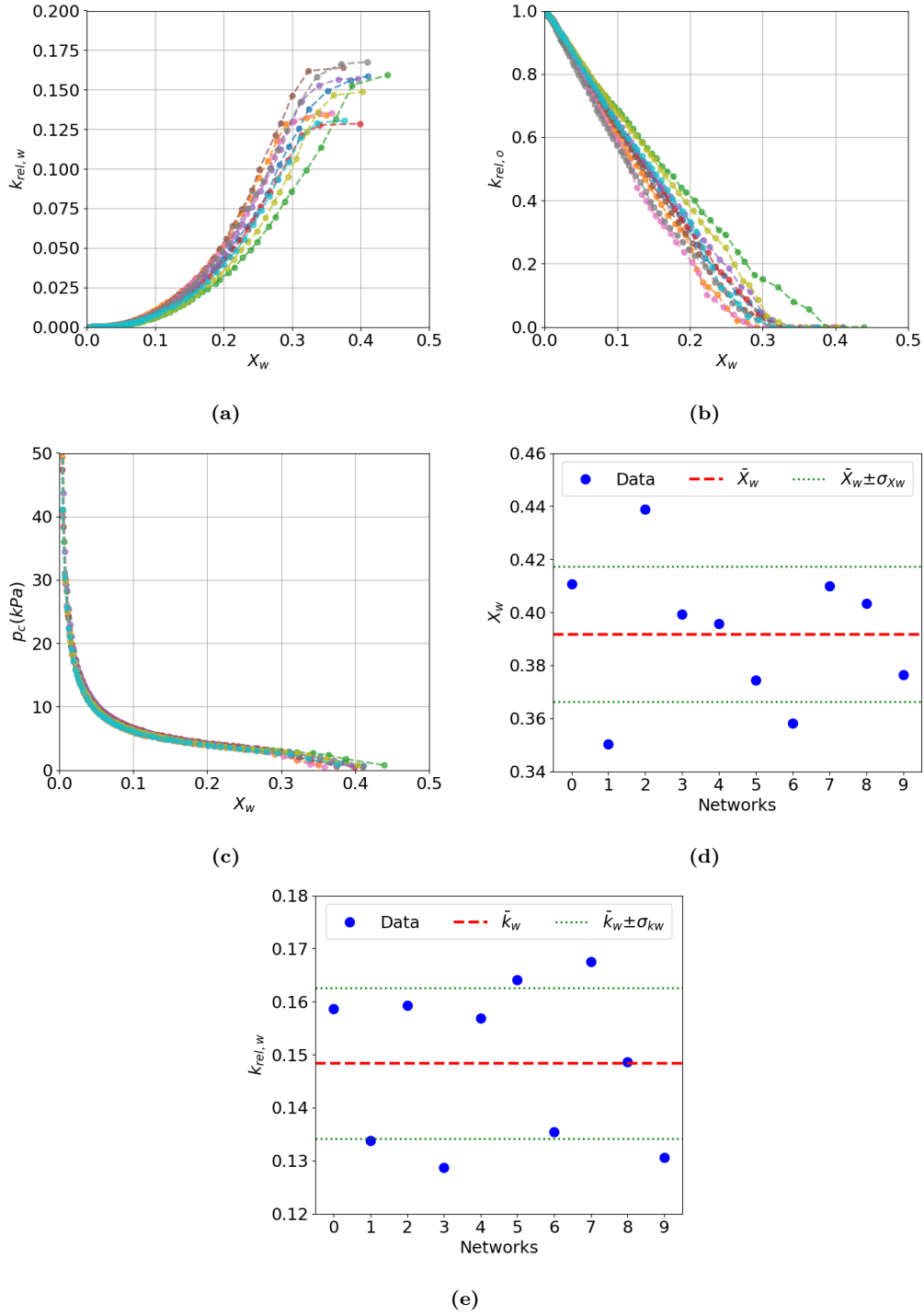


Figure 5.16: Statistical analysis of the imbibition simulation results for C10F36 networks, considering $\theta_r = \theta_a = 0^\circ$. a) water relative permeability, b) oil relative permeability, and c) capillary pressure are sampled at every 20 states. d) final water saturation, with $\bar{X}_w = 0.392$ and $\sigma_{X_w} = 0.025$ kPa. e) final water relative permeability, with $\bar{k}_w = 0.148$ and $\sigma_{k_w} = 0.014$.

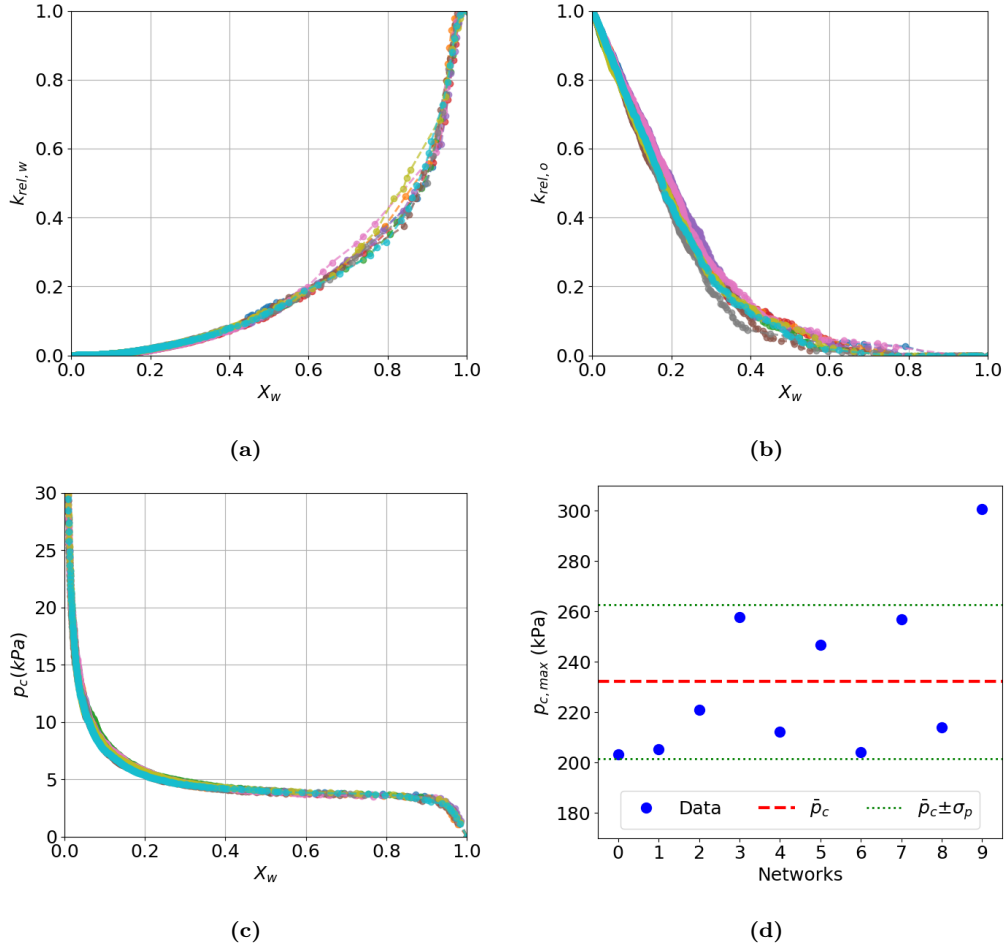


Figure 5.17: Statistical analysis of the drainage simulation results for the C20F36 networks, considering $\theta_r = \theta_a = 0^\circ$. a) water relative permeability, b) oil relative permeability, and c) capillary pressure are sampled at every 50 states. d) maximum capillary pressure, with $\bar{p}_c = 232.2$ kPa and $\sigma_p = 30.6$ kPa.

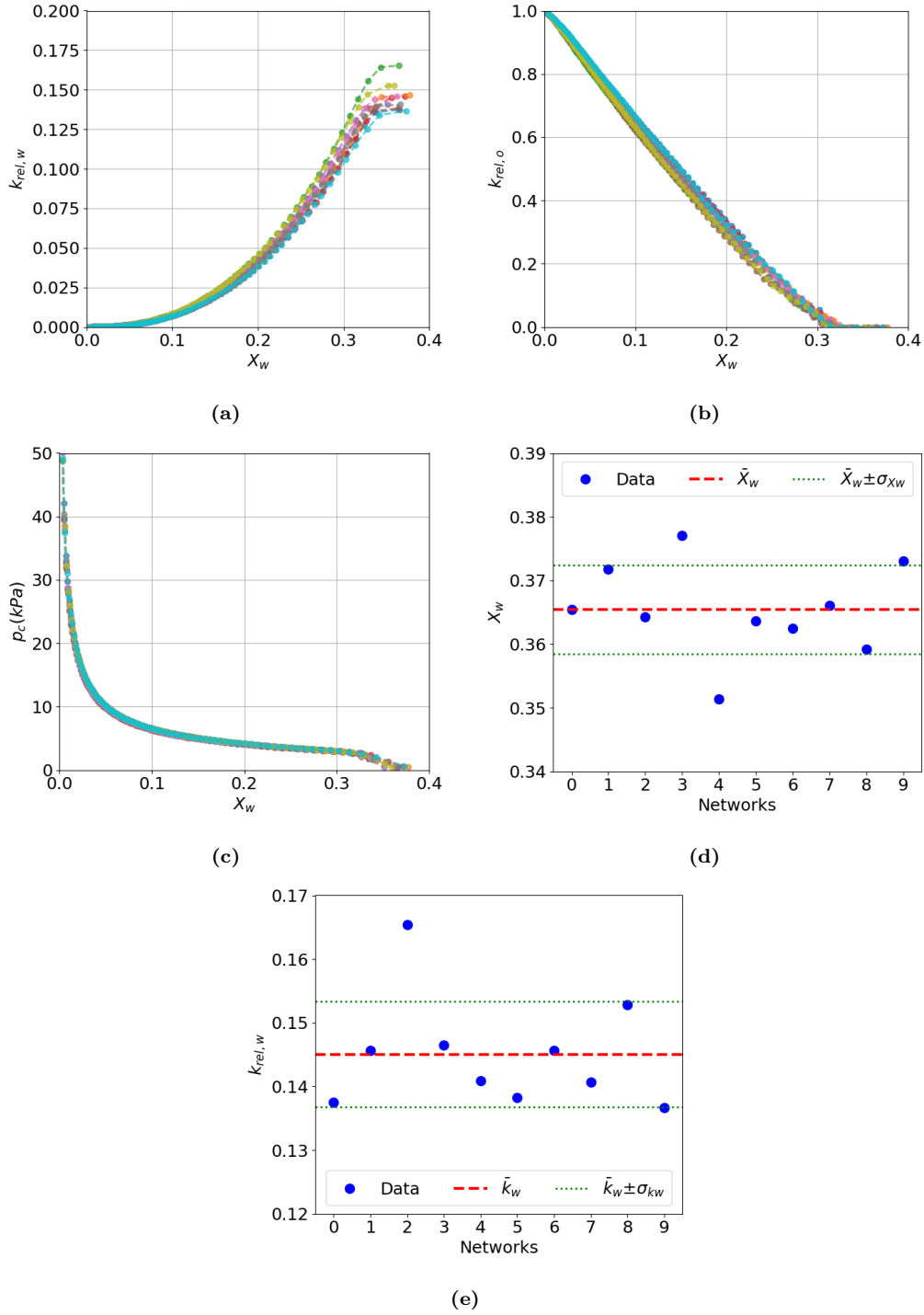


Figure 5.18: Statistical analysis of the imbibition simulation results for the C20F36 networks, considering $\theta_r = \theta_a = 0^\circ$. a) water relative permeability, b) oil relative permeability, and c) capillary pressure are sampled at every 100 states. d) final water saturation, with $\bar{X}_w = 0.365$ and $\sigma_{X_w} = 0.007$ kPa. e) final water relative permeability, with $\bar{k}_w = 0.145$ and $\sigma_{kw} = 0.008$.

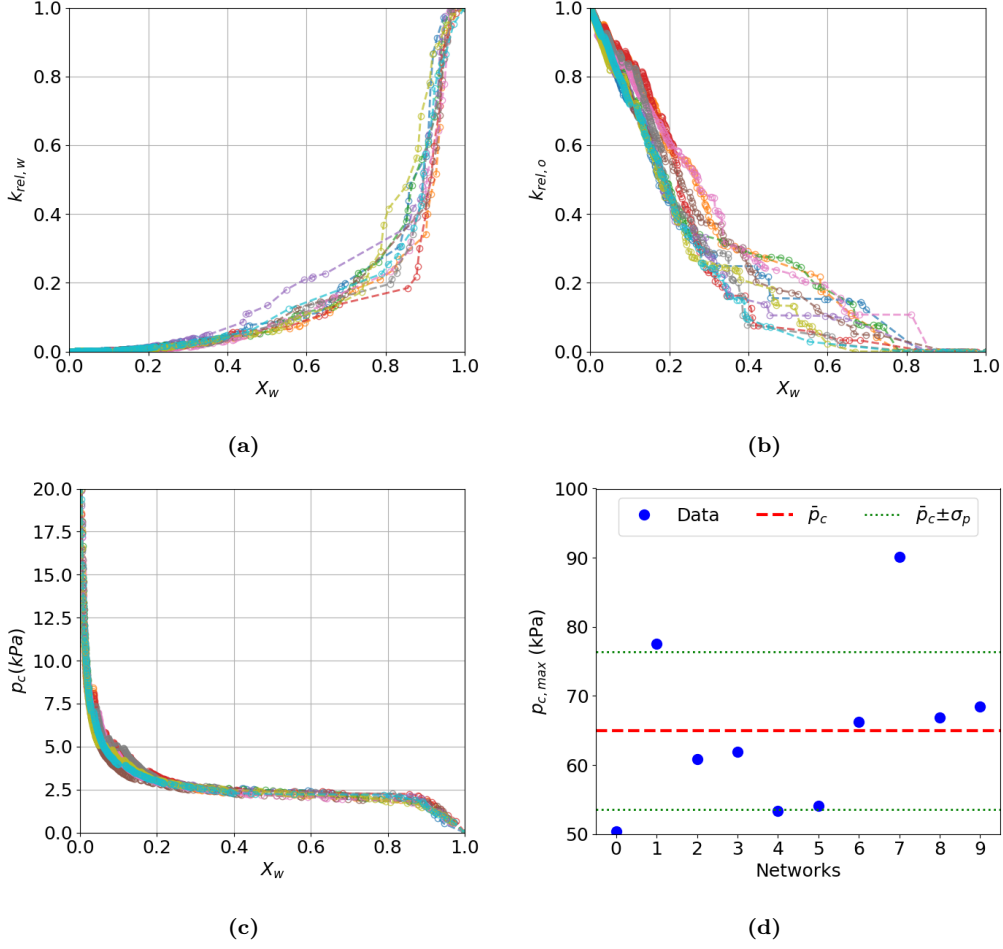


Figure 5.19: Statistical analysis of the drainage simulation results for the C10F36 networks, considering $\theta_r = 60^\circ$, $\theta_a = 110^\circ$. a) water relative permeability, b) oil relative permeability, and c) capillary pressure are sampled at every 10 states. d) maximum capillary pressure, with $\bar{p}_c = 62.5$ kPa and $\sigma_p = 19.1$ kPa.

networks. As observed in the previous results, both relative permeabilities ($k_{rel,w}$ and $k_{rel,o}$) follow a well-defined trend with respect to X_w , for the ten realizations of these networks. Moreover, the dispersions in these curves for the $20 \times 20 \times 20$ networks are significantly reduced when compared with the smaller networks. Also, despite the difference in the mean final capillary pressure (-42.7 kPa for the smallest networks and -80.5 kPa for the largest networks), all networks reach a water saturation value close to one at a $p_c \approx -6$ kPa.

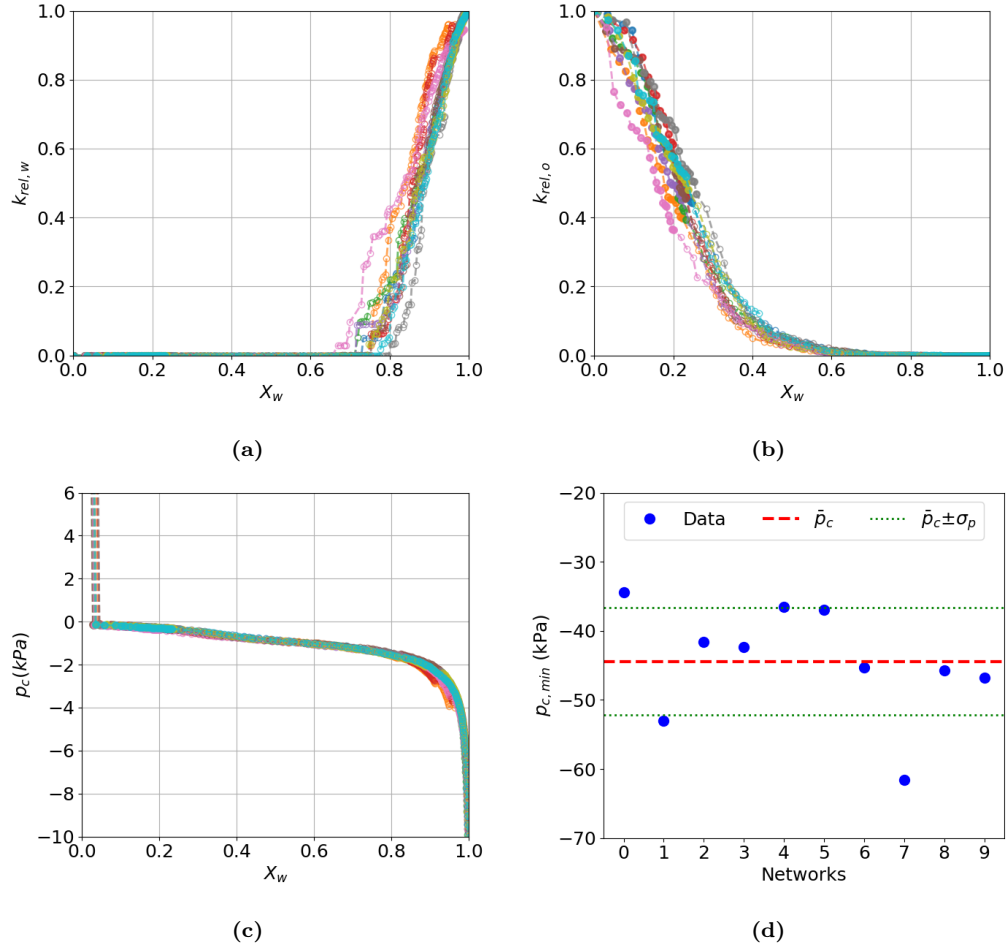


Figure 5.20: Statistical analysis of the imbibition simulation results for the C10F36 networks, considering $\theta_r = 60^\circ$, $\theta_a = 110^\circ$. a) water relative permeability, b) oil relative permeability, and c) capillary pressure are sampled first at every 4 states until state 60 (filled markers) and then every 20 states (unfilled markers). d) capillary pressure required to perform the last displacement, with $\bar{p}_c = -42.7$ kPa and $\sigma_p = 13.1$ kPa.

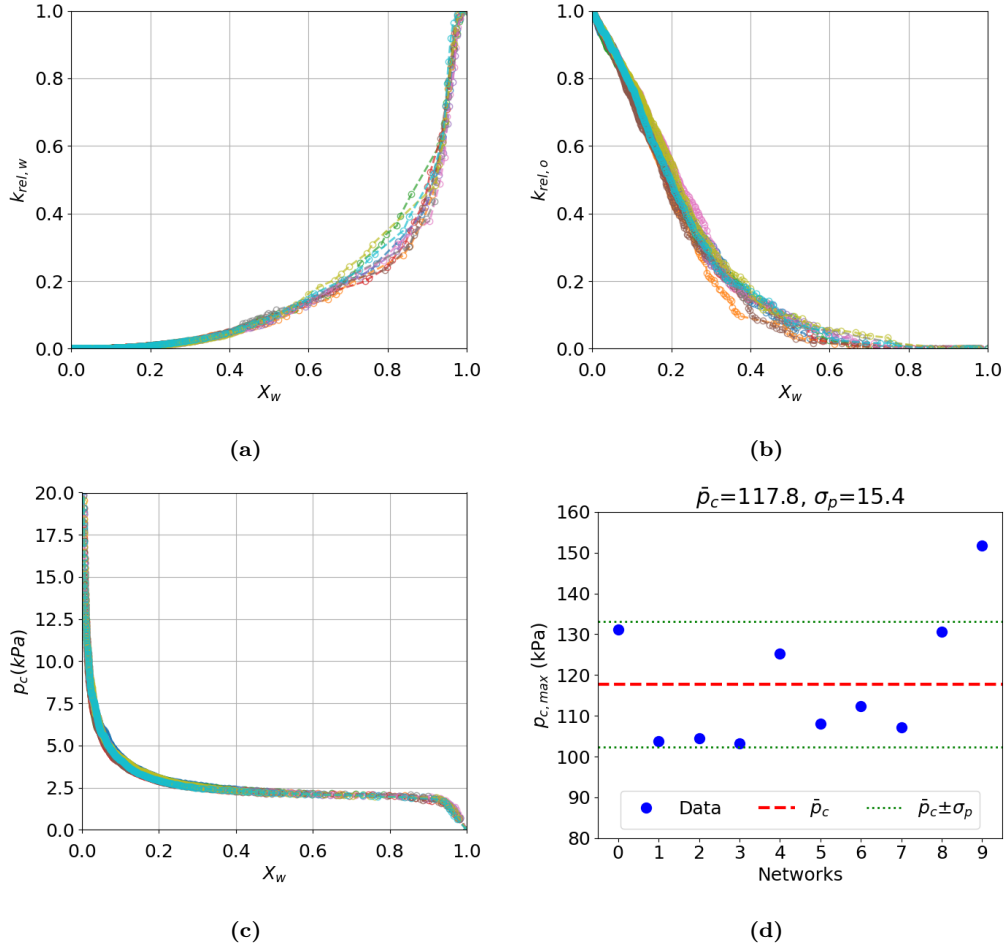


Figure 5.21: Statistical analysis of the drainage simulation for the C20F36 networks, considering $\theta_r = 60^\circ$, $\theta_a = 110^\circ$. a) water relative permeability, b) oil relative permeability, and c) capillary pressure are sampled at every 50 states. d) maximum capillary pressure, with $\bar{p}_c = 117.8$ kPa and $\sigma_p = 15.4$ kPa.

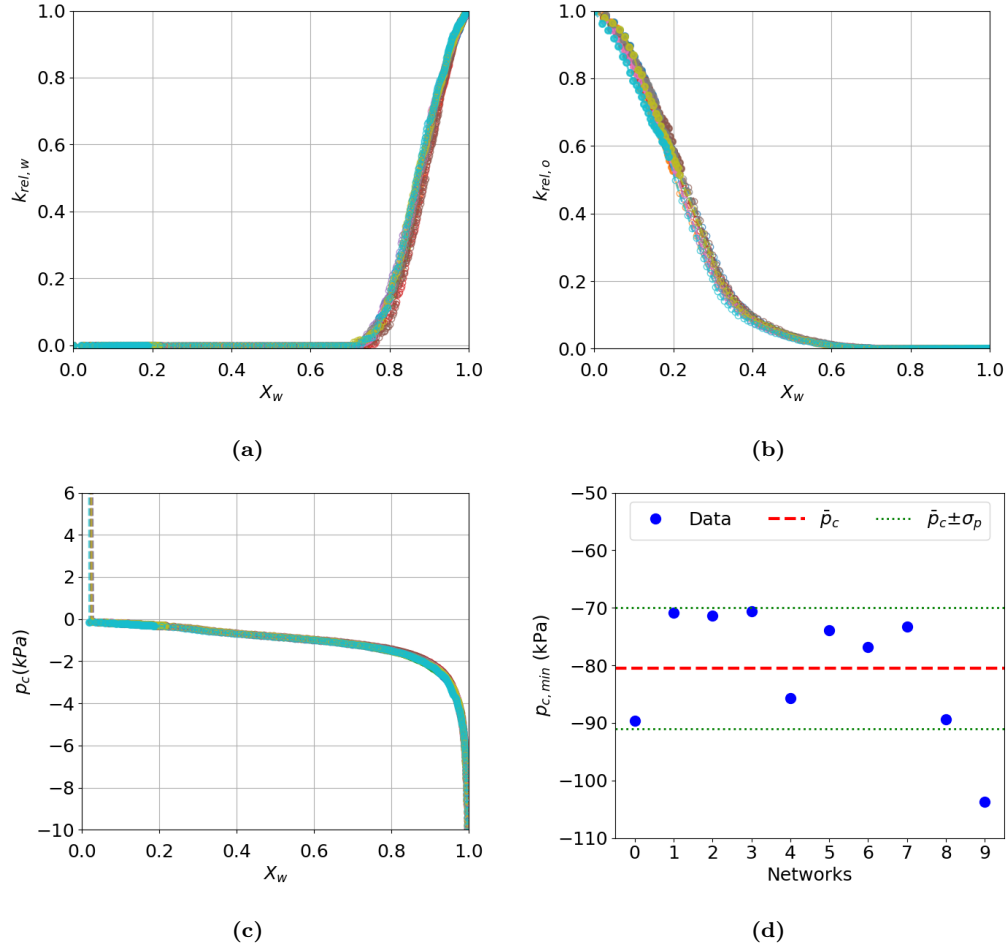


Figure 5.22: Statistical analysis of the imbibition simulation results of the C20F36 networks, considering $\theta_r = 60^\circ$, $\theta_a = 110^\circ$. a) water relative permeability, b) oil relative permeability, and c) capillary pressure are sampled first at every 20 states until state 500 (filled markers) and then every 100 states (unfilled markers). d) capillary pressure required to perform the last displacement, with $\bar{p}_c = -80.5$ kPa and $\sigma_p = 10.5$ kPa.

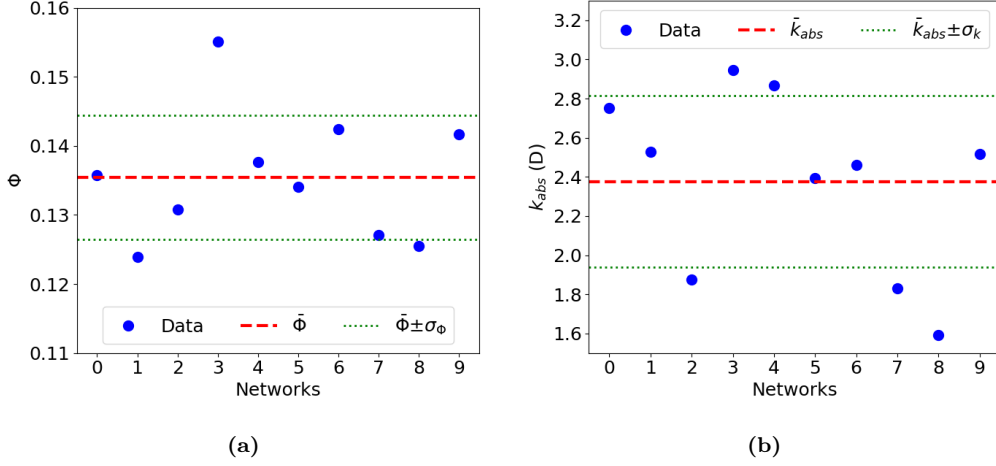


Figure 5.23: Statistical analysis of properties for CZ10F36 networks. a) porosity, with $\bar{\Phi} = 0.135$ and $\sigma_{\Phi} = 0.009$. b) absolute permeability, with $\bar{k}_{abs} = 2.38$ D and $\sigma_k = 0.44$ D.

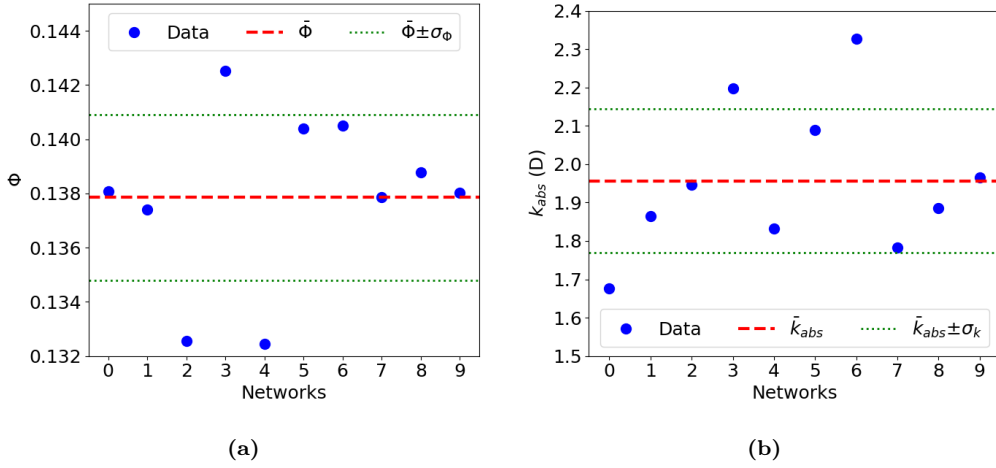


Figure 5.24: Statistical analysis of properties for CZ20F36 networks. a) porosity, with $\bar{\Phi} = 0.138$ and $\sigma_{\Phi} = 0.003$. b) absolute permeability, with $\bar{k}_{abs} = 1.96$ D and $\sigma_k = 0.19$ D.

Multi-directionally connected cubic networks

Figures 5.23 and 5.24 show the properties of the CZXF36 networks ($X = 10, 20$). The main difference between their properties and those of the CZF36 networks is that their \bar{k}_{abs} is significantly larger and the Φ is considerably lower. For the $20 \times 20 \times 20$ networks, σ_k is 9.7 % of \bar{k}_{abs} , which is larger than the result for the fully connected simple cubic networks of the same size.

The simulation results considering $\theta_r = \theta_a = 0^\circ$ are shown in Figures 5.25 and 5.26 for the smaller networks, and in Figures 5.27 and 5.28 for the larger networks. The statistical results for multidirectional networks exhibit the same pattern (a consistent trend with notable dispersion in the group of smaller networks, reduced

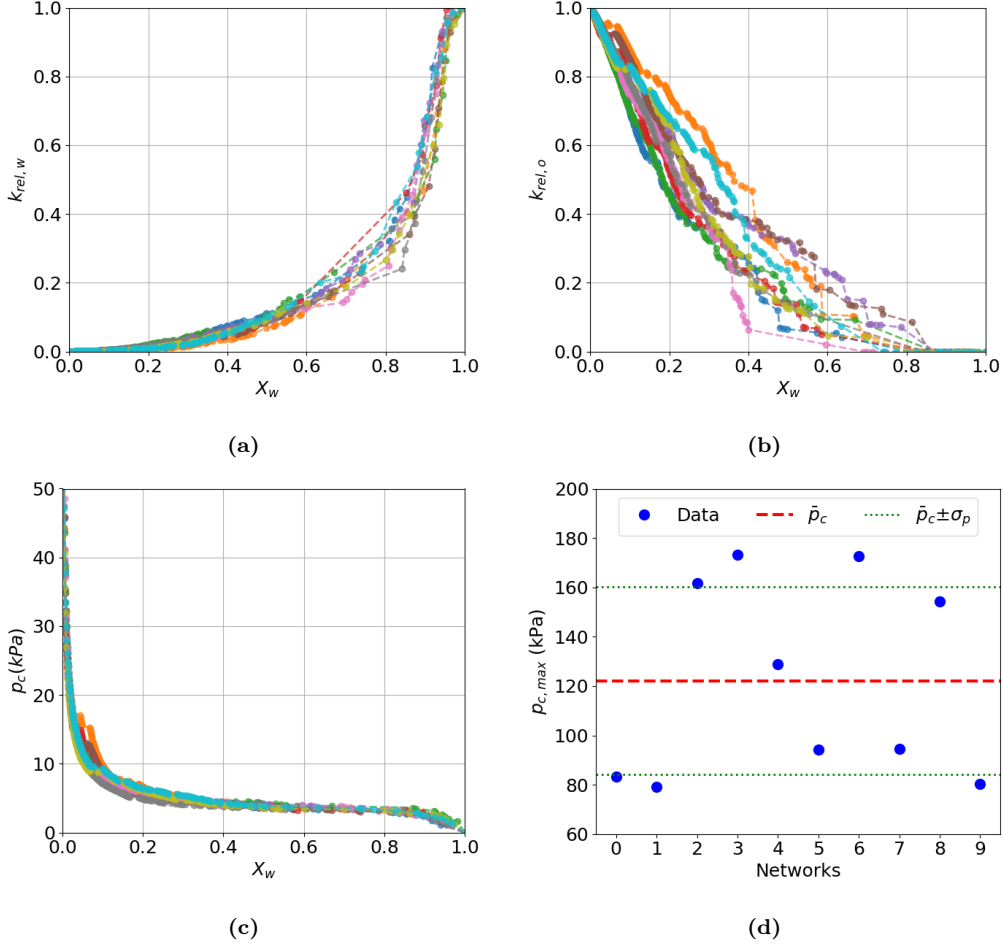


Figure 5.25: Statistical analysis of the drainage simulation results for the CZ10F36 networks, considering $\theta_r = \theta_a = 0^\circ$. a) water relative permeability, b) oil relative permeability, and c) capillary pressure are sampled at every 10 states. d) maximum capillary pressure, with $\bar{p}_c = 122.2$ kPa and $\sigma_p = 38.0$ kPa.

dispersion in the results for the group of larger networks, and p_c plots showing the lowest dispersion compared to k_{rel} plots within the same group of networks) as those obtained under identical phase conditions using networks with constant Z . However, for larger multidirectional networks, the reduction in the dispersions of $k_{rel} \times X_w$ curves between the smaller and larger networks are considerably smaller (Figures 5.25 to 5.28) than those shown in Figures 5.15 to 5.18. This may result from randomly eliminating pores and throats in the network construction method.

The simulation results considering $\theta_r = 60^\circ$, $\theta_a = 110^\circ$ are shown in Figures 5.29 and 5.30 for the smaller networks, and in Figures 5.31 and 5.32 for the larger networks. For the smaller networks, this case presents dispersion in the results of $k_{rel,o}$ and $k_{rel,w}$ during drainage and imbibition, as well as for the relationship

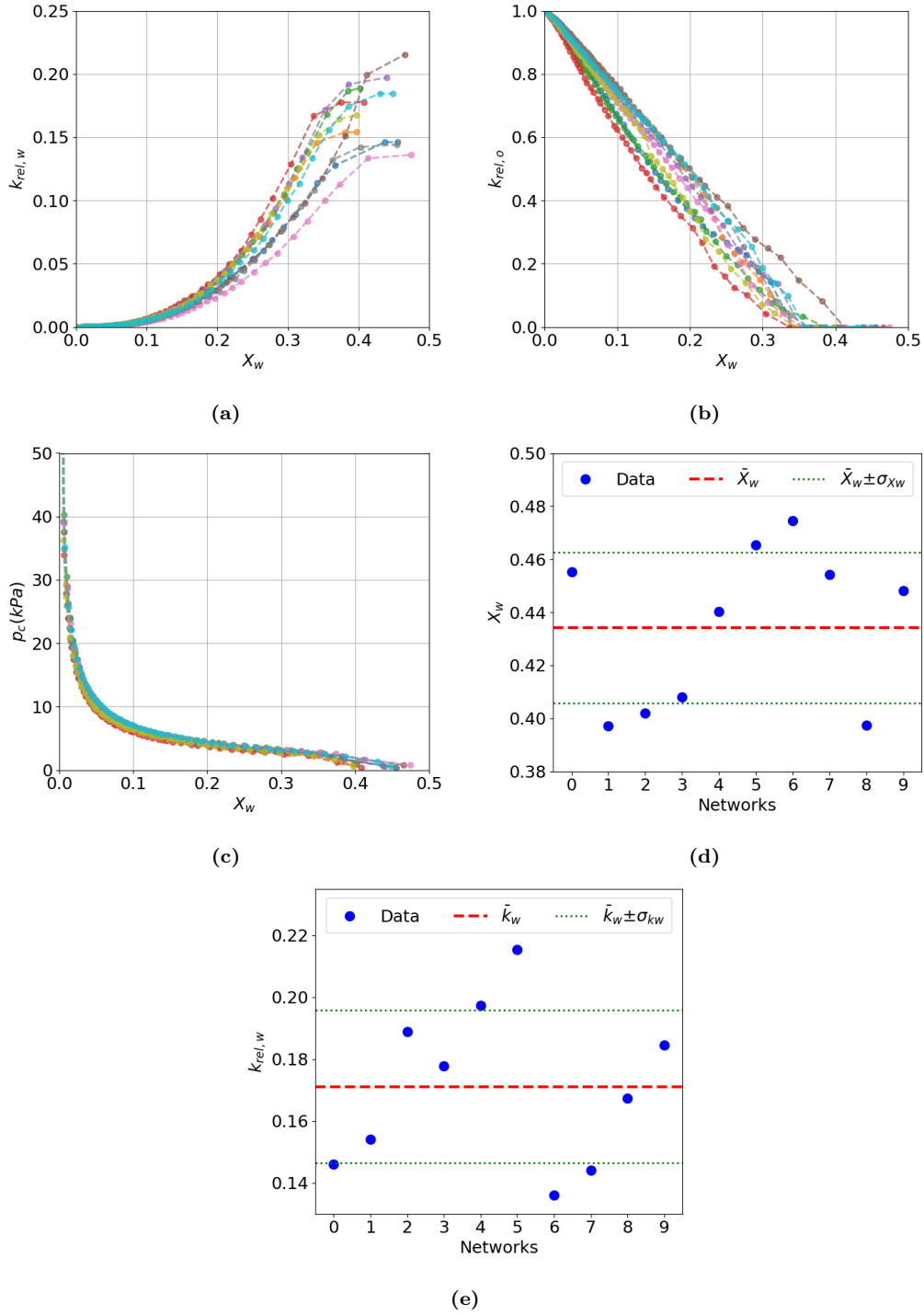


Figure 5.26: Statistical analysis of the imbibition simulation for the CZ10F36, considering $\theta_r = \theta_a = 0^\circ$. a) water relative permeability, b) oil relative permeability, and c) capillary pressure are sampled at every 20 states. d) final water saturation, with $\bar{X}_w = 0.434$ and $\sigma_{X_w} = 0.028$. e) final water relative permeability, with $\bar{k}_w = 0.171$ and $\sigma_{kw} = 0.025$.

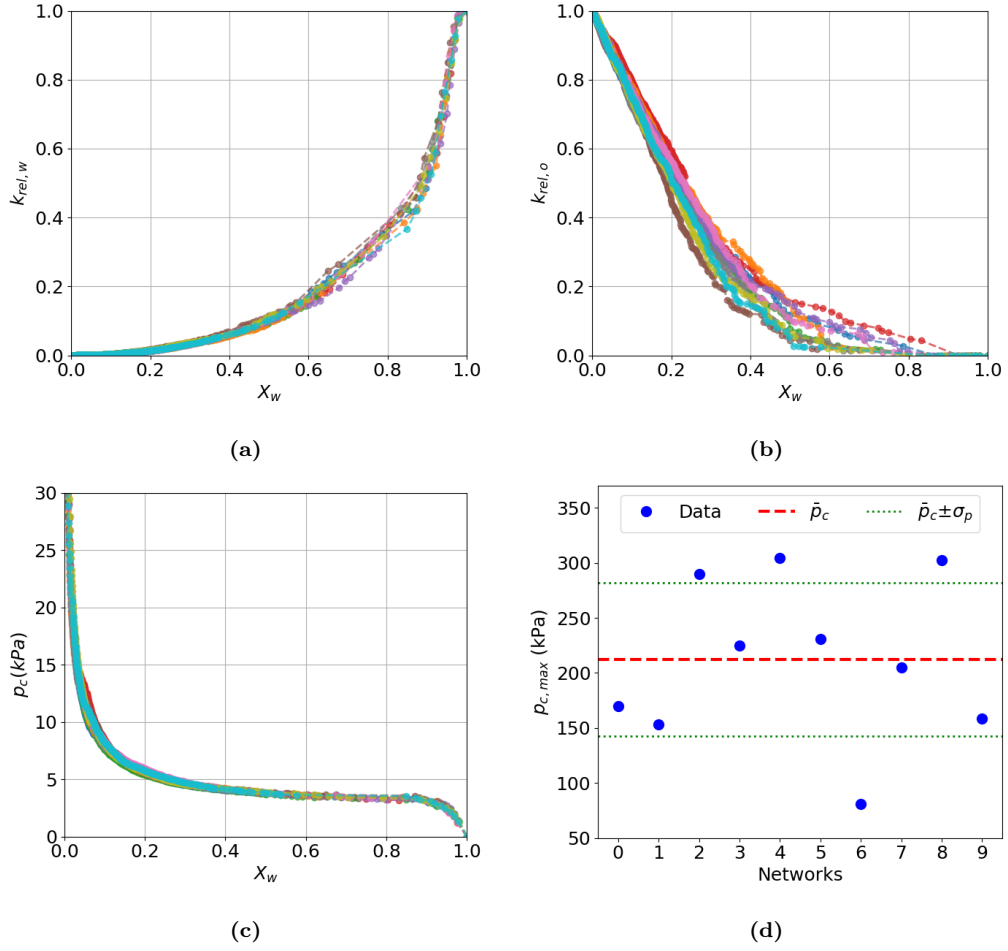


Figure 5.27: Statistical analysis of the drainage simulation results for the CZ20F36 networks, considering $\theta_r = \theta_a = 0^\circ$. a) water relative permeability, b) oil relative permeability, and c) capillary pressure are sampled at every 50 states. d) maximum capillary pressure, with $\bar{p}_c = 212.0$ kPa and $\sigma_p = 69.0$ kPa.

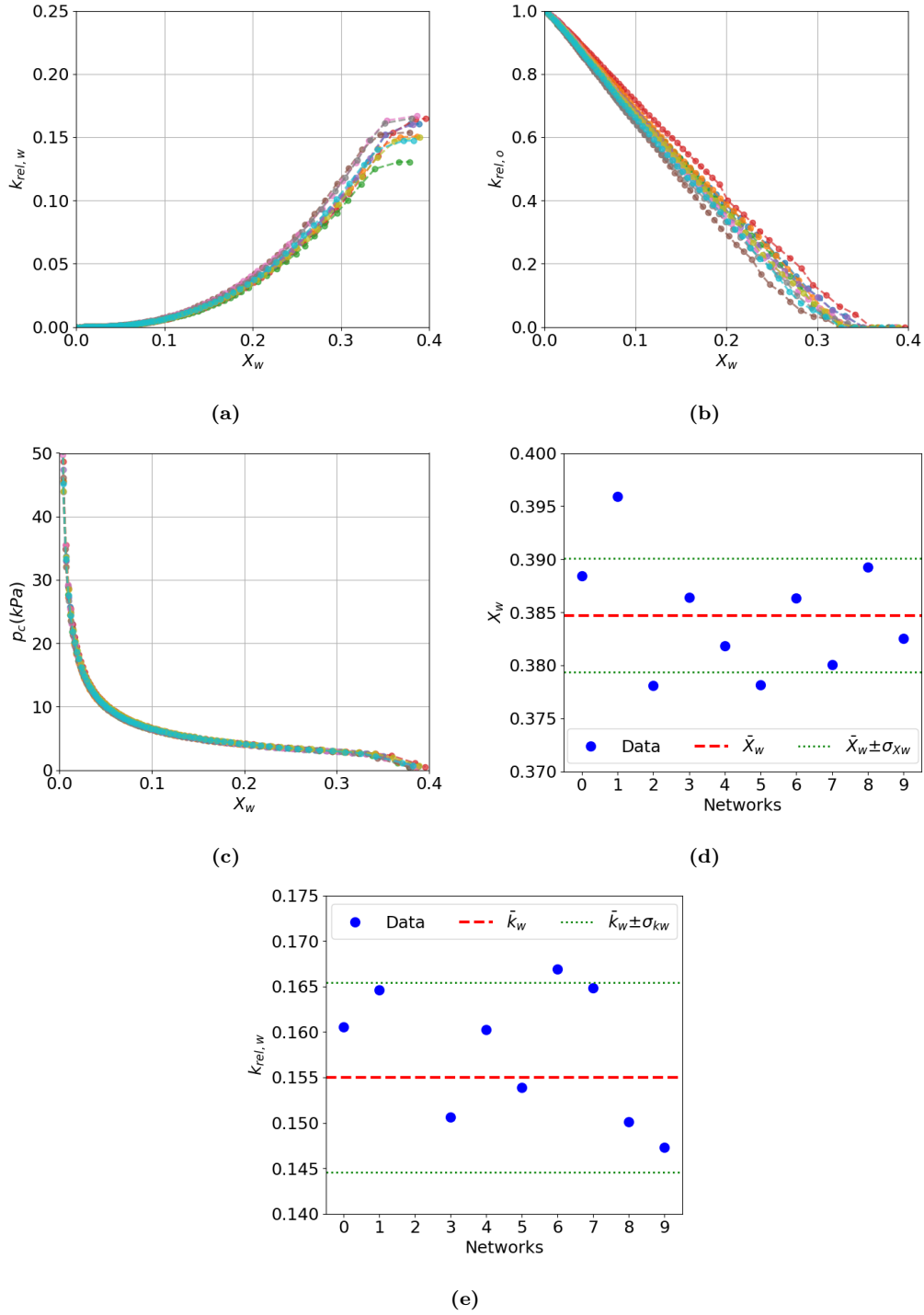


Figure 5.28: Statistical analysis of the imbibition simulation results for the CZ20F36 networks, considering $\theta_r = \theta_a = 0^\circ$. a) water relative permeability, b) oil relative permeability, and c) capillary pressure are sampled at every 100 states. d) final water saturation, with $\bar{X}_w = 0.385$ and $\sigma_{X_w} = 0.005$ kPa. e) final water relative permeability, with $\bar{k}_w = 0.158$ and $\sigma_{kw} = 0.007$.

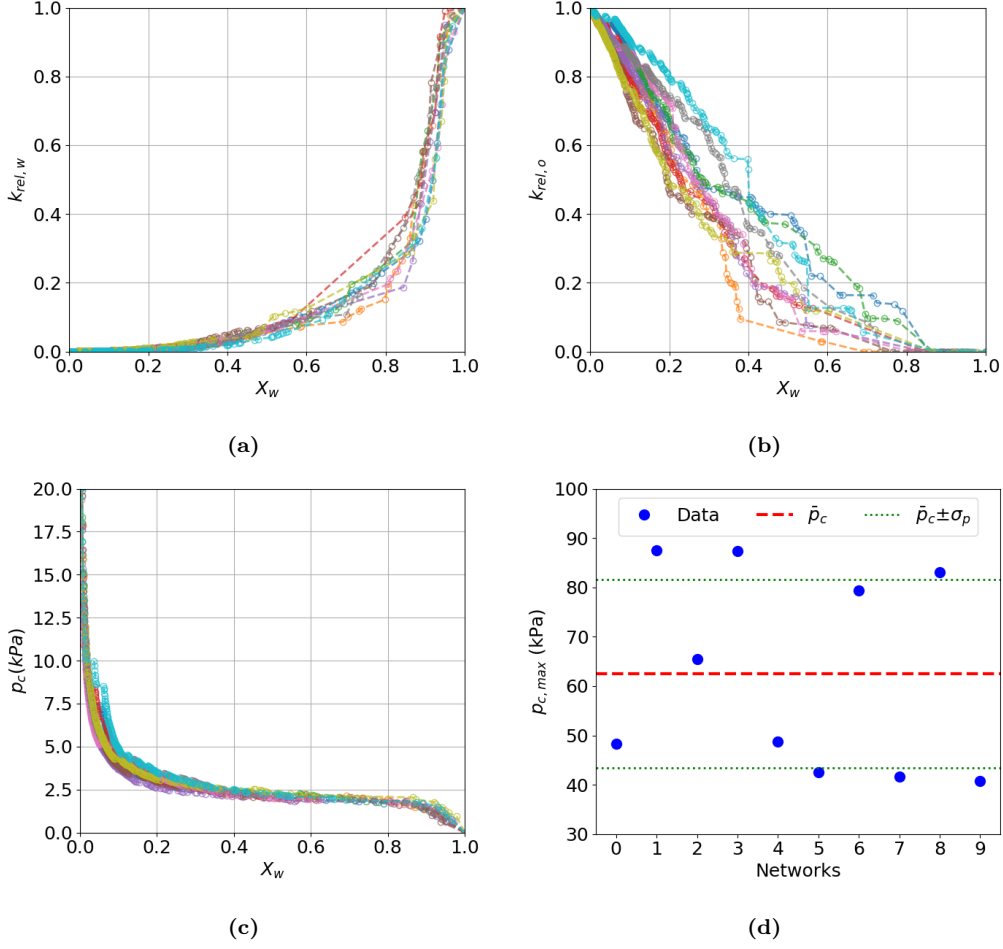


Figure 5.29: Statistical analysis of the drainage simulation results for the CZ10F36 networks, considering $\theta_r = 60^\circ$, $\theta_a = 110^\circ$. a) water relative permeability, b) oil relative permeability, and c) capillary pressure are sampled at every 10 states. d) maximum capillary pressure, with $\bar{p}_c = 62.5$ kPa and $\sigma_p = 19.1$ kPa.

between p_c and X_w . (Figure 5.29c). For the larger networks, the dispersion among the network realization results diminishes.

In conclusion, despite the additional randomness introduced by the construction of multidirectional networks and regardless of the phase properties (θ_r and θ_a), the simulator's results for large networks vary less among the network realizations. Consequently, a single $20 \times 20 \times 20$ network realization is considered adequate for the next sensitivity analyses.

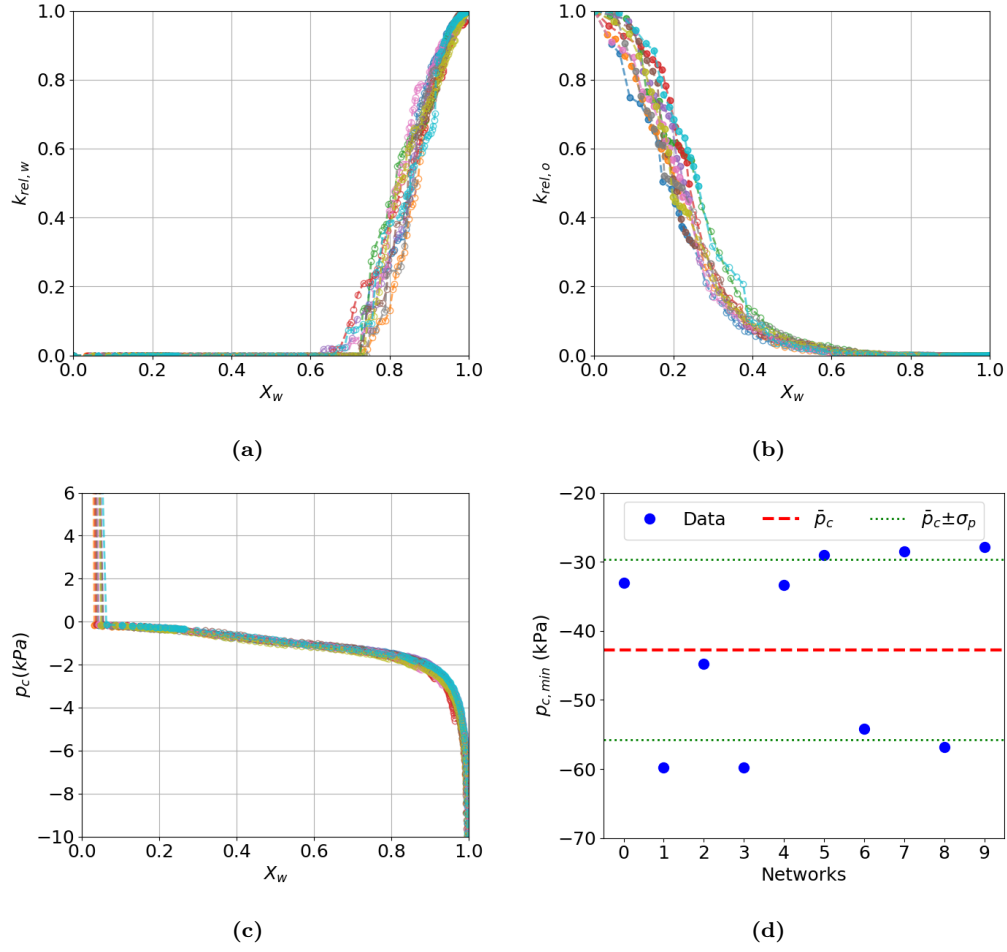


Figure 5.30: Statistical analysis of the imbibition simulation results for the CZ10F36 networks, considering $\theta_r = 60^\circ$, $\theta_a = 110^\circ$. a) water relative permeability, b) oil relative permeability, and c) capillary pressure are sampled first at every 4 states until state 60 (filled markers) and then every 20 states (unfilled markers). d) capillary pressure required to perform the last displacement, with $\bar{p}_c = -42.7$ kPa and $\sigma_p = 13.1$ kPa.

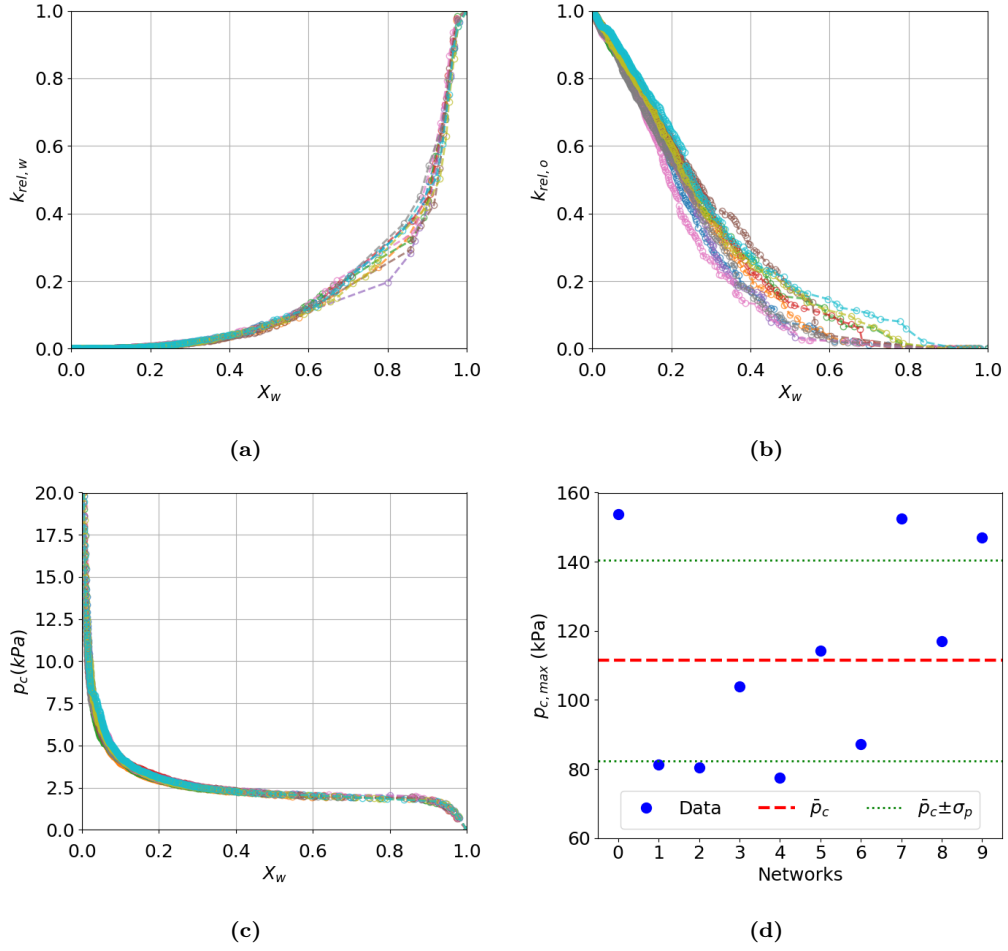


Figure 5.31: Statistical analysis of the drainage simulation results for the CZ20F36 networks, considering $\theta_r = 60^\circ$, $\theta_a = 110^\circ$. a) water relative permeability, b) oil relative permeability, and c) capillary pressure are sampled at every 50 states. d) maximum capillary pressure, with $\bar{p}_c = 111.5$ kPa and $\sigma_p = 29.1$ kPa.

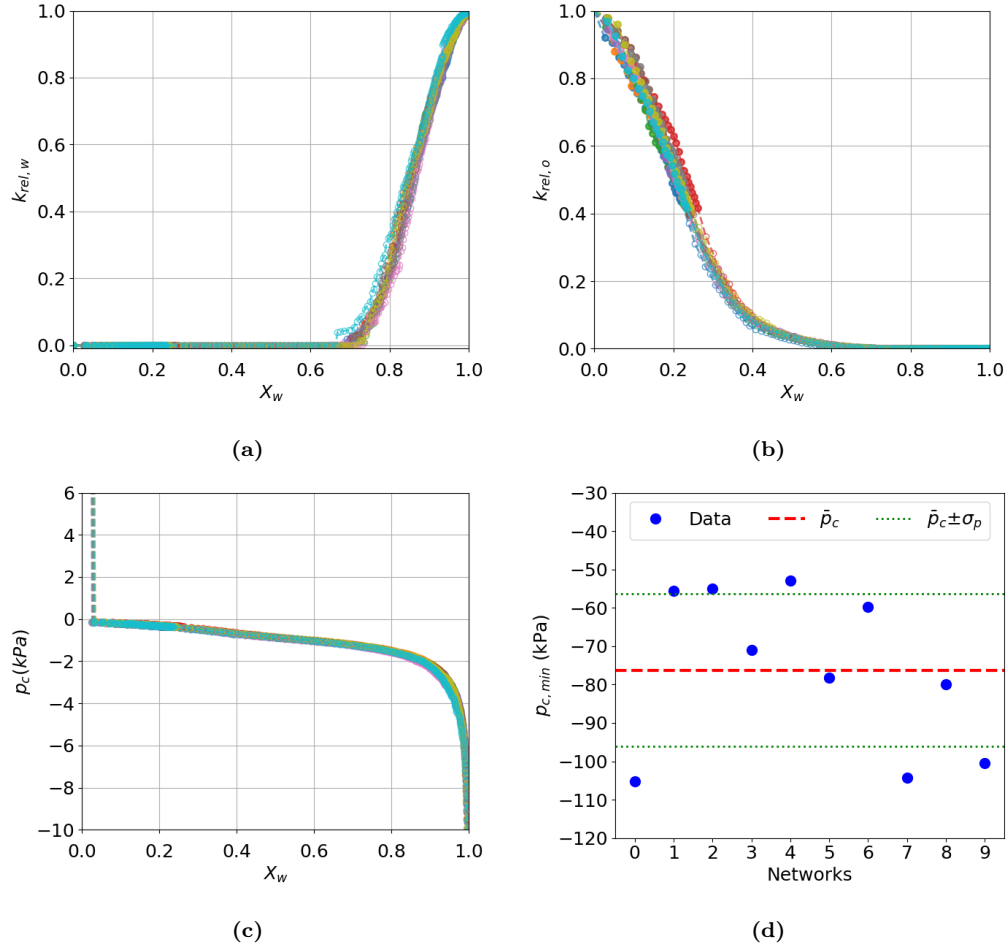


Figure 5.32: Statistical analysis of the imbibition simulation results for the CZ20F36 networks, considering $\theta_r = 60^\circ$, $\theta_a = 110^\circ$. a) water relative permeability, b) oil relative permeability, and c) capillary pressure are sampled first at every 20 states until state 500 (filled markers) and then every 100 states (unfilled markers). d) capillary pressure required to perform the last displacement, with $\bar{p}_c = -76.2$ kPa and $\sigma_p = 19.9$ kPa.

5.5.4 Influence of throat-to-pore area ratio

Figures 5.33 to 5.36 show the results for the drainage and imbibition for three values of F_{At} , giving a sensitive analysis to the throats' diameter. When water remains fully wetting throughout the process ($\theta_r = \theta_a = 0^\circ$), the relative permeability of water $k_{rel,w}$ during primary drainage is unaffected by networks with smaller throats. In contrast, the relative permeability of oil $k_{rel,o}$ is enhanced in networks with throats of larger cross-sectional area, which is expected since this phase flows through the center of pores and throats (Figure 5.33a). However, during imbibition, both $k_{rel,w}$ and $k_{rel,o}$ are impacted by F_{At} changes (Figure 5.34a). This occurs because in the elements previously invaded by oil, the area of water retained in the corners increases as capillary pressure p_c decreases, thereby influencing the flow of water and oil through the throats, especially when these are small. Notably, since the porous volume is predominantly contained in the pores, the pressure required to reach a given saturation level in drainage or imbibition remains almost independent of throat size (Figures 5.33b and 5.34b). However, $p_{c,max}$ varies with F_{At} , with values of 230.6 kPa, 214.0 kPa, and 200.6 kPa for F_{At} equal to 0.31, 0.36, and 0.41, respectively. Nonetheless, the final water saturation after imbibition is slightly higher in networks with larger throats (Fig. 5.34b). This can be explained by a decrease in snapoff events, which result in less trapped oil clusters. The percentage of snap-off displacements in throats, relative to the total invaded throats at the end of imbibition, is 44.8%, 38.8%, and 33.2% for F_{At} values of 0.31, 0.36, and 0.41, respectively, indicating a clear trend of greater snap-off occurrence with decreasing throat size.

Looking at the results from the simulations with wettability changes between the phases (Figures 5.35 and 5.36), we can see that the drainage and imbibition results for the networks with different values of F_{At} are very similar. The most noticeable difference appears in the $k_{rel,w}$ results, but only for $X_w > 0.7$. However, even then, the differences are not significant. Since this case has a weakly-wetting phase, as opposed to the previous case where water was strongly-wetting throughout

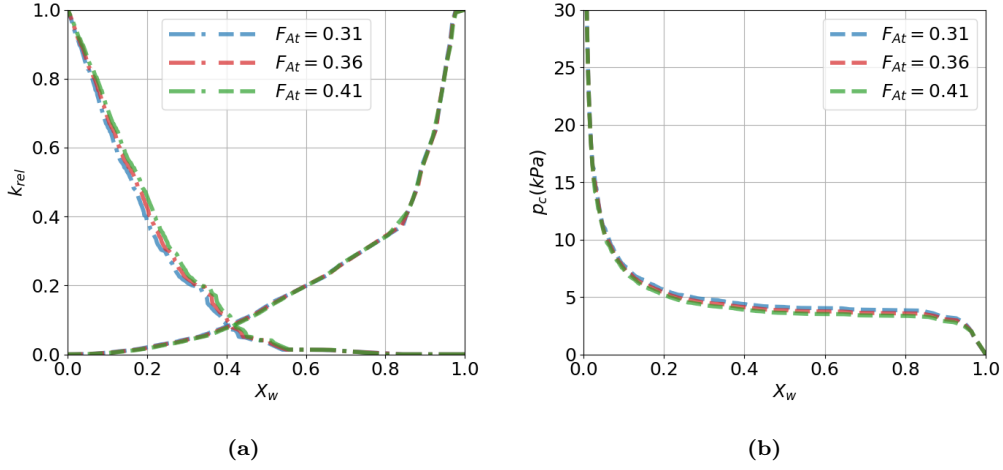


Figure 5.33: Primary drainage results using networks with different F_{At} , considering $\theta_r = \theta_a = 0^\circ$. a) relative permeability of oil (dash-dot) and water (dashed). b) capillary pressure.

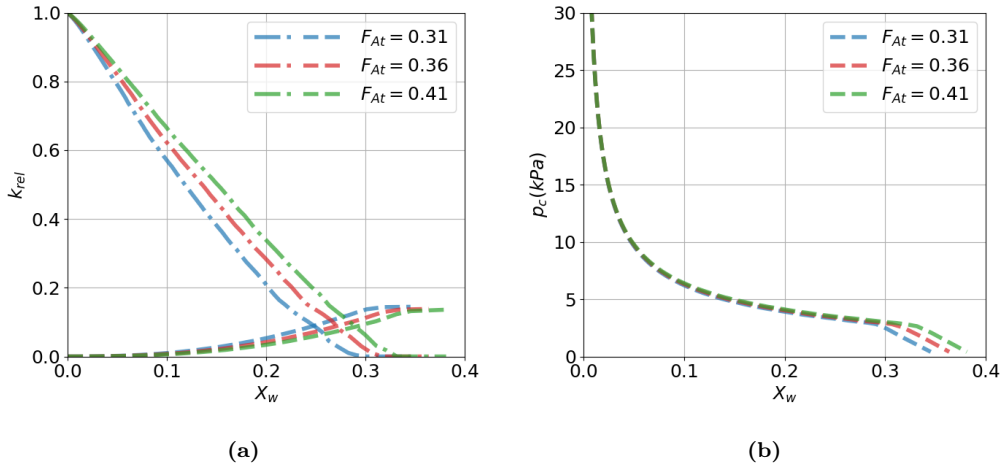


Figure 5.34: Imbibition results using networks with different F_{At} , considering $\theta_r = \theta_a = 0^\circ$. a) relative permeability of oil (dash-dot) and water (dashed). b) capillary pressure.

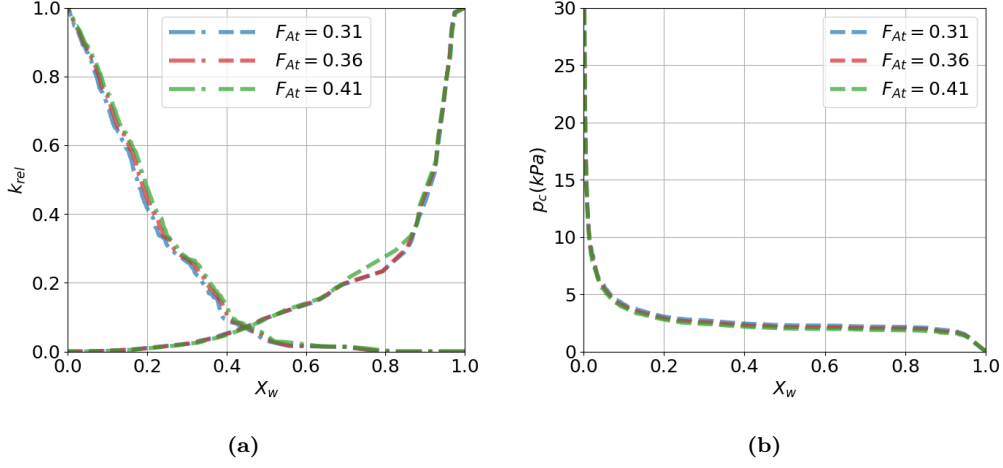


Figure 5.35: Primary drainage results using networks with different F_{At} , considering $\theta_r = 60^\circ$ and $\theta_a = 110^\circ$. a) relative permeability of oil (dash-dot) and water (dashed). b) capillary pressure.

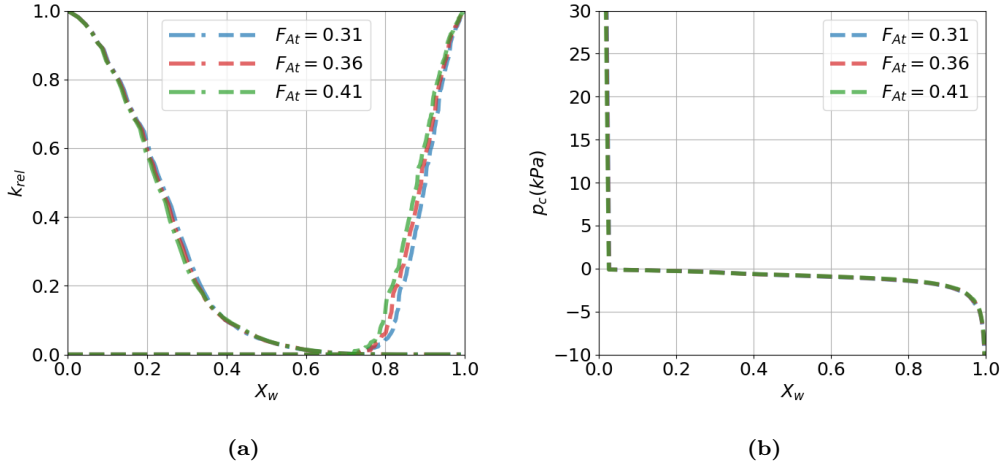


Figure 5.36: Imbibition results using networks with different F_{At} , considering $\theta_r = 60^\circ$ and $\theta_a = 110^\circ$. a) relative permeability of oil (dash-dot) and water (dashed). b) capillary pressure.

the process, we believe that the obtained behavior is caused by the decrease in the adhesion of this phase to the walls.

5.5.5 Results for different networks with the same permeability and porosity

In this analysis, we examine two networks constructed using different cubic lattices and with distinct connectivity fields and throat diameters. For the throats, the aspect ratio F_{At} differs between the two networks: 0.36 for C20F36 and 0.249 for CZ20T, as reported in Table 5.10. For the pores, there is a small variation of the mean diameter $\bar{D}_{eq,p}$, measuring 82.40 μm in the tuned network and 80.32 μm in the reference network. This difference represents only a 2.6% variation, which we assume does not significantly impact our relative permeability results.

First, we examine the results for $\theta_r = \theta_a = 0^\circ$ shown in Figures 5.37 and 5.38, representing fully wetting water conditions. During primary drainage, the relationships between $k_{rel,w}$ and X_w , as well as p_c and X_w are similar between the two networks (Figure 5.37). The $k_{rel,o}$ presents a more different behavior, with lower values observed in the C20F36 network ($F_{At} = 0.360$) compared to the network CZ20T ($F_{At} = 0.249$) at a specific X_w value. This trend is unexpected if it is just explained with the changes in F_{At} . We attribute this difference in behavior to the different connectivity field, which may affect the existence of clusters connected to inlet and outlet pores. During imbibition (Figure 5.38), however, the tendency on $k_{rel,o}$, $k_{rel,w}$, and p_c align with the influence of F_{At} . This suggests that the connectivity field may be less influential, likely because the formation of trapped clusters depends more on throat size distribution than pore-throat connectivity. Furthermore, an analysis of displacements after imbibition reveals patterns similar to those observed in the validation test (Section 5.5.1) as shown in Table 5.13: no SO,p displacement occurs in both networks, while in the tuned network CZ20T, 56.74% of the invaded throats experience snap-off, compared to 38.28% in the reference network C20F36.

Then, we examine the results for $\theta_r = 60^\circ$ and $\theta_a = 110^\circ$ shown in Figures 5.39 and 5.40, and representing a change in wettability between drainage and imbibition, without having a strong wetting phase. The observations during primary drainage exhibit the same trends as those seen in the case of fully wetting water conditions

Table 5.13: Information of displacements at the last state of the imbibition process on networks with the same Φ , k_{abs} , for a water-oil system with $\theta_r = \theta_a = 0^\circ$.

Network	C10F36	CZ10T	C20F36	CZ20T
\mathbb{F}_{abs} (PB)	610	526	4831	4469
\mathbb{F}_{abs} (SO.p)	0	0	0	0
\mathbb{F}_{abs} (PLD)	1369	697	12039	8574
\mathbb{F}_{abs} (SO.t)	930	1658	7468	11247
Invaded pores	610	526	4831	4469
Invaded throats	2299	2355	19508	19821

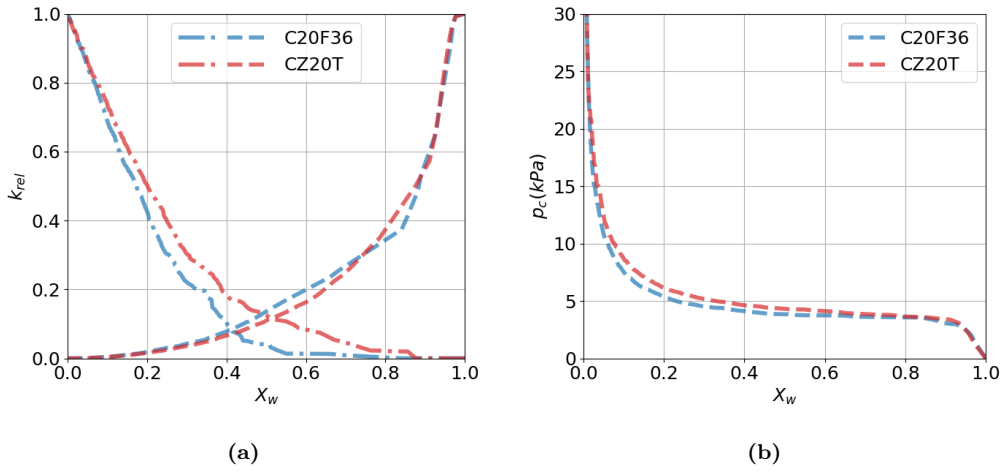


Figure 5.37: Primary drainage results using two different networks with the same Φ and k_{abs} , considering $\theta_r = \theta_a = 0^\circ$. a) relative permeability of oil (dash-dot) and water (dashed). b) capillary pressure.

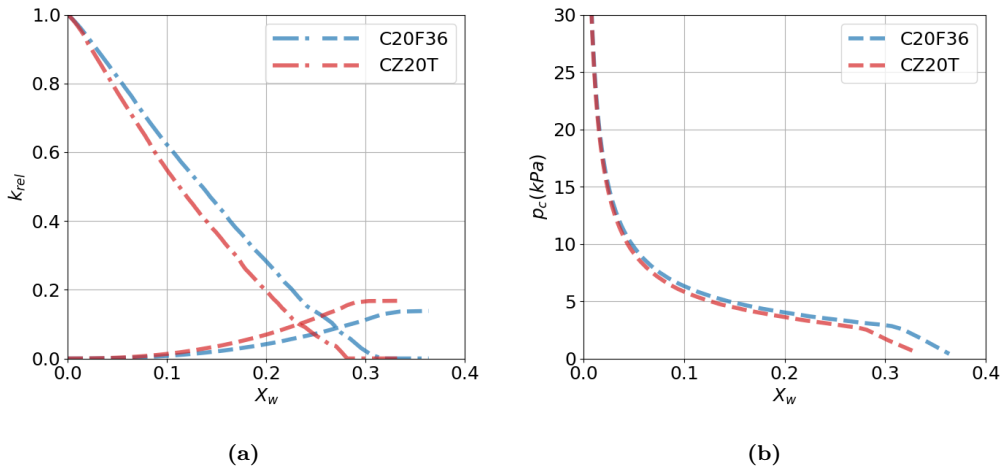


Figure 5.38: Imbibition results using two different networks with the same Φ and k_{abs} , considering $\theta_r = \theta_a = 0^\circ$. a) relative permeability of oil (dash-dot) and water (dashed). b) capillary pressure.

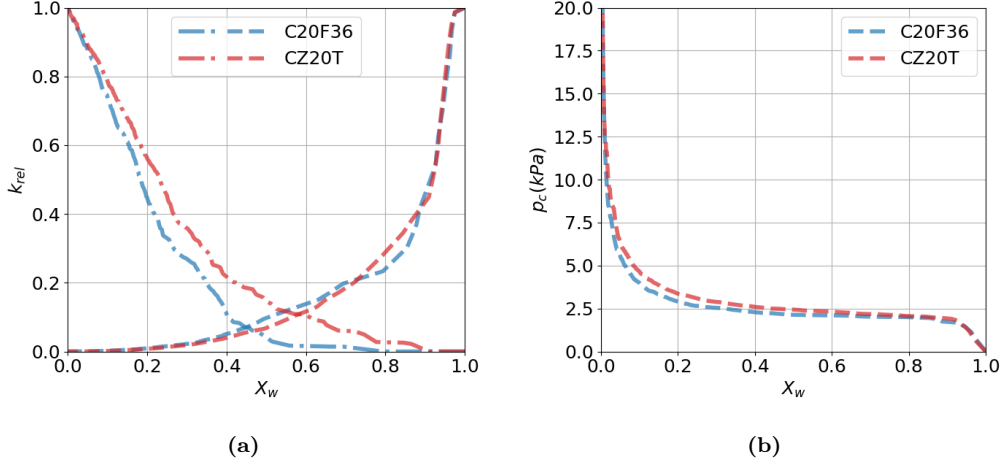


Figure 5.39: Primary drainage results using two different networks with the same Φ and k_{abs} , considering $\theta_r = 60^\circ$ and $\theta_a = 110^\circ$. a) relative permeability of oil (dash-dot) and water (dashed). b) capillary pressure.

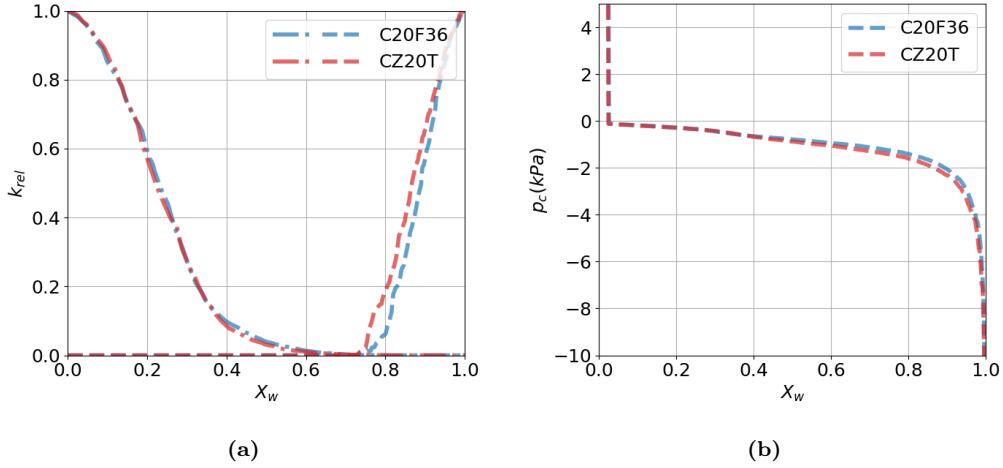


Figure 5.40: Imbibition results using two different networks with the same Φ and k_{abs} , considering $\theta_r = 60^\circ$ and $\theta_a = 110^\circ$. a) relative permeability of oil (dash-dot) and water (dashed). b) capillary pressure.

(Fig. 5.37). In contrast, comparing the imbibition results for the reference network (C20F36) and the tuned network (CZ20T), they show almost the same pattern, which is a different behavior of the simulation results from Fig. 5.38. However, for $X_w \geq 0.73$, where water-invaded pores and throats appear to form a spanning cluster in both networks, a slight divergence in $k_{rel,w}$ results emerges, which is gradually reduced as X_w increases. It is important to say that this behavior is consistent with the results observed in the validation test.

In conclusion, invasion results for two networks with identical porosity and permeability show different behaviors for the relative permeability. During primary

drainage, the oil relative permeability is predominantly influenced by the network connectivity field, regardless of phase properties. In contrast, during imbibition, the relative permeabilities $k_{rel,o}$ and $k_{rel,w}$ are affected by F_{At} only when a strongly wetting phase exists throughout the process. Beyond these effects, other relative permeability and capillary pressure results remain consistent in the simulations of both networks.

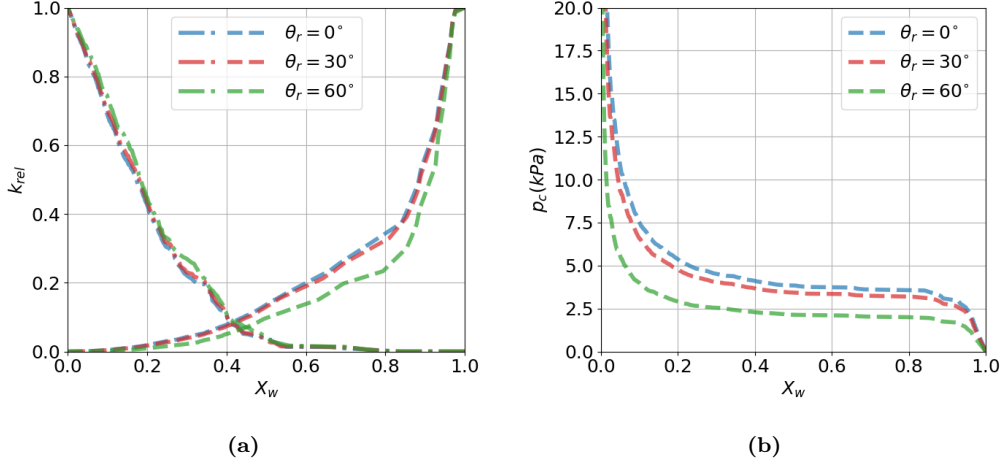


Figure 5.41: Impact of θ_r during primary drainage on the C20F36 network, considering $\theta_a = 60^\circ$. a) relative permeability of oil (dash-dot) and water (dashed). b) capillary pressure.

5.5.6 Influence of receding contact angle

Figure 5.41 shows the variations of relative permeability and capillary pressure with respect to water saturation for a sensitivity analysis to the value of θ_r . The required p_c values to invade all elements in these simulations were 214.0, 185.9, and 108.1 kPa for θ_r values of 0° , 30° , and 60° , respectively. As observed in the Berea sandstone network results, $k_{rel,w}$ is higher when the invaded phase is more wetting, which also correlates with a higher pressure needed to invade the elements. Regarding the imbibition process, the results are not displayed, as they show no dependence on θ_r , even though initial conditions, such as capillary pressure and water saturation, differed for each simulation.

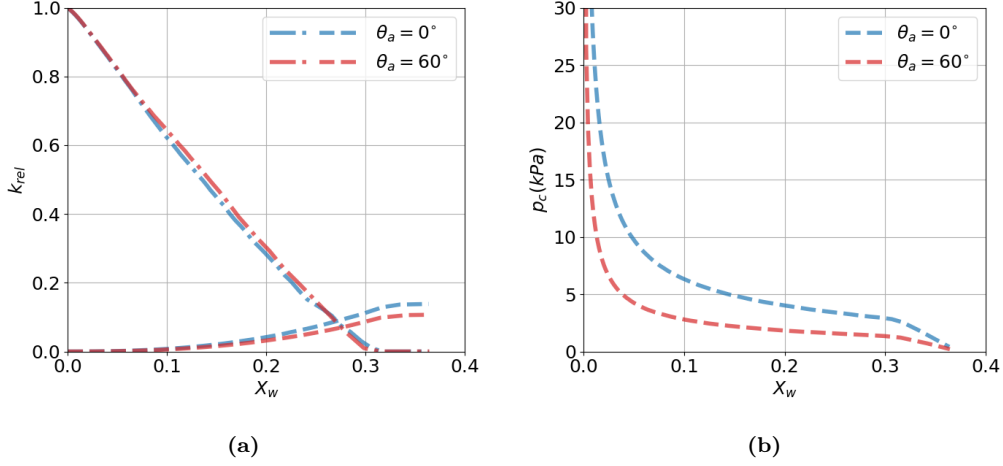


Figure 5.42: Impact of θ_a during imbibition on the C20F36 network, considering $\theta_r = 0^\circ$. a) relative permeability of oil (dash-dot) and water (dashed). b) capillary pressure.

5.5.7 Influence of advancing contact angle

Figures 5.42 and 5.43 show the variations of relative permeability and capillary pressure with respect to water saturation for a sensitivity analysis to the value of θ_a . When the receding contact angle is fixed at zero, the advancing contact angle barely influences the relative permeabilities of both phases $k_{rel,o}$ and $k_{rel,w}$ during imbibition (Figure 5.42a). The slight differences observed can be attributed to variations in the percentage of area occupied by the phases within pores and throats. In contrast, the pressure required to achieve a specific water saturation increases as the water becomes wetter (i.e., as θ_a decreases), a fully expected outcome during imbibition (Figure 5.42b). The value of θ_a did not alter the final X_w .

These trends remain consistent for $\theta_r = 60^\circ$ as well, as long as water is still the wetting phase during imbibition (Figure 5.43). However, upon a change of wettability ($\theta_a > 90^\circ$), almost all elements can be invaded, achieving a final water saturation close to 1, mainly due to the formation of oil layers that sustain the connectivity of the oil clusters.

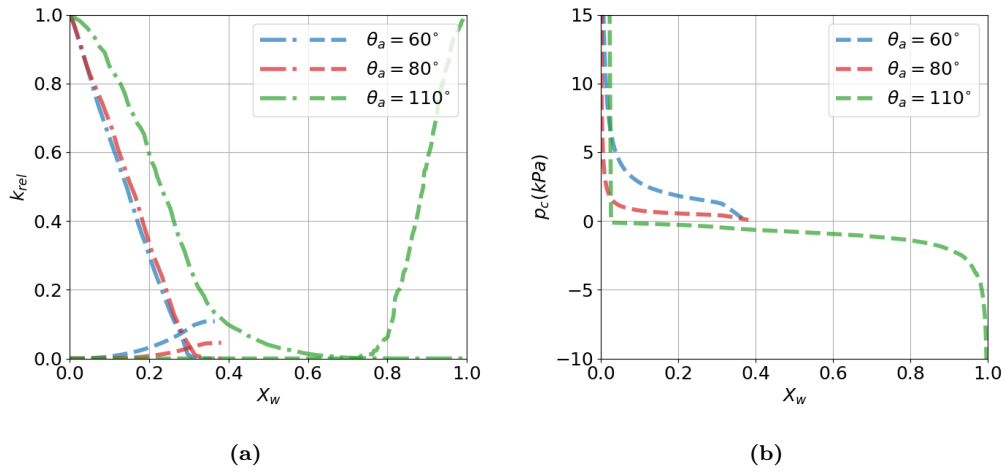


Figure 5.43: Impact of θ_a during imbibition on the C20F36 network, considering $\theta_r = 60^\circ$. a) relative permeability of oil (dash-dot) and water (dashed). b) capillary pressure.

Chapter 6

Conclusions

This study presents the development of a two-phase flow simulator for pore networks that accounts for the simultaneous presence of both phases in pores and throats. The simulation primarily relies on the software *OpenPNM* V 3.2.0, considering that some networks can be generated through modeling with *PoreSpy* V 2.2.2. In this approach, both elements are represented as triangular prisms. Mathematical relationships were also introduced to determine the invasion processes of elements during primary drainage and imbibition under quasi-static conditions and to calculate the flow rate of each phase in any quasi-static state. The results obtained from networks created using data from a Berea sample indicate that some events, like wetting-phase adhesion to walls, snap-off, and the formation of layers that maintain cluster connectivity, can be captured by the developed simulator — phenomena that cannot be properly represented using elements with circular cross sections.

Additionally, the simulator was used to perform various sensitivity analyses. It was observed that the results do not vary significantly among realizations of a network with given pore and throat size distributions, provided that the network is sufficiently large. The simulations also revealed that throat size significantly influences the relative permeability of both phases, mainly during imbibition, but only if a unique strongly-wetting phase is present throughout the entire invasion process, when the throat size becomes a more dominant factor than the network connectivity field. When working with networks with different connectivity fields but similar

porosity and permeability values, the k_{rel} vs X_w relationships remain largely unaffected, except in two cases: (1) the relative permeability of the invading phase during drainage, and (2) the relative permeability of both phases during imbibition, but only when a single strongly wetting phase is maintained throughout the process. Also, θ_r affects only primary drainage results and not imbibition, as long as full network invasion occurs during primary drainage. On the other hand, imbibition results are strongly influenced by phase wettability conditions. If the wetting phase during drainage becomes non-wetting during imbibition, more layers can form, maintaining connectivity and enabling near-complete network invasion.

6.1 Future work suggestions

It is important to implement a subsequent drainage process after imbibition or to improve the simulator to work with networks that include elements with different cross-sectional shapes, such as squares and circles. However, with the current tool, it would be interesting to perform simulations where the invaded phase during the imbibition process becomes completely non-wetting. Additionally, areas for improvement have been identified in the implemented codes, which could help reduce computational costs.

References

- AKBARI, M., SINTON, D., BAHRAMI, M., 2011, “Viscous flow in variable cross-section microchannels of arbitrary shapes”, *International Journal of Heat and Mass Transfer*, v. 54, n. 17, pp. 3970–3978. ISSN: 0017-9310. doi: <https://doi.org/10.1016/j.ijheatmasstransfer.2011.04.028>. Disponível em: <<https://www.sciencedirect.com/science/article/pii/S001793101100247X>>.
- BAKKE, S., ØREN, P.-E., 1997, “3-D Pore-Scale Modelling of Sandstones and Flow Simulations in the Pore Networks”, *SPE Journal*, v. 2, n. 02 (06), pp. 136–149. ISSN: 1086-055X. doi: 10.2118/35479-PA. Disponível em: <<https://doi.org/10.2118/35479-PA>>.
- BAUER, D., YOUSSEF, S., HAN, M., et al., 2011, “From computed microtomography images to resistivity index calculations of heterogeneous carbonates using a dual-porosity pore-network approach: Influence of percolation on the electrical transport properties”, *Phys. Rev. E*, v. 84 (Jul), pp. 011133. doi: 10.1103/PhysRevE.84.011133. Disponível em: <<https://link.aps.org/doi/10.1103/PhysRevE.84.011133>>.
- BLUNT, M., 2022. “Pore-Scale Modelling and Imaging”. <https://www.imperial.ac.uk/earth-science/research/research-groups/pore-scale-modelling/micro-ct-images-and-networks/>. Acesso em 4 de jun. 2023.
- BLUNT, M. J., 1997a, “Effects of Heterogeneity and Wetting on Relative Permeability Using Pore Level Modeling”, *SPE Journal*, v. 2, n. 01 (03), pp. 70–87. ISSN: 1086-055X. doi: 10.2118/36762-PA. Disponível em: <<https://doi.org/10.2118/36762-PA>>.
- BLUNT, M. J., 1997b, “Pore Level Modeling of the Effects of Wettability”, *SPE Journal*, v. 2, n. 04 (12), pp. 494–510. ISSN: 1086-055X. doi: 10.2118/38435-PA. Disponível em: <<https://doi.org/10.2118/38435-PA>>.

- BLUNT, M. J., 1998, “Physically-based network modeling of multiphase flow in intermediate-wet porous media”, *Journal of Petroleum Science and Engineering*, v. 20, n. 3, pp. 117–125. ISSN: 0920-4105. doi: [https://doi.org/10.1016/S0920-4105\(98\)00010-2](https://doi.org/10.1016/S0920-4105(98)00010-2). Disponível em: <<https://www.sciencedirect.com/science/article/pii/S0920410598000102>>.
- BLUNT, M. J., 2017, *Multiphase Flow in Permeable Media: A Pore-Scale Perspective*. Cambridge, Cambridge University Press. doi: 10.1017/9781316145098.002.
- BLUNT, M. J., BAZYLAK, A., BROOK, M., et al., 2024, “Research Needs in Porous Media for the Energy Transition”, *InterPore Journal*, v. 1, n. 1 (Apr.), pp. ipj260424–2. doi: 10.69631/ipj.v1i1nr14. Disponível em: <<https://ipjournal.interpore.org/index.php/interpore/article/view/14>>.
- BOGGS, P. T., BYRD, R. H., ROGERS, J. E., et al., 1992, “User’s reference guide for ODRPACK version 2.01: software for weighted orthogonal distance regression”. 6. Disponível em: <<https://api.semanticscholar.org/CorpusID:126352852>>.
- CHEN, S., DOOLEN, G. D., 1998, “LATTICE BOLTZMANN METHOD FOR FLUID FLOWS”, *Annual Review of Fluid Mechanics*, v. 30, n. Volume 30, 1998, pp. 329–364. ISSN: 1545-4479. doi: <https://doi.org/10.1146/annurev.fluid.30.1.329>. Disponível em: <<https://www.annualreviews.org/content/journals/10.1146/annurev.fluid.30.1.329>>.
- CLAASSEN, C., FATHIGANJEHLOU, A., PETERS, E., et al., 2025, “Mechanical Solute Dispersion in slender packed bed reactors: Comparing Pore Network Modeling and Particle-Resolved CFD”, *International Journal of Heat and Mass Transfer*, v. 240, pp. 126630. ISSN: 0017-9310. doi: <https://doi.org/10.1016/j.ijheatmasstransfer.2024.126630>. Disponível em: <<https://www.sciencedirect.com/science/article/pii/S0017931024014571>>.
- CUI, R., HASSANIZADEH, S. M., SUN, S., 2022, “Pore-network modeling of flow in shale nanopores: Network structure, flow principles, and computational algorithms”, *Earth-Science Reviews*, v. 234, pp. 104203. doi: <https://doi.org/10.1016/j.earscirev.2022.104203>.
- DONG, H., 2007, *Micro-CT imaging and pore network extraction*. Tese de Doutorado, Imperial College London.

- FATHIGANJEHLOU, A., EGHBALMANESH, A., BALTUSSEN, M., et al., 2023, “Pore network modelling of slender packed bed reactors”, *Chemical Engineering Science*, v. 273, pp. 118626. ISSN: 0009-2509. doi: <https://doi.org/10.1016/j.ces.2023.118626>. Disponível em: <<https://www.sciencedirect.com/science/article/pii/S0009250923001823>>.
- FRISS, H. A., PEDERSON, J., JETTESTUEN, E., et al., 2019, “OpenPNM: A Pore Network Modeling Package”, *Computing in Science and Engineering*, v. 128, pp. 123–151. doi: <https://doi.org/10.1007/s11242-019-01238-6>.
- GOSTICK, J., KHAN, Z., TRANTER, T., et al., 2019, “PoreSpy: A Python Toolkit for Quantitative Analysis of Porous Media Images”, *Journal of Open Source Software*. doi: <https://doi.org/10.21105/joss.01296>. Disponível em: <<https://www.sciencedirect.com/science/article/pii/S0734189X84900355>>.
- GOSTICK, J., AGHIGHI, M., HINEBAUGH, J., et al., 2016, “OpenPNM: A Pore Network Modeling Package”, *Computing in Science and Engineering*, v. 18, n. 4, pp. 60–74. doi: 10.1109/MCSE.2016.49.
- GOSTICK, J. T., 2017, “Versatile and efficient pore network extraction method using marker-based watershed segmentation”, *Phys. Rev. E*, v. 96 (Aug), pp. 023307. doi: 10.1103/PhysRevE.96.023307. Disponível em: <<https://link.aps.org/doi/10.1103/PhysRevE.96.023307>>.
- HÄRTEL, C., 1996, “Chapter 5 - Turbulent flows: Direct numerical simulation and large-eddy simulation”. In: Peyret, R. (Ed.), *Handbook of Computational Fluid Mechanics*, Academic Press, pp. 283–338, London. ISBN: 978-0-12-553010-1. doi: <https://doi.org/10.1016/B978-012553010-1/50006-2>. Disponível em: <<https://www.sciencedirect.com/science/article/pii/B9780125530101500062>>.
- LENORMAND, R., ZARCONI, C., SARR, A., 1983, “Mechanisms of The Displacement of One Fluid by Another in a Network of Capillary Ducts”, *Journal of Fluid Mechanics*, v. 135 (10). doi: 10.1017/S0022112083003110.
- LI, H., SHEN, Z., ZHANG, X., et al., 2024, “Fractal geometry of fingering front morphologies of water and NAPL flow in homogeneous porous media: A comparison study”, *Science of The Total Environment*, v. 946, pp. 174098. ISSN: 0048-9697. doi: <https://doi.org/10.1016/j.scitotenv.2024.174098>. Disponível em: <<https://www.sciencedirect.com/science/article/pii/S0048969724042463>>.

- LI, J., MCDUGALL, S., SORBIE, K., 2017, “Dynamic pore-scale network model (PNM) of water imbibition in porous media”, *Advances in Water Resources*, v. 107, pp. 191–211. ISSN: 0309-1708. doi: <https://doi.org/10.1016/j.advwatres.2017.06.017>. Disponível em: <<https://www.sciencedirect.com/science/article/pii/S0309170816304687>>.
- LIU, X., PENG, C., BAI, H., et al., 2020, “A pore network model for calculating pressure drop in packed beds of arbitrary-shaped particles”, *AIChE Journal*, v. 66, n. 9, pp. e16258. doi: <https://doi.org/10.1002/aic.16258>. Disponível em: <<https://aiche.onlinelibrary.wiley.com/doi/abs/10.1002/aic.16258>>.
- LIU, Y., ZOU, S., HE, Y., et al., 2021, “Influence of fractal surface roughness on multiphase flow behavior: Lattice Boltzmann simulation”, *International Journal of Multiphase Flow*, v. 134, pp. 103497. ISSN: 0301-9322. doi: <https://doi.org/10.1016/j.ijmultiphaseflow.2020.103497>. Disponível em: <<https://www.sciencedirect.com/science/article/pii/S030193222030608X>>.
- LONDON, I. C., 2021. “pnextract: Pore Network Extraction from Micro-CT Images of Porous Media”. Disponível em: <<https://github.com/ImperialCollegeLondon/pnextract>>. Accessed: 28 March 2025.
- LORENSEN, W. E., CLINE, H. E., 1987, “Marching cubes: A high resolution 3D surface construction algorithm”, v. 21, n. 4 (ago.), pp. 163–169. ISSN: 0097-8930. doi: [10.1145/37402.37422](https://doi.org/10.1145/37402.37422). Disponível em: <<https://doi.org/10.1145/37402.37422>>.
- MACHADO, A. V. L., LAGE, P. L. C., COUTO, P., 2024, “Boundary-fitted and voxelized meshes in rocks’ permeability simulations”. In: *Anais do IV Congresso Brasileiro de Fluidodinâmica Computacional*, 9.
- MACHADO, A. V., LAGE, P. L., COUTO, P., 2023, “Sub-volume analysis of pore-network simulations: Determining the asymptotic longitudinal dispersion coefficient”, *Advances in Water Resources*, v. 181, pp. 104541. ISSN: 0309-1708. doi: <https://doi.org/10.1016/j.advwatres.2023.104541>. Disponível em: <<https://www.sciencedirect.com/science/article/pii/S0309170823001756>>.
- MALENICA, L., ZHANG, Z., ANGST, U., 2024, “Towards improved understanding of spontaneous imbibition into dry porous media using pore-scale direct numerical simulations”, *Advances in Water Resources*,

- v. 194, pp. 104840. ISSN: 0309-1708. doi: <https://doi.org/10.1016/j.advwatres.2024.104840>. Disponível em: <<https://www.sciencedirect.com/science/article/pii/S0309170824002276>>.
- MANWART, C., AALTOSALMI, U., KOPONEN, A., et al., 2002, “Lattice-Boltzmann and finite-difference simulations for the permeability for three-dimensional porous media”, *Phys. Rev. E*, v. 66 (Jul), pp. 016702. doi: 10.1103/PhysRevE.66.016702. Disponível em: <<https://link.aps.org/doi/10.1103/PhysRevE.66.016702>>.
- MCDOUGALL, S. R., SORBIE, K. S., 1995, “The Impact of Wettability on Waterflooding: Pore-Scale Simulation”, *SPE Reservoir Engineering*, v. 10, n. 03 (08), pp. 208–213. ISSN: 0885-9248. doi: 10.2118/25271-PA. Disponível em: <<https://doi.org/10.2118/25271-PA>>.
- MEIJSTER, A., ROERDINK, J. B. T. M., HESSELINK, W. H., 2000, “A General Algorithm for Computing Distance Transforms in Linear Time”. In: *Mathematical Morphology and its Applications to Image and Signal Processing*, pp. 331–340, Boston, MA, Springer US. ISBN: 978-0-306-47025-7. doi: 10.1007/0-306-47025-X_36. Disponível em: <https://doi.org/10.1007/0-306-47025-X_36>.
- MORROW, N. R., 1976, “Capillary Pressure Correlations For Uniformly Wetted Porous Media”, *Journal of Canadian Petroleum Technology*, v. 15, n. 04 (10). ISSN: 0021-9487. doi: 10.2118/76-04-05. Disponível em: <<https://doi.org/10.2118/76-04-05>>.
- OAK, M. J., 1990, “Three-Phase Relative Permeability of Water-Wet Berea”, v. All Days (04), pp. SPE–20183–MS. Disponível em: <<https://doi.org/10.2118/20183-MS>>.
- OPENCFD, 2024. “OpenFOAM®”. Available in <https://www.openfoam.com/news/main-news/openfoam-v2212>.
- OREN, P.-E., BAKKE, S., HENRIQUEZ, A., et al., 1996, “Prediction of Relative Permeability and Capillary Pressure from a Pore Model”. 04. doi: 10.2523/35531-MS.
- ØREN, P., BAKKE, S., 2002, “Process Based Reconstruction of Sandstones and Prediction of Transport Properties”, *Transport in Porous Media*, v. 46, pp. 311–343. Disponível em: <<https://api.semanticscholar.org/CorpusID:67835408>>.

- PATZEK, T., SILIN, D., 2001, “Shape Factor and Hydraulic Conductance in Non-circular Capillaries: I. One-Phase Creeping Flow”, *Journal of Colloid and Interface Science*, v. 236, n. 2, pp. 295–304. ISSN: 0021-9797. doi: <https://doi.org/10.1006/jcis.2000.7413>. Disponível em: <<https://www.sciencedirect.com/science/article/pii/S0021979700974137>>.
- PIRI, M., 2003, *Pore-Scale Modelling of Three-Phase Flow*. Tese de Doutorado, Imperial College London.
- RABBANI, A., BABAEI, M., 2019, “Hybrid pore-network and lattice-Boltzmann permeability modelling accelerated by machine learning”, *Advances in Water Resources*, v. 126, pp. 116–128. ISSN: 0309-1708. doi: <https://doi.org/10.1016/j.advwatres.2019.02.012>. Disponível em: <<https://www.sciencedirect.com/science/article/pii/S0309170818311059>>.
- RABBANI, A., BABAEI, M., 2021, “Image-based modeling of carbon storage in fractured organic-rich shale with deep learning acceleration”, *Fuel*, v. 299, pp. 120795. ISSN: 0016-2361. doi: <https://doi.org/10.1016/j.fuel.2021.120795>. Disponível em: <<https://www.sciencedirect.com/science/article/pii/S0016236121006724>>.
- RABBANI, A., BABAEI, M., JAVADPOUR, F., 2020, “A Triple Pore Network Model (T-PNM) for Gas Flow Simulation in Fractured, Micro-porous and Meso-porous Media”, *Transport in Porous Media*, v. 132, n. 3 (4), pp. 707–740. ISSN: 1573-1634. doi: [10.1007/s11242-020-01409-w](https://doi.org/10.1007/s11242-020-01409-w). Disponível em: <<https://doi.org/10.1007/s11242-020-01409-w>>.
- SEIDL, V., MUZAFERIJA, S., PERIĆ, M., et al., 1997, “- Direct numerical simulation of flow around sphere with an unstructured fully implicit parallel navier-stokes solver”. In: Schiano, P., Ecer, A., Periaux, J., et al. (Eds.), *Parallel Computational Fluid Dynamics 1996*, North-Holland, pp. 100–107, Amsterdam. ISBN: 978-0-444-82327-4. doi: <https://doi.org/10.1016/B978-044482327-4/50079-6>. Disponível em: <<https://www.sciencedirect.com/science/article/pii/B9780444823274500796>>.
- SHAMS, M., RAEINI, A. Q., BLUNT, M. J., et al., 2018, “A numerical model of two-phase flow at the micro-scale using the volume-of-fluid method”, *Journal of Computational Physics*, v. 357, pp. 159–182. ISSN: 0021-9991. doi: <https://doi.org/10.1016/j.jcp.2017.12.027>. Disponível em: <<https://www.sciencedirect.com/science/article/pii/S002199911730921X>>.

- SHENG, Q., THOMPSON, K., 2016, “A unified pore-network algorithm for dynamic two-phase flow”, *Advances in Water Resources*, v. 95, pp. 92–108. ISSN: 0309-1708. doi: <https://doi.org/10.1016/j.advwatres.2015.12.010>. Disponível em: <<https://www.sciencedirect.com/science/article/pii/S0309170815300038>>. Pore scale modeling and experiments.
- SHOKRI, J., SCHOLLENBERGER, T., AN, S., et al., 2024, “Upscaling the reaction rates in porous media from pore- to Darcy-scale”, *Chemical Engineering Journal*, v. 493, pp. 152000. ISSN: 1385-8947. doi: <https://doi.org/10.1016/j.cej.2024.152000>. Disponível em: <<https://www.sciencedirect.com/science/article/pii/S1385894724034879>>.
- SILIN, D., PATZEK, T., 2006, “Pore space morphology analysis using maximal inscribed spheres”, *Physica A: Statistical Mechanics and its Applications*, v. 371, n. 2, pp. 336–360. ISSN: 0378-4371. doi: <https://doi.org/10.1016/j.physa.2006.04.048>. Disponível em: <<https://www.sciencedirect.com/science/article/pii/S037843710600464X>>.
- SIMONOV, O. A., ERINA, Y. Y., PONOMAREV, A. A., 2023, “Review of modern models of porous media for numerical simulation of fluid flows”, *Heliyon*, v. 9, n. 12, pp. e22292. ISSN: 2405-8440. doi: <https://doi.org/10.1016/j.heliyon.2023.e22292>. Disponível em: <<https://www.sciencedirect.com/science/article/pii/S2405844023095002>>.
- SOILLE, P. J., ANSOULT, M. M., 1990, “Automated basin delineation from digital elevation models using mathematical morphology”, *Signal Processing*, v. 20, n. 2, pp. 171–182. ISSN: 0165-1684. doi: [https://doi.org/10.1016/0165-1684\(90\)90127-K](https://doi.org/10.1016/0165-1684(90)90127-K). Disponível em: <<https://www.sciencedirect.com/science/article/pii/016516849090127K>>.
- STONE, H., 1970, “Probability Model for Estimating Three-Phase Relative Permeability”, *Journal of Petroleum Technology*, v. 22, n. 02 (02), pp. 214–218. ISSN: 0149-2136. doi: 10.2118/2116-PA. Disponível em: <<https://doi.org/10.2118/2116-PA>>.
- STONE, H., 1973, “Estimation of Three-Phase Relative Permeability And Residual Oil Data”, *Journal of Canadian Petroleum Technology*, v. 12, n. 04 (10). ISSN: 0021-9487. doi: 10.2118/73-04-06. Disponível em: <<https://doi.org/10.2118/73-04-06>>.
- TAGHAVINEJAD, A., RABBANI, A., FALCONE, G., et al., 2025, “Pore network modelling of CO₂-shale interaction for carbon storage: Swelling effect and

- fracture permeability”, *International Journal of Greenhouse Gas Control*, v. 141, pp. 104294. ISSN: 1750-5836. doi: <https://doi.org/10.1016/j.ijggc.2024.104294>. Disponível em: <<https://www.sciencedirect.com/science/article/pii/S1750583624002378>>.
- TARTAKOVSKY, A. M., TRASK, N., PAN, K., et al., 2016, “Smoothed particle hydrodynamics and its applications for multiphase flow and reactive transport in porous media”, *Computational Geosciences*, v. 20, pp. 807–834. doi: <https://doi.org/10.1007/s10596-015-9468-9>.
- VALVATNE, P. H., BLUNT, M. J., 2004, “Predictive pore-scale modeling of two-phase flow in mixed wet media”, *Water Resources Research*, v. 40, n. 7. doi: <https://doi.org/10.1029/2003WR002627>. Disponível em: <<https://agupubs.onlinelibrary.wiley.com/doi/abs/10.1029/2003WR002627>>.
- VAN DER WALT, S., SCHÖNBERGER, J. L., NUNEZ-IGLESIAS, J., et al., 2014, “scikit-image: image processing in Python”, *PeerJ*, v. 2 (6), pp. e453. ISSN: 2167-8359. doi: [10.7717/peerj.453](https://doi.org/10.7717/peerj.453). Disponível em: <<https://doi.org/10.7717/peerj.453>>.
- VIRTANEN, P., GOMMERS, R., OLIPHANT, T. E., et al., 2020, “SciPy 1.0: Fundamental Algorithms for Scientific Computing in Python”, *Nature Methods*, v. 17, pp. 261–272. doi: [10.1038/s41592-019-0686-2](https://doi.org/10.1038/s41592-019-0686-2).
- WANG, W., XIE, Q., AN, S., et al., 2023, “Pore-scale simulation of multiphase flow and reactive transport processes involved in geologic carbon sequestration”, *Earth-Science Reviews*, v. 247, pp. 104602. ISSN: 0012-8252. doi: <https://doi.org/10.1016/j.earscirev.2023.104602>. Disponível em: <<https://www.sciencedirect.com/science/article/pii/S001282522300291X>>.
- WHITE, F., 2002, *Fluid Mechanics*. Rhode Island, WCB/McGraw-Hill.
- YANG, S.-Y., HIRASAKI, G., BASU, S., et al., 1999, “Mechanisms for contact angle hysteresis and advancing contact angles”, *Journal of Petroleum Science and Engineering*, v. 24, n. 2, pp. 63–73. ISSN: 0920-4105. doi: [https://doi.org/10.1016/S0920-4105\(99\)00049-2](https://doi.org/10.1016/S0920-4105(99)00049-2). Disponível em: <<https://www.sciencedirect.com/science/article/pii/S0920410599000492>>.
- ØREN, P.-E., BAKKE, S., ARNTZEN, O. J., 1998, “Extending Predictive Capabilities to Network Models”, *SPE Journal*, v. 3, n. 04 (12), pp. 324–336.

ØREN, P.-E., BAKKE, S., 2003, “Reconstruction of Berea sandstone and pore-scale modeling of wettability effects”, *Journal of Petroleum Science and Engineering*, v. 39 (09), pp. 177–199. doi: 10.1016/S0920-4105(03)00062-7.

Appendix A

Modeling throats as isosceles triangular prisms

A.1 Algorithm to build pixelized isosceles triangles

Considering an isosceles triangle where the repeated angle is $2\beta_1$ located on the opposite side of a_1 (see Figure [A.1a](#)), it is possible to express parameters such as the height h , the other side a_2 and the area A as a function of β_1 and a_1 .

$$a_2 = 2a_1 \cos(2\beta_1) \tag{A.1}$$

$$h = a_1 \sin(2\beta_1) \tag{A.2}$$

$$A = \frac{1}{2}a_2h = a_1^2 \sin(2\beta_1) \cos(2\beta_1) \tag{A.3}$$

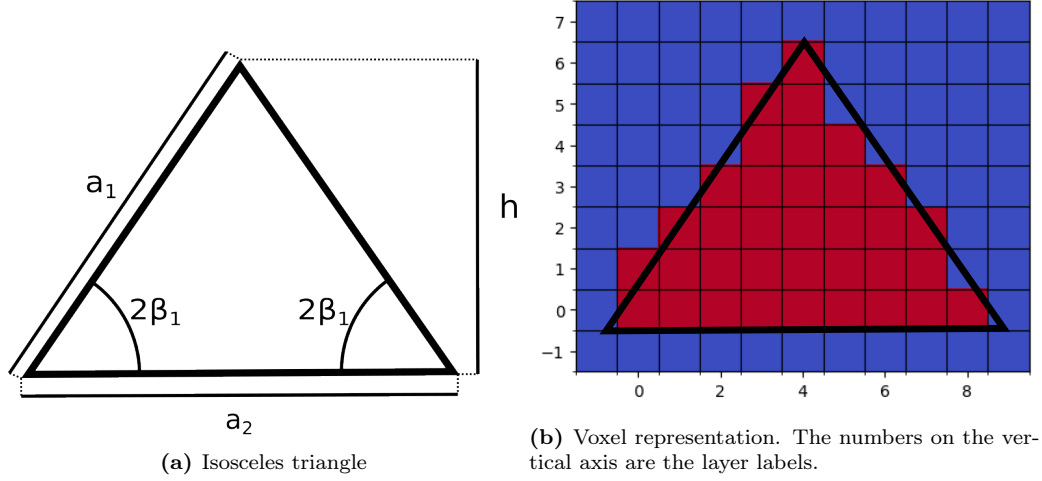


Figure A.1: Conversion into pixels of an isosceles triangle with $A = 35u^2$ and $h = 7u$. Voxel size $= 1u$

Representing the triangle with n_v pixels of length l_v , as in Figure A.1b, the area is:

$$A_v = n_v l_v^2 \quad (\text{A.4})$$

From here on, we use $l_v = 1$ to facilitate the calculation. Equalizing expression A.3 and A.4, and applying A.2, we obtain a relationship between β_1 , n_v , and h :

$$\tan(2\beta_1) = \frac{h^2}{n_v} \quad \text{or} \quad 2\beta_1 = \arctan\left(\frac{h^2}{n_v}\right) \quad (\text{A.5})$$

If h is a natural number, its value is equal to the number of horizontal layers n_l required to build an isosceles triangle. n_l can be estimated as long as we know A_v (and n_v) and β_1 .

Now, we must calculate the number of voxels per layer, which is related to the length of a layer. Notice that if we subtract the length values of two contiguous layers, the result must be $2/\tan(2\beta_1)$. With that information, we propose an expression to calculate the number of voxels $n_{v,i}$ for a specific layer i ($i = 0, \dots, n_l$):

$$n_{v,i} = n_{v,0} - \frac{2i}{\tan(2\beta_1)}, \quad \text{where } i = 0, 1, 2, \dots, n_l - 1 \quad (\text{A.6})$$

We consider that the layer at the bottom is layer 0 and is the largest one. Adding

the voxels of each layer we must obtain n_v as a result:

$$\sum_{i=0}^{n_l-1} n_{v,i} = n_v = n_{v,0} n_l - \frac{n_l(n_l - 1)}{\tan(2\beta_1)} \quad (\text{A.7})$$

Using Equations A.5 (with $h = n_l$) and A.7, we can calculate the number of voxels at the bottom layer:

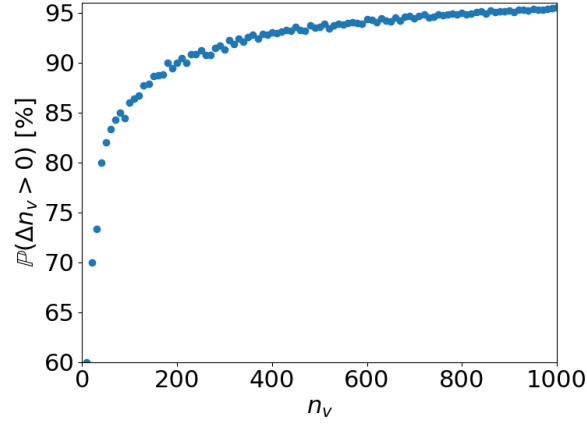
$$n_{v,0} = \frac{n_v}{n_l} \left(1 + \frac{n_l - 1}{n_l} \right) \quad (\text{A.8})$$

Equations A.8 and A.6 cannot be used to calculate natural values for $n_{v,i}$. And rounding the results does not ensure that $\sum n_{v,i} = n_v$. So it is necessary to rectify those values. Our correction considers that, when determining the number of voxels in a layer, the number of voxels from the previous layers are taken into account, its value is equal or lower than the value of the last layer and is different from zero. The final results are stored in a new variable, \mathbf{s} , which is called a “structure vector”, and $\mathbf{s}[\mathbf{i}] \in \mathbb{N}$ is the number of voxels of the layer i . The algorithm is given below:

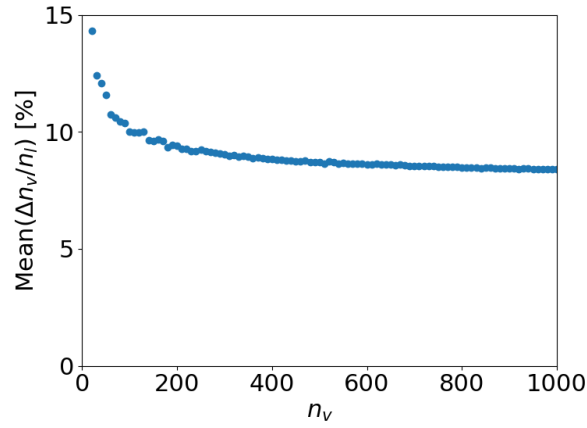
1. Do $\mathbf{s}[0] = \text{round}(n_{v,0})$;
2. set $j = 1$;
3. calculate $\mathbf{s}[j]$ using Equation A.9;
4. if $j < n_l - 1$, do $j = j + 1$ and return to step 3;
5. if $j = n_l - 1$, do $\mathbf{s}[n_l - 1] = \max(n_v - \sum_{i=0}^{n_l-2} \mathbf{s}[i], 1)$ and end loop.

$$\mathbf{s}[j] = \max(\min(\mathbf{s}[j - 1], \text{round}(\sum_{i=0}^j n_{v,i} - \sum_{i=0}^{j-1} \mathbf{s}[i])), 1) \quad (\text{A.9})$$

We utilized this algorithm to build triangles with an area from $10l_c^2$ to $1000l_c^2$, using pixels with area equal to l_c^2 ; and notice that some triangles have more pixels than expected ($\sum_{i=0}^{n_l} \mathbf{s}[i] - n_v = \Delta n_v > 0$). Figure A.2a shows the percentage of triangles with that problem. We observe that, the larger n_v is, the higher $\mathbb{P}(\Delta n_v > 0)$



(a)



(b)

Figure A.2: Results of building isosceles triangles with voxels before correct number of voxels used. (a) The probability to obtain more voxels than expected and (b) the average ratio $\Delta n_v/n_l$ are shown.

is, being \mathbb{P} the probability function. However, the excess voxels end up being less than 10% of the number of layers, as shown in Figure A.2b.

Thus, an additional procedure to remove the undesired pixels was applied. This procedure is for $j = n_l - 1, n_l - 2, \dots, 2, 1$, if $\mathbf{s}[j] > 1$, then $\mathbf{s}[j] = \mathbf{s}[j] - 1$ and evaluate the next value of j . This is done until reach the condition $\sum_{i=0}^{n_l-1} \mathbf{s}[i] = n_v$. The procedure steps are:

1. set $j = n_l - 1$;
2. if $\mathbf{s}[j] > 1$, then $\mathbf{s}[j] = \mathbf{s}[j] - 1$;
3. update Δn_v ;

4. if $\Delta n_v > 0$, do $j = j - 1$ and return to step 2;
5. if $\Delta n_v = 0$, end loop.

A.2 Calculation of the minimum shape factor

The isosceles triangle with G_{min} is a triangle with area A that, when represented by pixels ($A = n_v$, assuming pixel edge length equal to 1), its perimeter includes all pixels, that is $P_{ps} = n_v$. This perimeter depends on the number of horizontal layers n_l . If n_l is increased or reduced by one unit, P_{ps} changes. For that reason, the extreme cases for throats with $n_v \geq 30$ were evaluated. This means that n_l is very low or very high.

From Figure A.1a, we can obtain an expression for G :

$$G = \frac{A}{P^2} = \frac{a_1^2 \sin(2\beta_1) \cos(2\beta_1)}{(2a_1 + 2a_1 \cos(2\beta_1))^2} = \frac{1}{4} \frac{\tan(2\beta_1) \cos^2(2\beta_1)}{(1 + \cos(2\beta_1))^2} \quad (\text{A.10})$$

or using Equation A.5 ($h = n_l$):

$$G = \frac{n_l^2}{4n_v} \frac{\cos^2(2\beta_1)}{(1 + \cos(2\beta_1))^2} \quad (\text{A.11})$$

Evaluating the lowest values of n_l , $P_{ps} = n_v$ is obtained if $n_l = 1$ or 2. And if $n_l = 3$, $P_{ps} < n_v$ (see Figure A.3a). For $n_l = 3$, $2\beta_1 \rightarrow 0$ when $n_v \rightarrow \infty$ and we can assume that $\cos(2\beta_1) \approx 1$ for large n_v . Replacing this result in Equation A.11, we have:

$$G \approx \frac{n_l^2}{16n_v} = \frac{9}{16n_v} \quad (\text{A.12})$$

The analysis for the highest values of n_l cannot use specific values for n_l using the same reasoning as in the previous case. So we must return to the procedure of building triangles with pixels. If all the layers of a triangle have less than 3 voxels, we always satisfy the condition $P_{ps} = n_v$. If a triangle has one or two layers with 3 voxels, we still have $P_{ps} = n_v$. However, considering a third layer with 3 voxels

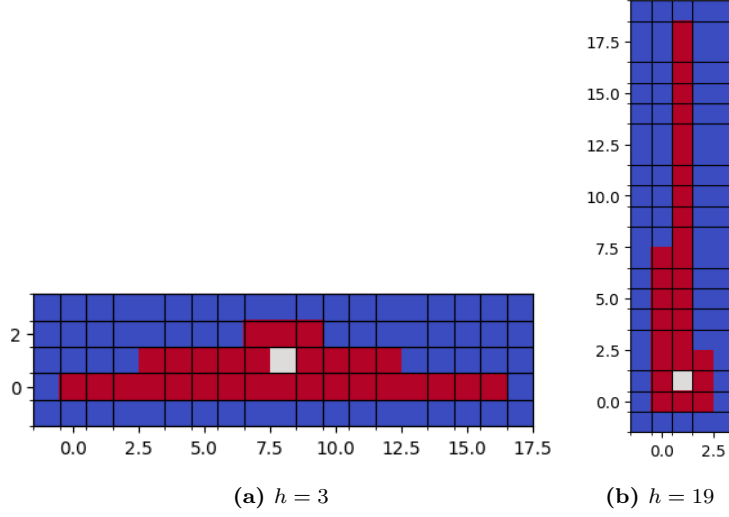


Figure A.3: G_{min} analysis for $v = 30$, where only one voxel (in gray) of the triangle is “protected” by “perimeter” voxels (in red).

leads to $P_{ps} < n_v$ (see Figure A.3b).

To obtain the value of n_l in these cases, the method used to obtain $n_{v,i}$ for $i = 2$ must be analyzed according to Equation A.9, in which the maximum and minimum operators can be disregarded. To reach at least three voxels in the third layer, it is necessary that:

$$\sum_{i=0}^2 n_{v,i} - \sum_{i=0}^1 s[i] \geq 2.5 \quad (\text{A.13})$$

where $n_{v,i}$ is calculated using Equations A.6 and A.8 with $s[0] = s[1] = 3$. Then, it is possible to employ equation A.13 to find a relationship between n_v and n_l .

$$\begin{aligned} 2.5 &\leq n_{v,0} + n_{v,1} + n_{v,2} - s[0] - s[1] \\ 2.5 &\leq 3n_{v,0} - \frac{6}{\tan(2\beta_1)} - 6 \\ 8.5 &\leq \frac{3n_v}{n_l} \left(1 + \frac{n_l - 1}{n_l} \right) - \frac{6n_v}{n_l^2} \\ 0 &\geq 8.5n_l^2 - 6n_v n_l + 9n_v \\ 0 &\geq n_l^2 - \frac{12n_v}{17}n_l + \frac{18n_v}{17} \end{aligned} \quad (\text{A.14})$$

where the roots for that quadratic expression are:

$$n_l = \frac{6n_v \pm \sqrt{36n_v^2 - 306n_v}}{17} \quad (\text{A.15})$$

The root with the lowest value can be expressed as:

$$\frac{6n_v - \sqrt{36n_v^2 - 306n_v}}{17} = \frac{306n_v}{17(6n_v + \sqrt{36n_v^2 - 306n_v})} = \frac{3}{1 + \sqrt{1 - 8.5n_v^{-1}}} \quad (\text{A.16})$$

For larger values of n_v , $n_l \rightarrow 1.5$. For that reason this root is discarded.

Evaluating the root with the largest value:

$$n_l = \frac{6n_v}{17}(1 + \sqrt{1 - 8.5n_v^{-1}}) \quad (\text{A.17})$$

Using this information on Equation A.5:

$$\begin{aligned} \tan(2\beta_1) &= \frac{n_l^2}{n_v} \\ &= \frac{36n_v}{289} \left[2(1 + \sqrt{1 - 8.5n_v^{-1}}) - 8.5n_v^{-1} \right] \\ &= \frac{144n_v}{289} (0.5 - 2.125n_v^{-1} + \sqrt{0.25 - 2.125n_v^{-1}}) \end{aligned} \quad (\text{A.18})$$

Expressing Equation A.11 in terms of $\tan(2\beta_1)$

$$\begin{aligned} G &= \frac{1 \sin(2\beta_1) \cos(2\beta_1)}{4 (1 + \cos(2\beta_1))^2} \\ &= \frac{\tan(2\beta_1)}{4(\sqrt{\tan^2(2\beta_1) + 1} + 1)^2} \\ &= \frac{1}{4 \tan(2\beta_1)} \left(\sqrt{1 + \frac{1}{\tan^2(2\beta_1)}} + \frac{1}{\tan(2\beta_1)} \right)^{-2} \end{aligned} \quad (\text{A.19})$$

Substituting Equation A.18 into A.19 to calculate G_{min} and simplifying, we have:

$$G_{min} = \frac{289}{576n_v} F_G \quad (\text{A.20})$$

where F_G is a correction factor equal to:

$$F_G = \left(\sqrt{\Gamma + \frac{83521}{20736n_v^2\Gamma}} + \frac{289}{144n_v\sqrt{\Gamma}} \right)^{-2} \quad (\text{A.21})$$

where $\Gamma = 0.5 - 2.125n_v^{-1} + \sqrt{0.25 - 2.125n_v^{-1}}$.

It is possible to observe that for $n_v \rightarrow \infty$, the value of F_G converges to 1. If we evaluate n_v between 30 and 100, the furthest value of F_G from 1 was 1.00327, for $v = 39$. This means that if $F_G = 1$, the calculated G_{min} has a maximum relative error of 0.327%, so it can be neglected. Therefore, we used $G_{min} = 289/(576v)$ as the value used for the power correlation.

A.3 Calculation of the half-corner angles for an isosceles triangle

Following [PATZEK and SILIN \(2001\)](#), the interval of values for β_2 , considering that $0 < \beta_1 \leq \beta_2 \leq \beta_3 < \pi/2$, is defined by G . Also $\beta_1 + \beta_2 + \beta_3 = \pi/2$. Figure [A.4](#) shows the geometry of a triangle. The length of the side a and the area A_{ij} of the two internal triangles shown in Fig. [A.4](#) can be expressed as:

$$a = R(\cot \beta_i + \cot \beta_j) \quad (\text{A.22})$$

$$A_{ij} = \frac{1}{2}R^2(\cot \beta_i + \cot \beta_j) \quad (\text{A.23})$$

where β_i, β_j are the half-corner angles adjacent to a and R is the radius of the inscribed circle. Applying that idea to the other sides, expressions for A and P are obtained:

$$A = R^2 \sum_{i=1}^3 \cot \beta_i \quad (\text{A.24})$$

$$P = 2R \sum_{i=1}^3 \cot \beta_i \quad (\text{A.25})$$

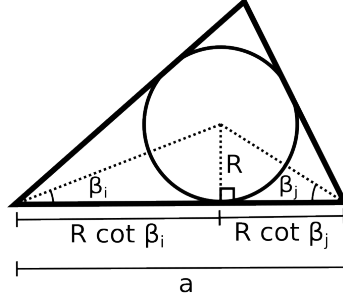


Figure A.4: Geometry of a triangle with an inscribed circle of radius R .

Then, G is expressed as:

$$G = \frac{A}{P^2} = \frac{R^2 \sum_i^3 \cot \beta_i}{(2R \sum_i^3 \cot \beta_i)^2} = \frac{1}{4 \sum_i^3 \cot \beta_i} \quad (\text{A.26})$$

Due to $\sum_{i=1}^3 \beta_i = \pi/2$, G depends only on two of the three half-corner angles.

We chose β_1 and β_2 for our demonstration, and $\beta_3 = \pi/2 - \beta_1 - \beta_2$. Then:

$$\begin{aligned} G &= \frac{1}{4} \left(\frac{1}{\tan \beta_1} + \frac{1}{\tan \beta_2} + \frac{1}{\tan \beta_3} \right)^{-1} \\ &= \frac{1}{4} \left(\frac{1}{\tan \beta_1} + \frac{1}{\tan \beta_2} + \tan(\beta_1 + \beta_2) \right)^{-1} \\ &= \frac{1}{4} \left(\frac{\tan \beta_1 + \tan \beta_2 + \tan(\beta_1 + \beta_2) \tan \beta_1 \tan \beta_2}{\tan \beta_1 \tan \beta_2} \right)^{-1} \end{aligned} \quad (\text{A.27})$$

The numerator of the fraction is equal to the expression obtained by developing the tangent addition formula:

$$\tan(\beta_1 + \beta_2) = \frac{\tan \beta_1 + \tan \beta_2}{1 - \tan \beta_1 \tan \beta_2}$$

$$\tan(\beta_1 + \beta_2)(1 - \tan \beta_1 \tan \beta_2) = \tan \beta_1 + \tan \beta_2$$

$$\tan(\beta_1 + \beta_2) - \tan(\beta_1 + \beta_2) \tan \beta_1 \tan \beta_2 = \tan \beta_1 + \tan \beta_2$$

$$\tan(\beta_1 + \beta_2) = \tan \beta_1 + \tan \beta_2 + \tan(\beta_1 + \beta_2) \tan \beta_1 \tan \beta_2 \quad (\text{A.28})$$

We use that information to simplify the expression for G :

$$G = \frac{1}{4} \tan \beta_1 \tan \beta_2 \cot(\beta_1 + \beta_2) \quad (\text{A.29})$$

That is the expression obtained by [PATZEK and SILIN \(2001\)](#). Since we use isosceles triangles, we consider either $\beta_1 = \beta_2$ or $\beta_2 = \beta_3$. For the former case, G can be expressed in terms of β_2 :

$$\begin{aligned} G &= \frac{1}{4} \tan^2 \beta_2 \frac{1}{\tan(\beta_2 + \beta_2)} \\ &= \frac{1}{4} \tan^2 \beta_2 \frac{1 - \tan^2 \beta_2}{2 \tan \beta_2} \\ &= \frac{\tan \beta_2 - \tan^3 \beta_2}{8} \end{aligned} \tag{A.30}$$

Equation [A.30](#) is also valid for the case with $\beta_2 = \beta_3$.

If $\tan \beta_2 = x$, then:

$$x^3 - x + 8G = 0 \tag{A.31}$$

which is a depressed cubic equation ($x^3 + c_1x + c_0 = 0$) with roots:

$$x_i = 2\sqrt{-\frac{c_1}{3}} \cos \left[\frac{1}{3} \arccos \left(\frac{3c_0}{2c_1} \sqrt{-\frac{3}{c_1}} \right) - \frac{2\pi i}{3} \right] \quad \text{for } i = 0, 1, 2 \tag{A.32}$$

In the cubic equation: $c_1 = -1$ and $c_0 = 8G$, so:

$$\frac{3c_0}{2c_1} \sqrt{-\frac{3}{c_1}} = \frac{3(8G)}{2(-1)} \sqrt{-\frac{3}{-1}} = -12\sqrt{3}G \tag{A.33}$$

G must be larger than 0 but smaller than the value for an equilateral triangle ($0 < G \leq \sqrt{3}/36$). Therefore:

$$-1 \leq \frac{3c_0}{2c_1} \sqrt{-\frac{3}{c_1}} < 0 \tag{A.34}$$

For the first root ($i = 0$):

$$\frac{\pi}{6} < \frac{1}{3} \arccos \left(\frac{3c_0}{2c_1} \sqrt{-\frac{3}{c_1}} \right) \leq \frac{\pi}{3} \tag{A.35}$$

$$\frac{1}{2} \leq \cos \left[\frac{1}{3} \arccos \left(\frac{3c_0}{2c_1} \sqrt{-\frac{3}{c_1}} \right) \right] < \frac{\sqrt{3}}{2} \quad (\text{A.36})$$

$$\frac{\sqrt{3}}{3} \leq x_0 < 1 \rightarrow \frac{\pi}{6} \leq \beta_2 \leq \frac{\pi}{4} \quad (\text{A.37})$$

For the second root ($i = 1$):

$$-\frac{\pi}{2} < \frac{1}{3} \arccos \left(\frac{3c_0}{2c_1} \sqrt{-\frac{3}{c_1}} \right) - \frac{2\pi}{3} \leq -\frac{\pi}{3} \quad (\text{A.38})$$

$$0 < \cos \left[\frac{1}{3} \arccos \left(\frac{3c_0}{2c_1} \sqrt{-\frac{3}{c_1}} \right) - \frac{2\pi}{3} \right] \leq \frac{1}{2} \quad (\text{A.39})$$

$$0 < x_1 \leq \frac{\sqrt{3}}{3} \rightarrow 0 < \beta_2 \leq \frac{\pi}{6} \quad (\text{A.40})$$

For the third root ($i = 2$):

$$-\frac{7\pi}{6} < \frac{1}{3} \arccos \left(\frac{3c_0}{2c_1} \sqrt{-\frac{3}{c_1}} \right) - \frac{4\pi}{3} \leq -\pi \quad (\text{A.41})$$

$$-1 \leq \cos \left[\frac{1}{3} \arccos \left(\frac{3c_0}{2c_1} \sqrt{-\frac{3}{c_1}} \right) - \frac{4\pi}{3} \right] < -\frac{\sqrt{3}}{2} \quad (\text{A.42})$$

$$\frac{-2}{\sqrt{3}} \leq x_2 < -1 \quad (\text{A.43})$$

Since $0 < \beta_2 < \pi/2$, just the first and second roots are accepted. When $i = 0$, $\pi/6 < \beta_2 \leq \pi/4$. In this case, since $2\beta_2 \rightarrow \pi/2$, this root represents an isosceles triangle with 2 large and equal corner angles that can reach the limit of $\pi/2$. Therefore, $\beta_3 = \beta_2$ and:

$$0 < \beta_1 \leq \pi/6 \leq \beta_2 = \beta_3 < \pi/4 \quad (\text{A.44})$$

When $i = 1$, $0 < \beta_2 \leq \pi/6$, this root represents an isosceles triangle with two

small corner angles that can reach the limit of zero. Thus, $\beta_1 = \beta_2$ and:

$$0 < \beta_1 = \beta_2 \leq \pi/6 \leq \beta_3 < \pi/2 \tag{A.45}$$

Appendix B

Calculating geometric properties for the equilateral triangular prismatic pores

Equation 3.23, that relates the pore properties V , S , and a is a depressed cubic equation with the form:

$$a^3 + c_1a + c_0 = 0 \quad (\text{B.1})$$

If it is true that $4c_1^3 + 27c_0^2 < 0$, then the equation has three different real roots. Since $c_1 = -2S/\sqrt{3}$ and $c_0 = 8V$, we have:

$$4\left(-\frac{2S}{\sqrt{3}}\right)^3 + 27(8V)^2 = 2^5 3^{-3/2} (3^{9/2} 2V^2 - S^3) \quad (\text{B.2})$$

Considering $S > S_{min} = 3\sqrt{3}\sqrt[3]{2V^2}$ (Equation 3.22), the expression in Eq. B.2 is always negative. Thus, Equation 3.23 always has three real roots. Those are calculated with the following equation:

$$a_i = 2\sqrt{-\frac{c_1}{3}} \cos \left[\frac{1}{3} \arccos \left(\frac{3c_0}{2c_1} \sqrt{-\frac{3}{c_1}} \right) - \frac{2\pi i}{3} \right] \quad \text{for } i = 0, 1, 2 \quad (\text{B.3})$$

To know the sign of each root, we analyze Equation B.3:

$$\frac{3c_0}{2c_1} \sqrt{-\frac{3}{c_1}} = -\frac{3^{9/4} 2^{1/2} V}{S^{3/2}} \quad (\text{B.4})$$

Again due to the range of values of S it is possible to conclude that if $S > S_{min}$:

$$-1 < \frac{3c_0}{2c_1} \sqrt{-\frac{3}{c_1}} < 0 \quad (\text{B.5})$$

For the first root ($i = 0$):

$$\frac{\pi}{6} < \frac{1}{3} \arccos \left(\frac{3c_0}{2c_1} \sqrt{-\frac{3}{c_1}} \right) < \frac{\pi}{3} \quad (\text{B.6})$$

$$\frac{1}{2} < \cos \left[\frac{1}{3} \arccos \left(\frac{3c_0}{2c_1} \sqrt{-\frac{3}{c_1}} \right) \right] < \frac{\sqrt{3}}{2} \quad (\text{B.7})$$

$$\sqrt{-\frac{c_1}{3}} < a_0 < \sqrt{-c_1} \quad (\text{B.8})$$

$$a_0 = \frac{2^{3/2} S^{1/2}}{3^{3/4}} \cos \left[\frac{1}{3} \arccos \left(-\frac{3^{9/4} 2^{1/2} V}{S^{3/2}} \right) \right] \quad (\text{B.9})$$

For the second root ($i = 1$):

$$-\frac{\pi}{2} < \frac{1}{3} \arccos \left(\frac{3c_0}{2c_1} \sqrt{-\frac{3}{c_1}} \right) - \frac{2\pi}{3} < -\frac{\pi}{3} \quad (\text{B.10})$$

$$0 < \cos \left[\frac{1}{3} \arccos \left(\frac{3c_0}{2c_1} \sqrt{-\frac{3}{c_1}} \right) - \frac{2\pi}{3} \right] < \frac{1}{2} \quad (\text{B.11})$$

$$0 < a_1 < \sqrt{-\frac{c_1}{3}} \quad (\text{B.12})$$

$$a_1 = \frac{2^{3/2} S^{1/2}}{3^{3/4}} \cos \left[\frac{1}{3} \arccos \left(-\frac{3^{9/4} 2^{1/2} V}{S^{3/2}} \right) - \frac{2\pi}{3} \right] \quad (\text{B.13})$$

For the third root ($i = 2$):

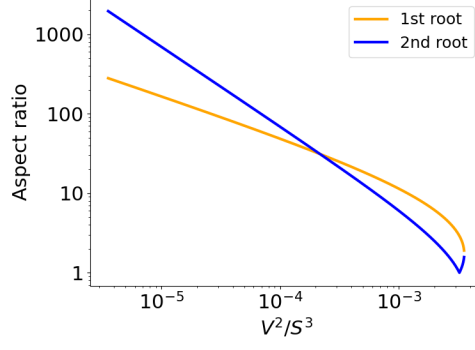


Figure B.1: Aspect ratio for triangular prisms with volume V and superficial area S . The roots are related to the possible values of the edge side a , calculated with Equation B.3

$$-\frac{7\pi}{6} < \frac{1}{3} \arccos \left(\frac{3c_0}{2c_1} \sqrt{-\frac{3}{c_1}} \right) - \frac{4\pi}{3} < -\pi \quad (\text{B.14})$$

$$-1 < \cos \left[\frac{1}{3} \arccos \left(\frac{3c_0}{2c_1} \sqrt{-\frac{3}{c_1}} \right) - \frac{4\pi}{3} \right] < -\frac{\sqrt{3}}{2} \quad (\text{B.15})$$

$$-2\sqrt{-\frac{c_1}{3}} < a_2 < -\sqrt{-c_1} \quad (\text{B.16})$$

$$a_2 = \frac{2^{3/2} S^{1/2}}{3^{3/4}} \cos \left[\frac{1}{3} \arccos \left(-\frac{3^{9/4} 2^{1/2} V}{S^{3/2}} \right) - \frac{4\pi}{3} \right] \quad (\text{B.17})$$

From Equation B.16, a_2 is negative, so it is not taken into account. From Equations B.8 and B.12, we can see that $a_0 \geq a_1$, and, therefore, from Equation 3.17 $h_0 \leq h_1$. Figure B.1 shows the results of the aspect ratio (Equation 3.24) for a prism with an adimensional ratio V^2/S^3 . Notice that the results just depend on V^2/S^3 , independent of the values of V and S .

Appendix C

Defining properties to create networks

C.1 Defining pore diameters using a truncated log-normal distribution

Since we consider a lognormal distribution to be the best fit for the pore equivalent diameter, we imposed its cumulative distribution by using random numbers between 0 and 1 and mapping them to corresponding diameter values. Since the distribution is truncated to cover only the range between $D_{p,min}$ and $D_{p,max}$, care is needed for its imposition. The expression for the cumulative distribution for a lognormal distribution of a random variable x is:

$$\mathbb{F}(x, m, \sigma) = \int_0^x \mathbb{P}(x) = \frac{1}{2} \operatorname{erfc} \left(-\frac{\ln(x) - m}{\sigma\sqrt{2}} \right) \quad (\text{C.1})$$

where m and σ is the mean and the standard deviation of the underlying normal distribution (in log scale) respectively, \mathbb{P} is the distribution, and $\operatorname{erfc}(z)$ is the complementary error function defined as:

$$\operatorname{erfc}(z) = 1 - \operatorname{erf}(z) = 1 - \frac{2}{\sqrt{\pi}} \int_0^z e^{-t^2} dt \quad (\text{C.2})$$

Expressions for m and σ can be obtained from the mean and the standard deviation of x in the original scale, which are represented by \bar{x} and σ_x respectively:

$$m = \ln \left(\frac{\bar{x}^2}{\sqrt{\bar{x}^2 + \sigma_x^2}} \right) \quad (C.3)$$

$$\sigma = \sqrt{\ln \left(1 + \left(\frac{\sigma_x}{\bar{x}} \right)^2 \right)} \quad (C.4)$$

The probability that x is higher than x_{min} and lower than x_{max} is represented by W_1 and can be expressed using the cumulative relative frequency function:

$$\begin{aligned} W_1 &= \int_{x_{min}}^{x_{max}} \mathbb{P}(x, m, \sigma) dx \\ &= \int_0^{x_{max}} \mathbb{P}(x, m, \sigma) dx - \int_{x_{max}}^{x_{min}} \mathbb{P}(x, m, \sigma) dx \\ &= \mathbb{F}(x_{max}, m, \sigma) - \mathbb{F}(x_{min}, m, \sigma) \end{aligned} \quad (C.5)$$

Now, for a truncated lognormal distribution, the relative frequency is defined as:

$$\mathbb{P}^T(x; m, \sigma) = \begin{cases} 0 & , \text{ if } x < x_{min} \text{ or } x > x_{max} \\ W_1^{-1} \mathbb{P}(x, m, \sigma) & , \text{ if } x_{min} \leq x \leq x_{max} \end{cases} \quad (C.6)$$

Then, its cumulative relative frequency for a value x within the range $[x_{min}, x_{max}]$ is given by:

$$\mathbb{F}^T(x; m, \sigma) = \int_{0^+}^x \mathbb{P}^T(x, m, \sigma) dx = \int_{x_{min}}^x \mathbb{P}^T(x, m, \sigma) dx \quad (C.7)$$

We can rewrite the expression for \mathbb{F}^T as follows:

$$\begin{aligned} \mathbb{F}^T(x; m, \sigma) &= \int_{x_{min}}^x W_1^{-1} \mathbb{P}(x, \mu, \sigma) dx \\ &= W_1^{-1} \left[\int_{0^+}^x \mathbb{P}(x, \mu, \sigma) dx - \int_{0^+}^{x_{min}} \mathbb{P}(x, \mu, \sigma) dx \right] \\ &= W_1^{-1} [\mathbb{F}_{rel}(x; m, \sigma) - \mathbb{F}_{rel}(x_{min}; m, \sigma)] \\ &= \frac{\mathbb{F}_{rel}(x; m, \sigma) - \mathbb{F}_{rel}(x_{min}; m, \sigma)}{\mathbb{F}(x_{max}, m, \sigma) - \mathbb{F}(x_{min}, m, \sigma)} \end{aligned} \quad (C.8)$$

Our objective is to express x in terms of $F^T(x)$, so we rewrite the expression in Eq. C.8 using Eq. C.1 and introducing W_2 as:

$$W_2 = \mathbb{F}(x_{min}; m, \sigma) / W_1 \quad (\text{C.9})$$

for simplification. Also, for simplification too, we use $\mathbb{F}^T(x)$ instead of $\mathbb{F}^T(x; \mu, \sigma)$:

$$\begin{aligned} \mathbb{F}^T(x) &= \frac{1}{2W_1} \operatorname{erfc} \left(-\frac{\ln(x) - \mu}{\sigma\sqrt{2}} \right) - W_2 \\ 2W_1(\mathbb{F}^T(x) + W_2) &= \operatorname{erfc} \left(-\frac{\ln(x) - \mu}{\sigma\sqrt{2}} \right) \\ \frac{\ln(x) - m}{\sigma\sqrt{2}} &= -\operatorname{erfc}^{-1} (2W_1(\mathbb{F}^T(x) + W_2)) \\ \ln(x) - m &= -\sigma\sqrt{2} \operatorname{erfc}^{-1} (2W_1(\mathbb{F}^T(x) + W_2)) \\ \ln(x) &= -\sigma\sqrt{2} \operatorname{erfc}^{-1} (2W_1(\mathbb{F}^T(x) + W_2)) + m \\ x &= \exp \left[-\sigma\sqrt{2} \operatorname{erfc}^{-1} (2W_1(\mathbb{F}^T(x) + W_2)) + m \right] \end{aligned} \quad (\text{C.10})$$

Therefore, we have a method to define $D_{eq,p}$ for a pore, having as information $\bar{D}_{eq,p}$, σ_D , $D_{p,min}$, and $D_{p,max}$: First we calculate m (Eq. C.3), σ (Eq. C.4), W_1 (Eq. C.5), and W_2 (Eq. C.9); then we choose a random number between 0 and 1, which is the value for $F^T(D_{eq,p})$; and finally we calculate $D_{eq,p}$ using the final expression from Eq. C.10, replacing x with $D_{eq,p}$.

C.2 Avoiding pore overlapping in imposing pore diameter distribution

If $\lambda \leq D_{p,max}$, we can generate overlapping pores. The condition for two connected pores with equivalent diameters D_{p1} and D_{p2} to overlap is $(D_{p1} + D_{p2})/2 > \lambda$. To avoid this, we propose the following algorithm:

1. define the number of pores N_p ;

2. construct a vector which contains N_p random values between 0 and 1, representing the $\mathbb{F}^T(D_{eq,p})$ values;
3. with this vector, calculate the corresponding $D_{eq,p}$ vector according to the information in Appendix C.1, which we represent as \mathbf{D} ;
4. construct another vector with N_p elements consisting of natural numbers from 0 to $N_p - 1$, arranged randomly, which we represent as \mathbf{p} ;
5. set $i = 0$;
6. for the pore in position $\mathbf{p}[i]$ select as $D_{eq,p}$ the highest value in \mathbf{D} the satisfies the condition to avoid overlapping and remove it from \mathbf{D} ,
7. if $i < N_p - 1$, make $i = i + 1$ and return to Step 6. If not, end the process.

This algorithm does not guarantee avoiding overlapping, as it relies on random values for the pore equivalent diameter. The probability of success increases with higher values of λ . Also, since we work with networks containing thousands of pores, we must consider that it is very likely that at least one of them has a diameter close to $D_{p,max}$. If $\lambda < (D_{p,min} + D_{p,max})/2$, there is no chance to avoid overlapping for that pore. For that reason, we recommend to work with a λ that satisfies the condition $\lambda > (D_{p,min} + D_{p,max})/2$. In our particular case, with $D_{p,min} = 24.59 \mu\text{m}$ and $D_{p,max} = 266.69 \mu\text{m}$, λ must be higher than $145.64 \mu\text{m}$.

Appendix D

Calculation of entry capillary pressures

D.1 Analysis of the PLD in a throat

D.1.1 Primary drainage

The expressions for A_{nw} , L_{nw-w} , and L_{nw-s} given by Equations 3.31, 3.33 and 3.35 are demonstrated below. These values are expressed in terms of the half-contact angles β_i , the inscribed radius R , the radius of curvature of the interface for a drainage process r_d , and the shape factor G of the cross section. Figure D.1 shows the geometry of a corner that keeps the wetting phase after the invasion of the non-wetting phase.

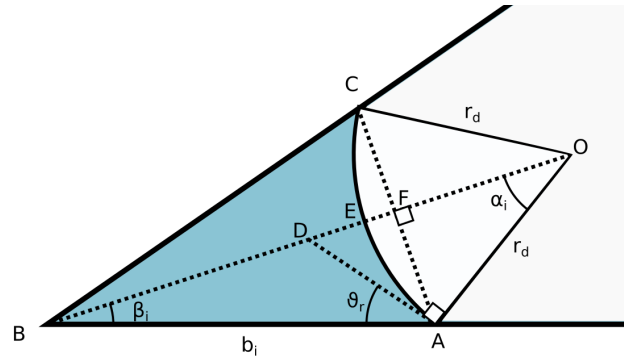


Figure D.1: Reproduction of Figure 3.5c

L_{nw-w} is the sum of all fluid-fluid interface lengths. In Figure D.1, the interface is the arc \widehat{AEC} , equal to $2r_d\alpha_i$. But α_i can be expressed in terms of β_i and θ_r :

$$\alpha_i + \frac{\pi}{2} + \theta_r + \beta_i = \pi \quad \rightarrow \quad \alpha_i = \frac{\pi}{2} - (\theta_r + \beta_i) \quad (\text{D.1})$$

Then, the interface \widehat{AEC} is:

$$\widehat{AEC} = 2r_d\alpha_i = 2r_d\left(\frac{\pi}{2} - \theta_r - \beta_i\right) \quad (\text{D.2})$$

The summation of all interfaces gives Equation 3.35, which is the expression to calculate L_{nw-w} .

The expressions for L_{nw-s} and A_{nw} requires the calculation of some segments that appear in Figure D.1 in terms of r_d , θ_r , and β_i :

$$\overline{OF} = r_d \cos \alpha_i = r_d \sin(\theta_r + \beta_i) \quad (\text{D.3})$$

$$\overline{FA} = r_d \sin \alpha_i = r_d \cos(\theta_r + \beta_i) \quad (\text{D.4})$$

$$\overline{FB} = \overline{FA} \cot \beta_i = r_d \cos(\theta_r + \beta_i) \cot \beta_i \quad (\text{D.5})$$

$$\overline{AB} = b_i = \overline{FA} \csc \beta_i = r_d \cos(\theta_r + \beta_i) \csc \beta_i \quad (\text{D.6})$$

To obtain L_{nw-s} , we subtract the solid-wetting phase interface lengths from the cross-sectional perimeter. In Figure D.1, the interface solid-wetting phase is $2\overline{AB}$. And, from Eqs. A.24, A.25, and A.26, $P = R/(2G)$. These two pieces of information are used to get the expression in Equation 3.33.

To obtain A_{nw} , we subtract the area occupied by the wetting phase from the cross-sectional area:

$$A_{nw} = A - \sum_{i=1}^3 A_{co}(\beta_i) \quad (\text{D.7})$$

where $A_{co}(\beta_i)$ is the area occupied by the wetting phase in the corner with half angle β_i . From Eqs. A.24, A.25, and A.26, we have:

$$A = 0.5RP = \frac{R^2}{4G} \quad (\text{D.8})$$

$A_{co}(\beta_i)$ is calculated by doubling the area of the section AEB , which is calculated as follows:

$$\begin{aligned} AEB &= OBA - AOE \\ &= \frac{\overline{FA}(\overline{OF} + \overline{FB})}{2} - \frac{r_d^2 \alpha_i}{2} \\ &= \frac{r_d^2}{2} \cos(\theta_r + \beta_i) [\sin(\theta_r + \beta_i) + \cos(\theta_r + \beta_i) \cot \beta_i] - \frac{r_d^2}{2} \left[\frac{\pi}{2} - (\theta_r + \beta_i) \right] \\ &= \frac{r_d^2}{2} \left[\cos(\theta_r + \beta_i) \left[\frac{\sin(\theta_r + \beta_i) \sin \beta_i + \cos(\theta_r + \beta_i) \cos \beta_i}{\sin \beta_i} \right] + \theta_r + \beta_i - \frac{\pi}{2} \right] \\ &= \frac{r_d^2}{2} \left[\frac{\cos(\theta_r + \beta_i) \cos \theta_r}{\sin \beta_i} + \theta_r + \beta_i - \frac{\pi}{2} \right] \end{aligned} \quad (\text{D.9})$$

Then:

$$A_{co}(\beta_i) = 2AEB = r_d^2 \left[\frac{\cos(\theta_r + \beta_i) \cos \theta_r}{\sin \beta_i} + \theta_r + \beta_i - \frac{\pi}{2} \right] \quad (\text{D.10})$$

Substitutions of Equations D.10 and D.8 into Equation D.7 leads to the expression of A_{nw} in Equation 3.31.

Now we can substitute Equations 3.31, 3.33, and 3.35 into Eq. 3.30 and use the definition $\Psi_4 = \Psi_1 - 2\Psi_2 \cos \theta_r + \Psi_3$, to obtain an expression for r_d :

$$\begin{aligned}
A_{nw} &= r_d(L_{nw-w} + L_{nw-s} \cos \theta_r) \\
\frac{R^2}{4G} - r_d^2 \Psi_1 &= r_d \left[(r_d \Psi_3) + \left(\frac{R}{2G} - 2r_d \Psi_2 \right) \cos \theta_r \right] \\
0 &= r_d^2 (\Psi_1 - 2\Psi_2 \cos \theta_r + \Psi_3) + r_d \frac{R}{2G} \cos \theta_r - \frac{R^2}{4G} \\
0 &= r_d^2 \Psi_4 + r_d \frac{R}{2G} \cos \theta_r - \frac{R^2}{4G}
\end{aligned} \tag{D.11}$$

If the roots of the quadratic equation are calculated, we have:

$$\begin{aligned}
r_d &= \frac{-R \cos \theta_r / (2G) \pm \sqrt{(R \cos \theta_r / 2G)^2 + 4\Psi_4 R^2 / (4G)}}{2\Psi_4} \\
r_d &= \frac{R \cos \theta_r}{4G\Psi_4} \left(-1 \pm \sqrt{1 + \frac{4G\Psi_4}{\cos^2 \theta_r}} \right)
\end{aligned} \tag{D.12}$$

Since r_d must be positive, we have:

$$\begin{aligned}
r_d &= \frac{R \cos \theta_r}{4G\Psi_4} \left(-1 + \sqrt{1 + \frac{4G\Psi_4}{\cos^2 \theta_r}} \right) \left(1 + \sqrt{1 + \frac{4G\Psi_4}{\cos^2 \theta_r}} \right) \left(1 + \sqrt{1 + \frac{4G\Psi_4}{\cos^2 \theta_r}} \right)^{-1} \\
r_d &= \frac{R \cos \theta_r}{4G\Psi_4} \left(-1 + 1 + \frac{4G\Psi_4}{\cos^2 \theta_r} \right) \left(1 + \sqrt{1 + \frac{4G\Psi_4}{\cos^2 \theta_r}} \right)^{-1} \\
r_d &= \frac{R}{\cos \theta_r} \left(1 + \sqrt{1 + \frac{4G\Psi_4}{\cos^2 \theta_r}} \right)^{-1}
\end{aligned} \tag{D.13}$$

By substituting this expression for r_d in Equation 3.30, it is possible to arrive at Equation 3.37 in order to calculate p_c^e .

D.1.2 Spontaneous imbibition process

The analysis for a spontaneous imbibition process is similar to the analysis for primary drainage, replacing θ_r by θ_h or θ_a , and r_d by r_{imb} .

Since b_i is sometimes constant, it is better to express L_{nw-s} and L_{nw-w} as functions of b_i . Thus, for the sum of the solid-wetting phase interface lengths, we have $L_{nw-s} = P - 2 \sum_{i=1}^3 b_i$. Also, Equations D.4 with r_{imb} in the place of r_d allows to write:

$$\overline{FA} = r_{imb} \sin \alpha_i = b_i \sin(\beta_i) \quad (\text{D.14})$$

Using Eq. D.2 with r_{imb} , we can write:

$$L_{nw-w} = \sum_{i=1}^n 2r_{imb} \alpha_i = \sum_{i=1}^n 2r_{imb} \arcsin \left[\frac{b_i \sin \beta_i}{r_{imb}} \right] \quad (\text{D.15})$$

Notice that, during an imbibition process, either the contact angle $\theta_{h,i}$ or the AM distance to the corner, b_i , can be changing, which may be different for each corner. For that reason, the analytical demonstration of the expression for r_d done in Appendix D.1.1 can not be used to calculate r_{imb} , and an iteration process must be done.

The maximum value of θ_a that allows a spontaneous imbibition process ($p_c^e > 0$) $\theta_{a,max}$ is obtained for the limiting condition $p_c^e = 0$. If we replace that value on Equation 3.43:

$$L_{nw-w} + L_{nw-s} \cos \theta_{a,max} = 0 \quad (\text{D.16})$$

This pressure condition means that $r_{imb} \rightarrow \infty$, so in Figure D.1 the arc \widehat{AEC} is exactly the same as the line \overline{AFC} , being equal to $2b_i \sin \beta_i$. As b_i remains invariant until θ_h reaches θ_a , we can recalculate L_{nw-w} using Equation D.14 and the expression for b_i provided by Equation 3.39:

$$L_{nw-w} = 2 \sum_{i=1}^n b_i \sin \beta_i = 2 \frac{\sigma}{p_{c,max}} \sum_{i=1}^n \cos(\theta_r + \beta_i) \quad (\text{D.17})$$

To calculate L_{nw-s} , we replace the expression for b_i in Equation 3.46:

$$\begin{aligned}
L_{nw-s} &= \frac{R}{2G} - 2 \sum_{i=1}^n b_i \\
&= \frac{R}{2G} - 2 \sum_{i=1}^n \left(\frac{\sigma}{p_{c,max}} \frac{\cos(\theta_r + \beta_i)}{\sin \beta_i} \right) \\
&= \frac{R}{2G} - 2 \frac{\sigma}{p_{c,max}} \sum_{i=1}^n \left(\frac{\cos \theta_r \cos \beta_i - \sin \theta_r \sin \beta_i}{\sin \beta_i} \right) \\
&= \frac{R}{2G} - 2 \frac{\sigma}{p_{c,max}} \sum_{i=1}^n (\cos \theta_r \cot \beta_i - \sin \theta_r) \\
&= \frac{\sigma}{2p_{c,max}G} \left[\frac{Rp_{c,max}}{\sigma} - 4G \left(\cos \theta_r \sum_{i=1}^n \cot \beta_i - n \sin \theta_r \right) \right]
\end{aligned} \tag{D.18}$$

Combining Equations [D.16](#), [D.17](#) and [D.18](#):

$$\begin{aligned}
\cos \theta_{a,max} &= - \frac{L_{nw-w}}{L_{nw-s}} \\
&= - \frac{2 \frac{\sigma}{p_{c,max}} \sum_{i=1}^n \cos(\theta_r + \beta_i)}{\frac{\sigma}{2p_{c,max}G} \left[\frac{Rp_{c,max}}{\sigma} - 4G (\cos \theta_r \sum_{i=1}^n \cot \beta_i - n \sin \theta_r) \right]} \\
&= - \frac{-4G \sum_{i=1}^n \cos(\theta_r + \beta_i)}{Rp_{c,max}/\sigma - 4G (\cos \theta_r \sum_{i=1}^n \cot \beta_i - n \sin \theta_r)}
\end{aligned} \tag{D.19}$$

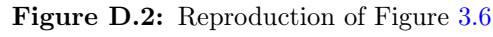
which is Equation [3.48](#).

D.1.3 Forced imbibition process

When $p_c < 0$, the interface curvature is inverted. Figure [D.2](#) shows the interface direction at this condition.

We can use the same expressions for L_{nw-s} and L_{nw-w} obtained for the spontaneous imbibition (Eqs. [3.46](#) and [3.47](#)), because these are expressed in terms of b_i . For A_{nw} , we evaluate how the inversion of the interface curvature modifies Equation [3.45](#).

From Figure [D.2](#), the relation between β_i , θ_h and α is:



The expressions to calculate the lengths of the segments \overline{OF} , \overline{FA} , and \overline{FB} are:

$$\overline{FA} = r_{imb} \sin \alpha_i = -r_{imb} \cos(\theta_h + \beta_i) \quad (\text{D.22})$$

If these equations were compared to those in Appendix D.1.1, the only difference is the sign in the expressions of \overline{FA} and \overline{FB} . Calculating A_{co} :

Eq. D.24 gives the same expression for A_{co} on a spontaneous imbibition invasion.

For that reason, Equation 3.45 can still be used.

D.2 Analysis for snap-off in spontaneous imbibition

The first AM to move is the one located at the sharpest corner. This is proved if we find a relation between β and the required p_c for a contact angle of an AM to achieve the value of θ_a . For that, we compute the partial derivative of $p_c(\theta_a)/p_{c,max}$ with respect of β , using Equation 3.42:

$$\frac{\partial}{\partial \beta} \left(\frac{p_c(\theta_a)}{p_{c,max}} \right) = \frac{\cos(\theta_a + \beta) \sin(\theta_r + \beta)}{\cos^2(\theta_r + \beta)} - \frac{\sin(\theta_a + \beta)}{\cos(\theta_r + \beta)} = \frac{\sin(\theta_r - \theta_a)}{\cos^2(\theta_r + \beta)} \quad (\text{D.25})$$

The partial derivative is always negative for $0 < \theta_r < \theta_a < \pi$. So, $p_c(\theta_a)$ is a decreasing function in β . For a process that reduces p_c , the first AM that starts moving is the one that has the highest value for $p_c(\theta_a)$, which is the one located on the sharpest corner.

For the analysis of the collision between AMs, we use the information from Figure D.3. Talking about spontaneous imbibition, when the AM of the sharpest corner starts to move, the other AMs are fixed. Assuming they remain fixed, we can calculate the b_1 required for collision, represented by b_1^S , by subtracting b_i from the length of the triangle side that connects the AMs that will collide:

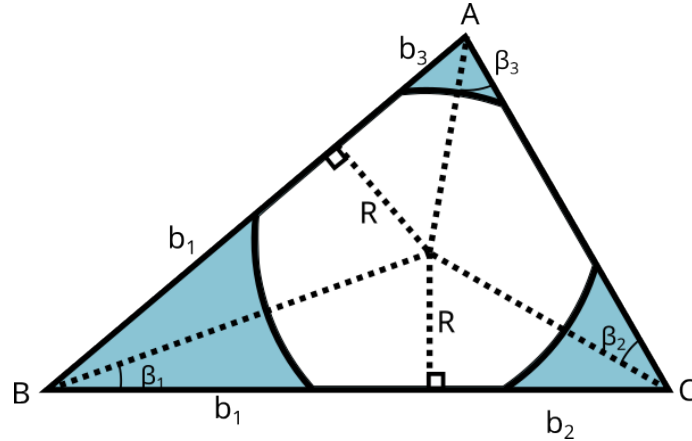


Figure D.3: Geometrical analysis of a triangular cross section after the invasion of the non-wetting phase. $0 < \beta_1 \leq \beta_2 \leq \beta_3 < \pi/2$

$$b_1^S = R(\cot \beta_1 + \cot \beta_i) - b_i \quad \text{for} \quad i = 2, 3 \quad (\text{D.26})$$

Notice that b_i does not depend on R . Using Equation 3.39 to substitute b_i on Equation D.26:

$$b_1^S = R(\cot \beta_1 + \cot \beta_i) - r_{d,min} \frac{\cos(\theta_r + \beta_i)}{\sin \beta_i} \quad (\text{D.27})$$

We have two collision options (for $i = 2, 3$) and the one that occurs is the one involving the least displacement of the AM, or the lowest b_1 . We may know which collision is preferred by differentiating b_1 with respect to β_i :

$$\frac{\partial b_1^S}{\partial \beta_i} = -\frac{R}{\sin^2 \beta_i} + \frac{r_{d,min} \cos \theta_r}{\sin^2 \beta_i} \quad (\text{D.28})$$

We do not have a direct relation between R and $r_{d,min}$. However, Equation D.13 gives a relation between R and the value for r_d required to be invaded during a primary drainage process:

$$\frac{R}{r_d \cos \theta_r} = 1 + \sqrt{1 + \frac{4G\Psi_4}{\cos^2 \theta_r}} \quad (\text{D.29})$$

Analyzing the term from the right is too complicated, mainly because Ψ_4 is calculated using different expressions that involve θ_r and the triangle geometry (see Section 3.5.2). So we decided to calculate it for different scalene triangles (algorithm to construct of scalene triangles given by PATZEK and SILIN (2001)) and many values of θ_r considering that $0 \leq \theta_r \leq \pi/2$. We find that this term is always higher than 1 (values close to 1 are found for G close to zero and $\theta_r = 0$). So:

$$R > r_d \cos \theta_r > r_{d,min} \cos \theta_r \quad (\text{D.30})$$

and:

$$\frac{R}{r_d \cos \theta_r} > 1 \quad (\text{D.31})$$

Also, the AM was formed when the element was invaded at a pressure p_c lower than or equal to the maximum capillary pressure reached during primary drainage. As the interfacial radius of curvature is inversely proportional to the capillary pressure, $r_{d,min} \leq r_d$. Then:

$$-R + r_{d,min} \cos \theta_r < 0 \quad (\text{D.32})$$

Replacing this inequality on Eq. D.28, we find that b_1^S is a decreasing function in β_i . The greater the β_i is, the shorter the distance traveled by the moving AM. That means the collision will occur with the AM with the largest β_i (β_3), which is the indicated condition for the first snap-off scenario during spontaneous imbibition. To calculate the required p_c^e we work with Equation D.26 considering that $i = 3$:

$$\overline{AB} = b_1 + b_3 = R(\cot \beta_1 + \cot \beta_3) \quad (\text{D.33})$$

As the contact angles of the AM of the corners A and B are $\theta_{h,3}$ and θ_a respectively, we use Equations 3.40 and 3.44 to replace b_1 and b_3 . Also, as we are calculating the entry capillary pressure, substitute $r_{imb} = \sigma/p_c^e$:

$$\begin{aligned} b_1 + b_3 &= \frac{\sigma}{p_c^e} \left[\frac{\cos(\theta_a + \beta_1)}{\sin \beta_1} + \frac{\cos(\theta_{h,3} + \beta_3)}{\sin \beta_3} \right] \\ &= \frac{\sigma}{p_c^e} \left[\frac{\cos \theta_a \cos \beta_1 - \sin \theta_a \sin \beta_1}{\sin \beta_1} + \frac{\cos \theta_{h,3} \cos \beta_3 - \sin \theta_{h,3} \sin \beta_3}{\sin \beta_3} \right] \quad (\text{D.34}) \\ &= \frac{\sigma}{p_c^e} (\cos \theta_a \cot \beta_1 - \sin \theta_a + \cos \theta_{h,3} \cot \beta_3 - \sin \theta_{h,3}) \end{aligned}$$

Combining Equations D.33 and D.34, it is possible to obtain p_c^e as in Equation 3.51.

When all interfaces move, as in Figure 3.10b, the calculation for collision between the displaced AMs is modified. However, the mathematical analysis is similar to the one used to demonstrate Equation 3.51. The required p_c to collide two moving AMs can be calculated using Equation 3.51, replacing θ_h with θ_a , and generalizing for β_i and β_j :

$$p_c^e = \frac{\sigma}{R} \left(\cos \theta_a - \frac{2 \sin \theta_a}{\cot \beta_i + \cot \beta_j} \right) \quad (\text{D.35})$$

The collision with the highest p_c^e is the one that occurs. That is when $\cot \beta_i + \cot \beta_j$ has its maximum value. So β_i and β_j must refer to the two sharpest corners, just as is indicated in Equation 3.52.

D.3 Analysis for layer collapse

After an invasion for an imbibition process, some corners may have a thin layer of the invaded phase sandwiched between the phases located at the center and the corner, as shown in Figure D.4. This layer is formed on a corner if the newly created fluid-fluid interface is a convex surface viewed from the corner, which occurs if:

$$\theta_a > \pi/2 + \beta_i \quad (\text{D.36})$$

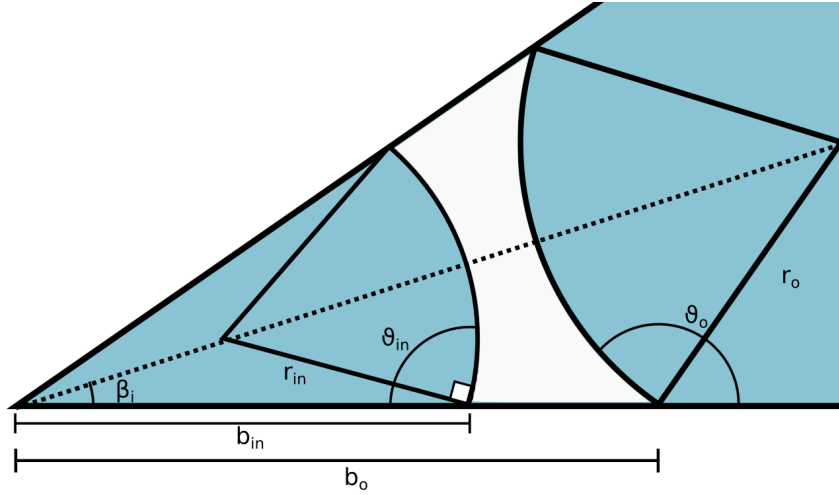


Figure D.4: Reproduction of Figure 3.20

This criterion is easily perceived by analyzing the limiting case of a planar fluid-fluid interface.

After a layer is created, we have an inner and an outer interface, which are the nearest and farthest AMs from the corner. In this situation, the inner interface has a hinging contact angle $\theta_h = \theta_{in}$ and a fixed distance to the corner b_i , and the

outer interface is moving with a constant angle equal to θ_a . This layer collapses if both interface crests collide. Thus, we can obtain analytically the distances of the crest of both interfaces to the corner. Expressions for these distances we obtained in Appendices D.1.1 and D.1.3: both are the length of \overline{EB} in Figures D.1 and D.2. For the inner interface, using Equations D.21, D.23:

$$\begin{aligned}
\overline{EB} &= \overline{FB} + \overline{OE} - \overline{OF} \\
&= r \cos(\theta_{in} + \beta_i) \cot \beta_i + r - r \sin(\theta_h + \beta_i) \\
&= r - r \frac{\sin(\theta_{in} + \beta_i) \sin \beta_i + \cos(\theta_{in} + \beta_i) \cos \beta_i}{\sin \beta_i} \\
&= r \left(1 - \frac{\cos \theta_{in}}{\sin \beta_i} \right)
\end{aligned} \tag{D.37}$$

For the outer interface, using Equations D.3, D.5 replacing θ_r by $\pi - \theta_a$, we have:

$$\overline{OF} = r \sin(\pi - \theta_a + \beta_i) \tag{D.38}$$

$$\overline{FB} = r \cos(\pi - \theta_a + \beta_i) \cot \beta_i \tag{D.39}$$

and then:

$$\begin{aligned}
\overline{EB} &= \overline{OF} + \overline{FB} - \overline{OE} \\
&= r \sin(\pi - \theta_a + \beta_i) + r \cos(\pi - \theta_a + \beta_i) \cot \beta_i - r \\
&= -r + r \frac{\sin(\pi - \theta_a + \beta_i) \sin \beta_i + \cos(\pi - \theta_a + \beta_i) \cos \beta_i}{\sin \beta_i} \\
&= r \frac{\cos(\pi - \theta_a)}{\sin \beta_i} - r \\
&= -r \left(\frac{\cos \theta_a}{\sin \beta_i} + 1 \right)
\end{aligned} \tag{D.40}$$

Equalizing distances of both crests (Equations D.37 and D.40):

$$\theta_{in} = \arccos(2 \sin \beta_i + \cos \theta_a) \tag{D.41}$$

To calculate p_c , we use Equation 3.40 replacing $\theta_h = \theta_{in}$ by the expression from

Equation [D.41](#).

$$\begin{aligned}
b_i &= \frac{\sigma}{p_c} \frac{\cos(\theta_{in} + \beta_i)}{\sin \beta_i} \\
b_i &= \frac{\sigma}{p_c} \frac{\cos(\arccos(2 \sin \beta_i + \cos \theta_a) + \beta_i)}{\sin \beta_i} \\
p_c &= \frac{\sigma}{b_i} \left(\frac{\cos(\arccos(2 \sin \beta_i + \cos \theta_a) + \beta_i)}{\sin \beta_i} \right)
\end{aligned} \tag{D.42}$$

If Δp is equal or lower than the p_c value calculated using Equation [D.42](#), the layer collapses.

Appendix E

Calculation of conductance expressions

This section presents the geometrical equations employed to compute conductance at corners. Notice that the geometrical analysis is valid for layers. These expressions use expressions proved in Appendix D.

When calculating corner conductance, we consider a phase located on a corner with half corner angle β , separated from the other phase by an AM with contact angle θ and distance to the corner b , like in Figures 3.12b and 3.12c. Equation D.10 gives an expression for the cross-sectional area A_{co} using r_d , and Equation D.6 gives a relation between r_d and b :

$$r_d = b \frac{\sin \beta}{\cos(\theta + \beta)} \quad (\text{E.1})$$

We get the final expression for A_{co} (Eq. 3.69) by combining D.10 and E.1. This expression is independent of the AM curvature.

Then, the cross-sectional corner perimeter P_{co} is determined considering all interfaces. The solid-fluid interface has a length of $2b$. Equation D.2 provides the length of the fluid-fluid interface, which can also be represented in terms of b according to Equation E.1.

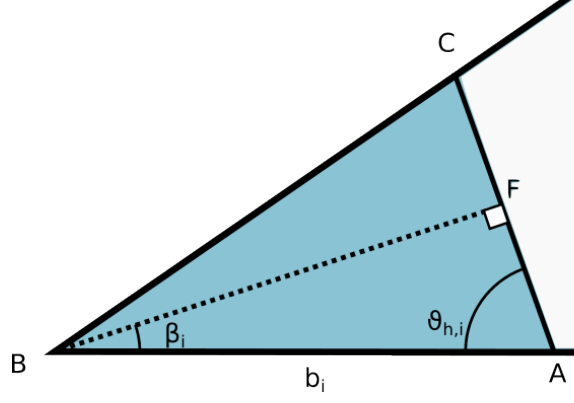


Figure E.1: Planar fluid-fluid interface, when $r \rightarrow \infty$

$$\widehat{AEC} = \frac{2b \sin \beta}{\cos(\theta + \beta)} \left(\frac{\pi}{2} - \theta - \beta \right) \quad (\text{E.2})$$

Equation 3.70 is obtained by adding up the lengths of all interfaces.

$G_{r \rightarrow \infty}$ is calculated using A_{co} and P_{co} for a planar fluid-fluid interface (see Figure E.1). In this case:

$$A_{r \rightarrow \infty} = \overline{FB} \cdot \overline{FA} = (b_i \cos \beta_i)(b_i \sin \beta_i) = b_i^2 \sin \beta_i \cos \beta_i \quad (\text{E.3})$$

$$P_{r \rightarrow \infty} = 2(\overline{AB} + \overline{FA}) = 2(b_i + b_i \sin \beta_i) = 2b_i(1 + \sin \beta_i) \quad (\text{E.4})$$

and then:

$$G_{r \rightarrow \infty} = \frac{A_{r \rightarrow \infty}}{P_{r \rightarrow \infty}^2} = \frac{b_i^2 \sin \beta_i \cos \beta_i}{(2b_i(1 + \sin \beta_i))^2} = \frac{\sin \beta_i \cos \beta_i}{4(1 + \sin \beta_i)^2} \quad (\text{E.5})$$